UNIVERSITY
OF TRENTO - Italy
Department of Materials Engineering
and Industrial Technologies

Doctoral School in Materials Engineering – XXII cycle

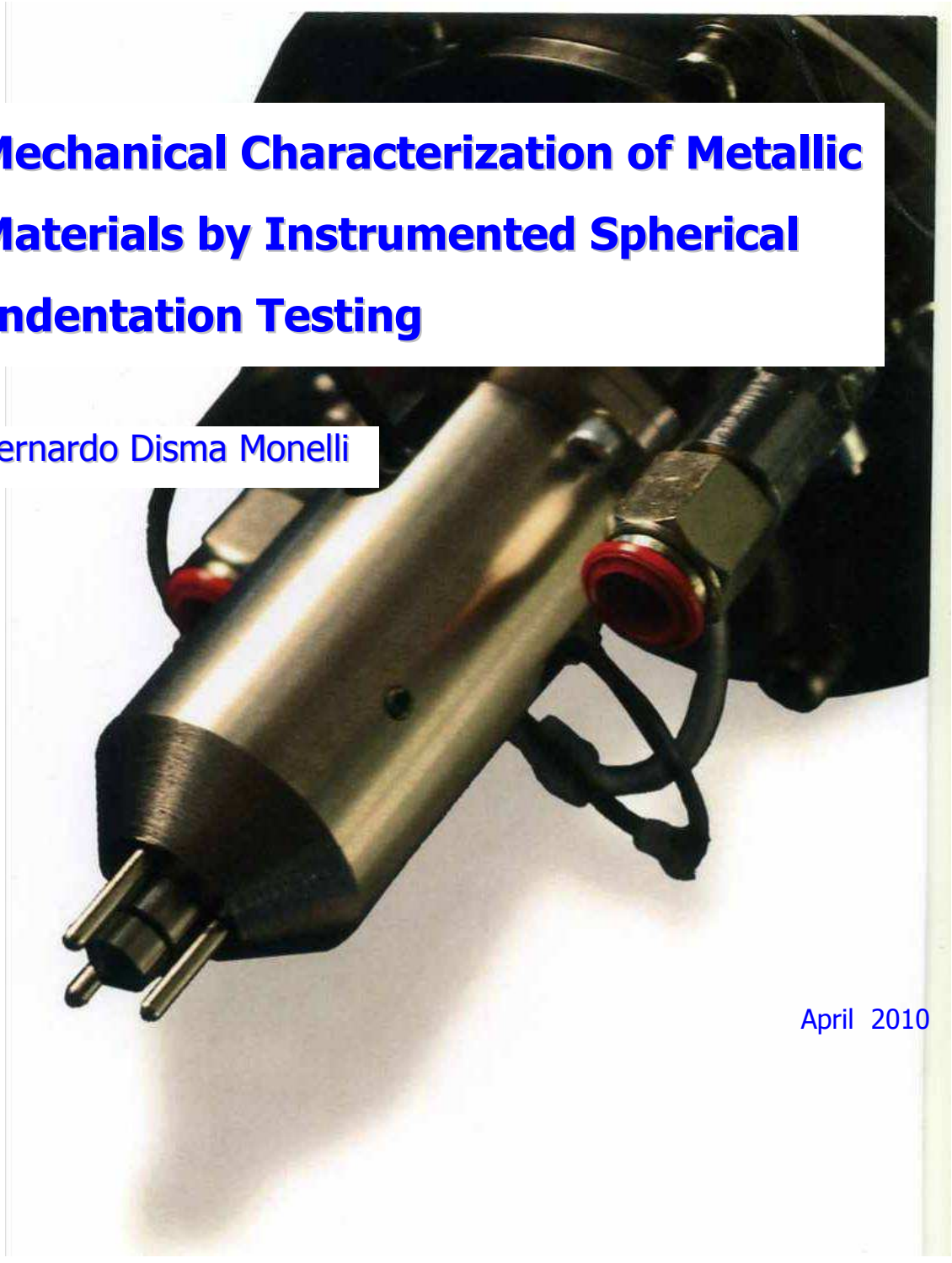

Mechanical Characterization of Metallic Materials by Instrumented Spherical Indentation Testing

Bernardo Disma Monelli

April 2010

Contents

1 Introduction and overview

PART ONE – STATE OF THE ART

2 Spherical Indentation Mechanics in Elastic-Plastic Solids

2.1 Spherical Indentation Response and Associated Nomenclature

2.1.1 Loading and un-loading indentation depth curves

2.1.2 Crater profile morphologies

2.2 Frictionless Spherical Indentation Stress and Strain Fields in Elastic- Plastic Solids

2.2.1 Indentation Regimes

2.2.2 Hill's Similarity Solution

2.2.3 Mesarovich and Fleck's model

2.3 Frictional effects onto the spherical indentation metallic materials response

2.4 Summary

3 Stress-Strain constitutive laws evaluation procedures

3.1 Tabor's approach

3.2 Modified Tabor's based approaches

3.3 Evaluation procedures based on the Reference Point Concept

3.3.1 Reference Point Concept

3.3.2 Taljat's evaluation procedure

3.3.3 Lee's evaluation procedure

3.4 Evaluation procedures based on the Representative Strain Concept

3.4.1 Representative Strain Concept

3.4.2 Cao's evaluation procedure

3.4.3 Zhao's evaluation procedure

3.5 Evaluation procedures based on the Load-Penetration Depth Curve Analysis

3.6 Summary

PART TWO – RESEARCH ACTIVITY

4 Materials and Methods

4.1 Indentation Testing Machine

4.1.1 Technical Specifications and Features

4.1.2 Testing machine Supporting System

4.1.3 Testing machine Indentation Unit

4.1.4 Testing machine zero setting

4.2 Computational modelling of the spherical indentation test

4.2.1 Model formulation

4.2.2 Basic Issues of computational modelling qualification

4.2.3 Mesh density and mesh typology convergence

4.2.4 Indenter compliance and element technology effects

4.3 Experimental constitutive behaviours of the reference materials

4.3.1 Basic issues of the integration
4.3.2 Experimental constitutive behaviours of the reference materials
4.3.3 Experimental indentation response of the reference materials
4.3.4 Residual crater profile analysis
4.3.5 Testing machine calibration
4.3.6 Computational model validation
4.4 Summary
5 Numerical analysis of the plastic deformation process
5.1 Plastic strains field evolution into the sub-indenter region
5.1.1 Plastic strains field evolution promoted by frictionless indenter
5.1.2 Frictional effects onto the plastic deformation process
5.2 Crater profile evolution
5.2.1 Crater profile evolution in frictionless spherical indentation
5.2.2 Frictional effects onto the crater profile evolution
5.3 Frictional effects onto load – penetration depth curves
5.4 Summary
6 Direct and reverse analysis. Setup and assessment of the algorithms
6.1 Direct analysis
6.1.1 *Material model and L-h curves database*
6.1.2 L-h curves interpolation
6.2 Reverse Analysis
6.3.1 *L-h* curve interpolation function
6.3.2 Error analysis
6.3 Experimental validation of the reverse analysis
6.4 Summary
7 Concluding remarks
References

CHAPTER 1
Introduction and overview

Instrumented indentation testing is now considered one of the most attractive tools for characterizing engineering materials. A large number of materials properties can be investigated, from the hardness to the materials fracture toughness. Such techniques are non-destructive and do not require specimen preparation. Instrumented indentation testing can be also applied even though small amounts of materials are available. In this frame, instrumented spherical indentation testing is especially considered the most powerful tool for inferring the constitutive laws of metallic materials. However, the large number of analytical and numerical approaches developed in the last two decades revealed that the interpretation of the experimental indentation response is not a straightforward task. Complex straining phenomena are induced by the indenters, thus making it impossible to deduce the constitutive properties of the indented materials easily and accurately. From this point of view the present dissertation was aimed at developing a new methodology for inferring the material behaviour of metallic materials from their indentation response. To achieve this goal, a deep investigation and analysis of the indentation response of metallic materials were

carried out. The research was performed into two steps. The deformation mechanisms promoted by spherical indenters in the sub-indenter region and the procedures developed for inferring the constitutive parameters via analysing the spherical indentation response were investigated in the first part of this dissertation. On the base of the acquired information, a new methodology was built-up in the second part of the present research.

The knowledge of the typical straining phenomena induced by spherical indenters are of paramount importance for understanding which information referring to the behaviour of the indented material are collected by the indentation response. In this frame, Chapter 2 was devoted to review the most prominent indentation theories. Strains field evolution in the sub-indenter region was especially analysed and correlated with the characteristic indentation response represented by the load-indentation depth curve (L-h curve) and crater profile geometry. The evaluation procedures developed to interpret such deformation mechanisms were then focused in Chapter 3. Advantages and drawbacks of each procedure were highlighted.

The analysis of the material indentation response revealed, from both the considered point of view, several criticalities which can potentially affect the accuracy of the predictions. Ideal constitutive behaviours are always assumed and adopted to establish the material response and to deduce constitutive laws, respectively. The lack of bridging between the experimental response of real materials and analytical or numerical predictions was observed. Experimental parameters as friction that play surely a crucial role in the deformation process were

not fully established. Accordingly, the investigation of real materials behaviour through these methodologies appeared particularly critical.
The information acquired in the first part of the present research were used for developing a new tool allowing to investigate the experimental data and the deformation processes induced by spherical indenters simultaneously. To this purpose, a testing machine and a computational model were specifically built-up for performing instrumented spherical indentation test and inferring the attendant deformation phenomena occurring in the indented target. Chapter 4 is devoted to present both the new testing machine and the computational model as well as the procedure adopted to integrate these new tools. The availability of a tool experimentally assessed offered the opportunity to explore the straining phenomena promoted by the indenters during the experimental test with an high level of accuracy, thus making it possible to establish the most reliable source of information from the point o view of the constitutive law estimation. In addition, the new tool allowed to assess the role played by key experimental parameter like the friction between the contacting bodies. To this purpose, the indentation response of two real materials were investigated and the results presented in Chapter 5. Friction were found to affect the crater morphology and the plastic strains distribution in the sub-indenter region, whilst negligible effects were observed onto the trend of the L-h curve. Accordingly, the characteristic L-h curve resulted to be the most reliable experimental data for inferring the constitutive parameters of metallic materials.
The direct analysis for correlating the constitutive material parameters to the load-indentation depth curve, from one side, and

the reverse analysis for deducing the material parameters from the aforementioned curve were described in Chapter 6.
Finally, interesting topics were presented for future developments.

CHAPTER 2
SPHERICAL INDENTATION MECHANICHS IN ELASTIC-PLASTIC SOLIDS

The indentation response of any materials is strictly related to the deformation phenomena involved in the region beneath the indenter. Therefore, the constitutive properties evaluation by instrumented indentations testing cannot leave out of consideration a deep understanding of the deformation mechanisms activated by the indenter during the indentation process. Distinguishing and characterizing the straining phenomena induced by the indenter leads to establish which are the material properties and experimental parameters driving the deformation mechanisms and, consequently, how the information concerning the constitutive behaviour of the indented material are collected by the material indentation response.

For metallic materials, the indentation response is driven by the elastic-plastic strains field evolution and contact conditions. In the literature there are many theories developed to describe the spherical indentation mechanics, theories based on experimental findings and analytical-numerical approaches.

The present chapter is devoted to review the main experimental evidences and computational models concerning the spherical

indentation mechanics of elastic-plastic materials. Special emphasis is dedicated to highlight the limits of each model as well as the agreements with the experimental results in order to establish their accuracy and predictive capabilities. After introducing the main physical quantities, which can be gauged during an instrumented indentation test and the associated nomenclature, the most important experimental findings are reported. Then, the deformation mechanisms promoted by spherical indenters into elastic-ideally plastic and work hardening media are analysed. Correlations with the crater profile evolution and sinking-in and piling-up phenomena are also investigated. Since the friction between the contacting bodies cannot be neglected in the experimental test, frictional effects onto the characteristic load-indentation depth curve and stress-strain fields evolution are also analysed.

2.1 Spherical Indentation Response and Associated Nomenclature

2.1.1 Loading and un-loading indentation depth curves

Indentation-based technique for materials characterization is perhaps one of the most promising and attractive tool nowadays available in materials engineering and science. Depending on the indenter type and the range of the applied loads to the indenter, different materials properties can be inferred [1-26]: hardness, toughness and constitutive laws evaluation of ceramic and metallic materials are

only some examples of the large number of applications based on the indentation testing.

As regards to the evaluation of the constitutive laws of metallic materials, instrumented spherical indentation testing is now considered a very attractive tool [27-29]. Fig. 2.1 shows a schematic representation of the spherical indentation test and the attendant load-indentation depth curve (*L*-*h* curve) which can be obtained by continuously measuring the driving force *L* and the indent depth *h* during the test.

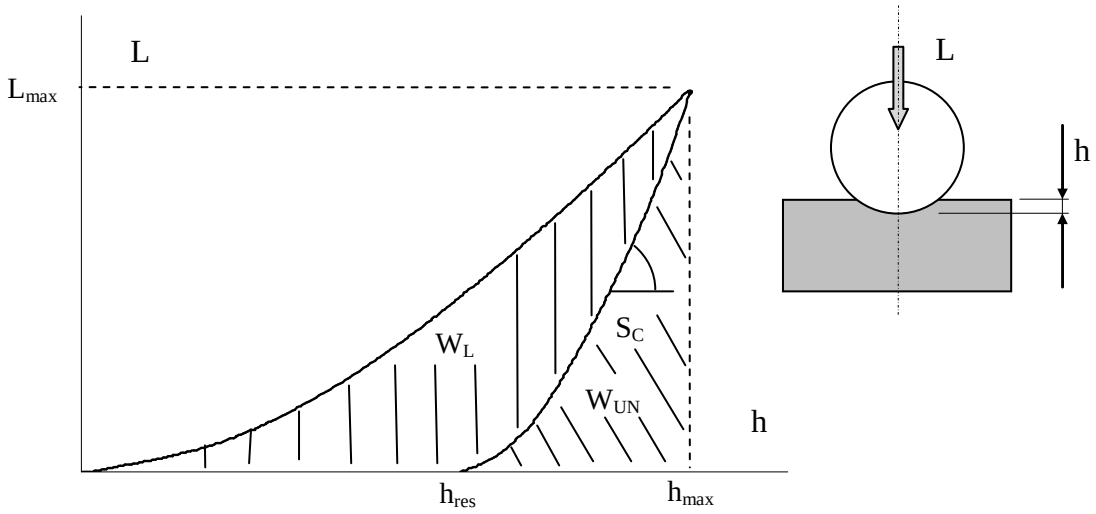

Figure 2.1. Spherical indentation test and the typical attendant load *L* – indentation depth *h* response of the indented material.

Chen et al. [29] showed that several shape factors characterizing the material indentation response can be recognized by analysing the trends of the loading and unloading curves of the indentation cycle. It is apparent that the maximum applied load L_{max}, the corresponding

penetration depth h_{max} and the residual indentation depth h_{res} must be considered as the most characteristic parameters of materials indentation response. However, these parameter are not sufficient to uniquely identify the material *L-h* curve. According to Chen et al. and Chen et al. [27,29], the knowledge of the loading and unloading cycles forms and the areas under these two curves, the total work done by the indenter W_L and the elastic work W_{UN} stored in the bulk, are needed to fully define the frame. In addition, Pharr et al. and Oliver et al. [24,26,30] probed that the initial slope of the unloading curve can be related to the materials elastic properties. Therefore, the slope of the unloading ramp, S_C, evaluated at the maximum reached load can be considered as a further characteristic parameter of the material indentation response.

Experimental findings and analytical predictions [1,31-34] confirm that the form of the loading curve is dictated by the indenter geometry. If sharp indenters are used in the indentation test, the loading cycle is well described by Kick's Law,

$$L = Ch^2 \tag{2.1}$$

where the loading curvature *C* is a material constant. The quadratic form is an obvious consequence of the geometric indenter self-similarity [31-33].

Conversely, when spherical indenters are driven into the material Meyer's Law [34-35],

$$\frac{L}{\pi a^2} = k\left(\frac{a}{D}\right)^{1/m} \tag{2.2}$$

where *k* and *m* (>1) are a set of constant depending on the material behaviour, is well-obeyed. Here, *D* is the diameter of the sphere, whilst *a* the radius determined by the intersection between the indenter contact profile with the original undeformed surface. As expected, being the self-similarity lost in a spherical indentation test, the corresponding loading curvature *C* is a function of the penetration depth *h* and varies during both loading and unloading cycles. However, as shown by O'Neill [36], Meyer's Law is not just an empiricist relationship between the applied load *L* and the crater geometry: uniaxial true stress-strain curve of metallic materials, in fact, can be well-fitted by the following power law characterized by the same *m* exponent,

$$\tau = \kappa \gamma^{1/m} \tag{2.3}$$

where τ and γ are Cauchy stress and logarithmic plastic strain, respectively, and κ is a material constant. The extensive analysis by Tabor [1], finally, revealed that *k*, κ and *m* are correlated:

$$\frac{k}{\kappa} = \alpha \beta^{1/m} \tag{2.4}$$

and α and β are two universal constants whose values are close to 3.0 and 0.4, respectively. By substituting (2.4) into (2.2), it results,

$$\frac{L}{\pi a^2} = \alpha \kappa \left(\frac{\beta a}{D}\right)^{1/m} \tag{2.5}$$

thus proofing that the apparent hardness $L/\pi a^2$ is α times the material flow stress corresponding to the representative strain $\beta a D$.

2.1.1 Crater profile morphologies

Although the material *L-h* curve represents the primary source of information about the indented material behaviour, the crater profile evolution during the indentation test as well as the residual impression morphology can be used to characterize the material indentation response [37-39]. Typical impression morphologies which can be promoted by indenting a metallic material with a spherical indenter are sketched in Fig. 2.2.

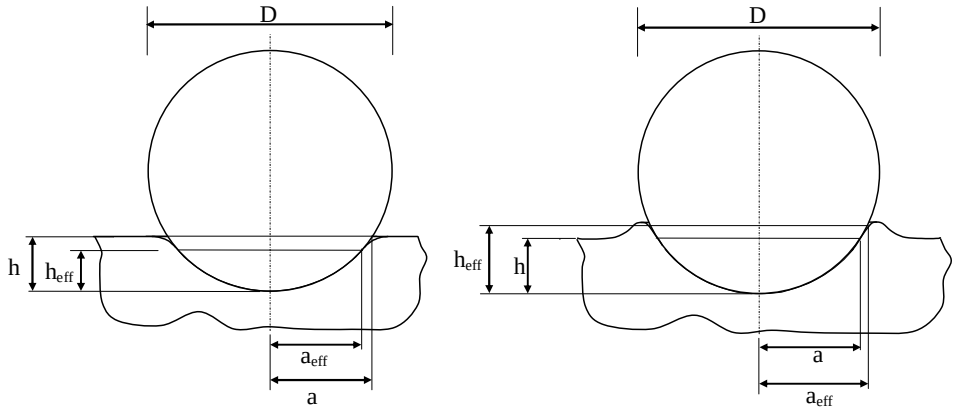

Fig. 2.2. Schematic representation of the spherical indentation crater geometry. Sinking-in (left) and piling-up phenomena (right).

As illustrated by Figure 2.2, a quite complex profile characterizes the impressions produced by spherical indenters onto metallic materials. The representation of the crater profile as an ideal spherical cap having the penetration depth *h* and the contact radius *a* as height and base radius respectively, leads to a information loss about the indented material behaviour: material sinking-in and piling –up phenomena were observed experimentally [40,41], thus confirming

that the actual crater morphology is far from this ideal representation. Material piling-up and sinking-in amounts are related to the indented material constitutive properties [38,39]. Accounting for the real response of the indented surface, the effective indent depth h_{eff}, which represents the actual height of the indenter portion immersed into the indented material, will differ from the penetration depth h. Larger and smaller values of h_{eff} with respect to h must be expected if the material indentation response is governed by piling-up or sinking-in phenomena, respectively. Equally, the actual contact radius a_{eff} will differ from the surface contact radius "*a*" and greater or lower values than "*a*" must result when piling-up and sinking-in phenomena are considered. Accordingly, owing to piling-up and sinking-in phenomena, the effective contact area will be different from the ideal contact area which is obtained if these phenomena are neglected.

The extensive body of data elaborated by Norboury et al. [40] also reveals that the penetration depth h can be related to a^2 during the indentation process and the ratio,

$$c^2 = a^2/Dh \tag{2.6}$$

is an invariant which depends on the same m exponent encountered in Meyer and O'Neill's et al. [34,36] predictions, over a wide range of materials. As will be shown in the next paragraphs, the function $c^2(m)$ is monotonic increasing and can be used to evaluate material piling-up and sinking-in amounts, thus making it potentially possible to infer the material m exponent of Eqn. (2.3) by a proper analysis of the impression geometry left by the indenter.

2.2 Frictionless Spherical Indentation Stress and Strain Fields in Elastic-Plastic Solids

2.2.1 Indentation Regimes

L-h curve and crater profile evolution during the indentation are a macroscopic effect of the deformation processes occurring in the region beneath the indenter. To establish a proper correlation between the material indentation response and each stage of the indentation process, it is of paramount importance to distinguish the strain processes promoted by spherical indenters as function of material properties and indent depth *h*.

To fully understand the straining processes induced by a spherical indenter into metallic materials, frictionless spherical indentation of homogeneous, isotropic and linear elastic-ideally plastic media is firstly analyzed. An infinite half-space is considered. A sketch of the problem configuration is depicted in Fig. 2.3. An ideal contact impression, characterized by a contact radius *a*, is assumed to be produced by the indenter.

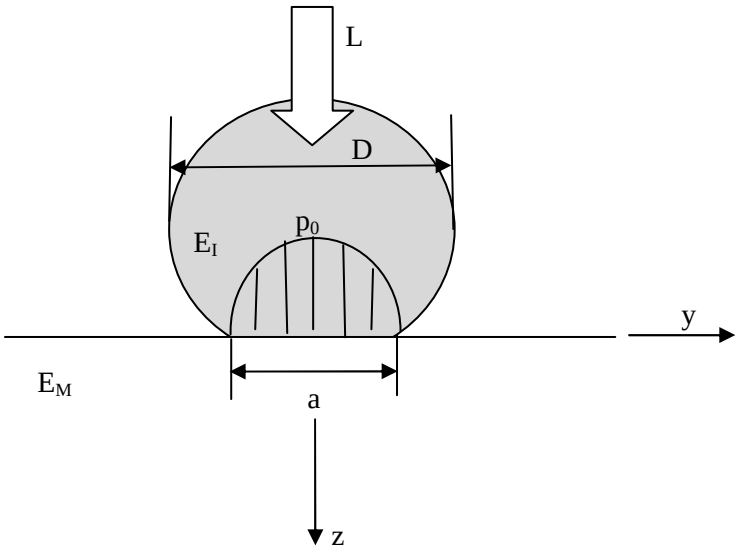

Figure 2.3. Sketch of the spherical indentation regimen into metallic materials.

Until the yielding stress of the indented material is not exceeded, the strain process is solely driven by the elastic stresses distribution and the elastic contact regime proposed by Hertz [42,43] governs the material indentation response. Accordingly, the load-indent depth curve pertinent to this regime is represented by the well-known power-law found by Hertz [44],

$$L = \frac{4}{3}\sqrt{\frac{D}{2}}E^{*}h^{3/2} \qquad (2.7)$$

in which the elastic modulus of the indented solid has been replaced by the effective elastic modulus E* defined as ,

$$\frac{1}{E^{*}} = \frac{1-\nu_I^2}{E_I} + \frac{1-\nu_M^2}{E_M} \qquad (2.8)$$

in order to take into account the indenter compliance. Here, E_I, ν_{I} and E_M, ν_{M} represent the Young's modulus and Poisson ratio of the indenter and indented half-space, respectively. Stress field in the half-space can be derived following the procedure proposed by Timoshenko and Goodier [45], once the loading conditions are known. According to Hertz's theory, the pressure distribution *p(r)* between the sphere and the infinite half-space takes the following form:

$$p(r) = p_0(a^2 - r^2)^{1/2}/a \tag{2.9}$$

where p_0 is the maximum pressure between the contacting bodies. The equilibrium of the indenter along the indentation axis provides the relationship between the applied load L and p_0,

$$L = \frac{2}{3}\pi p_0 a^2 \tag{2.10}$$

Consequently, the elastic stress components on the indented surface $(z = 0)$ and inside the loaded circle $(0 \le r \le a)$ result [45],

$$\sigma_r = \left\{\frac{(1-2\nu_M)}{3}\frac{a^2}{r^2}\left[1 - \left(1 - \frac{a^2}{r^2}\right)^{3/2}\right] - \left(1 - \frac{a^2}{r^2}\right)^{1/2}\right\} p_0 \tag{2.11a}$$

$$\sigma_\theta = -\left\{\frac{(1-2\nu_M)}{3}\frac{a^2}{r^2}\left[1 - \left(1 - \frac{a^2}{r^2}\right)^{3/2}\right] - 2\nu_M\left(1 - \frac{a^2}{r^2}\right)^{1/2}\right\} p_0 \tag{2.11b}$$

$$\sigma_z = -\left(1 - \frac{a^2}{r^2}\right)^{1/2} p_0 \tag{2.11c}$$

whereas outside the loaded circle $(r \ge a)$,

$$\sigma_r = -\sigma_\theta = (1 - 2\nu_M)\frac{a^2}{3r^2}p_0 \quad (2.12)$$

Conversely, along the indentation axis (z-axis):

$$\sigma_r = \sigma_\theta = \left\{-(1+\nu_M)\left[1 - \frac{z}{a}\tan(a/z)^{-1}\right] + \frac{1}{2}\left(1 + \frac{z^2}{a^2}\right)^{-1}\right\}p_0 \quad (2.13a)$$

$$\sigma_z = -\left(1 + \frac{z^2}{a^2}\right)^{-1} p_0 \quad (2.13b)$$

It should be noted that along the indentation axis (*z*-axis) the stress components σ_r , σ_θ and σ_z given by Eqns. (2.13) are principal stresses and the principal shear stress (Fig. 2.4)

$$\tau_1 = \frac{1}{2}|\sigma_z - \sigma_\theta| \quad (2.14)$$

takes the maximum value along the indentation axis at a depth $z = 0.48a$ for $\nu_M = 0.3$, as usually occurs for metallic materials. Therefore, plastic strains development must be expected to initiate in that region beneath the indenter tip centred at the aforementioned depth.

Metallic materials yield is usually well described by either the Von Mises's Criterion,

$$\frac{1}{6}\{(\sigma_1 - \sigma_2)^2 + (\sigma_2 - \sigma_3)^2 + (\sigma_3 - \sigma_1)^2\} = \frac{S_{yp}^2}{3} \quad (2.15)$$

or Tresca's Criterion,

$$max\{|\sigma_1 - \sigma_2|, |\sigma_2 - \sigma_3|, |\sigma_3 - \sigma_1|\} = S_{yp} \quad (2.16)$$

in which σ_1, σ_2 and σ_3 are the principal stresses and S_{yp} the material yield stress in monotinic uniaxial tension (or compression). By rearranging the Eqns. (2.10), (2.13) and (2.15) or (2.16), it is possible to deduce the plastic onset in terms of the applied load *L* to the indenter. If $L_{S_{yp}}$ denotes the load value at which the plastic deformation process starts to occur, the following relationship among $L_{S_{yp}}$,indenter geometry and the material yield stress can be obtained:

$$L_{S_{yp}} = \frac{\pi^3 D^2}{24 E^{*2}} S_{yp}^3 \qquad (2.17)$$

In terms of indentation average pressure p_m, $(p_m = L/\pi a^2)$, the plastic yield onset is achieved when,

$$p_m \approx 1.1 S_{yp} \qquad (2.18)$$

Accordingly, once the threshold given by Eqn. (2.17) or Eqn. (2.18) is exceeded, the yielding process starts to occur. As predicted by Eqns. (2.13) and (2.14) plastic strains firstly develop along the indentation axis at a depth from the contact surface depending on the indented material Poisson ratio. The initial plastic core radially spreads and, as the indentation becomes more severe, it may break out to the free surface, thus entirely surrounding the indenter contact surface [44]. Therefore, the deformation mechanism into the sub-indenter region at this stages of the indentation process is characterized by a strong interaction between the plastic strain field, pertinent to the region immediately beneath the indenter, and the elastic strain distribution surrounding the plastic core. Since both the components of the strain, elastic and plastic, are comparable, the material indentation

response will be affected by both elastic and plastic material properties. As the indentation depth *h* further increases, it must be expected that the containing effect of the surrounding elastic medium gradually tends to disappear and the plastic strains become dominant. Owing to the loosening of this containing action, the plastic flow can freely spread laterally and break out to the free surface at severe penetration depths, thus entirely surrounding the indenter and producing material piling-up phenomena. It is apparent that the material indentation response at these values of the penetration depths is mainly governed by the plastic properties of the indented material. Slip Line Theory [40,44] can be invoked for determining the transition between the elastic-plastic and fully plastic indentation regimes. According to SLT predictions, the transition to fully plastic indentation regime occurs as the indentation pressure p_m reaches a value given by the following expression for rigid-plastic solids:

$$p_m = kS_{yp} \tag{2.19}$$

where *k* is a constant depending on the contact conditions (friction coefficient) and the indenter geometry. Its values, however, is approximately equal to 3.0.

From the aforementioned analysis a very important remark can be drawn. Each indentation regime can be related to a specific portion of the indented material constitutive law. Since the elastic-plastic portion of materials stress-strain curves represent the most important source of information from the engineering point view, it should not be surprising if there are many analytical and numerical models aimed at describing the elastic-plastic indentation regimes of

engineering materials. However, the expanding spherical cavity model elaborated by Johnson [44,46] may be considered the most effective model for understanding how the strain process proceeds during the elastic-plastic indentation regime and determine the material properties driving the containing action by the surrounding elastic medium. Although the model validity is restricted to linear elastic-ideally plastic solids characterized by a constant yield stress in simple compression, Tabor's findings [1] have proofed that the expanding cavity model predictions can be extended also to elastic-work hardening solids, thus confirming the general validity of Johnson's model.

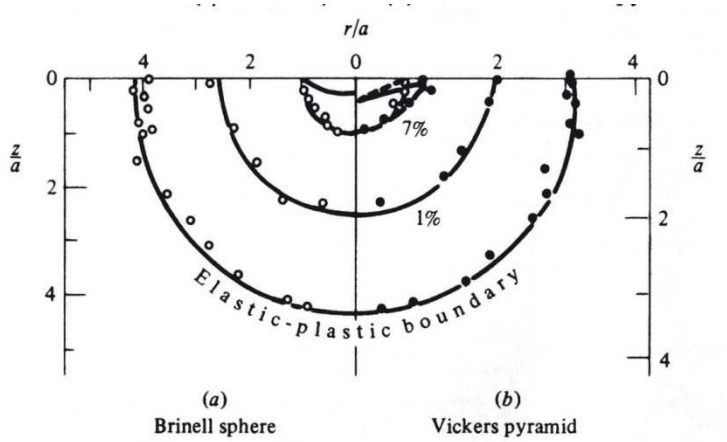

Figure 2.4. Johnson cavity model [44]: iso-strain distribution.

Accounting for the observations of Samuel et al. and Mulhearn [47,48], Johnson realized that the displacement field produced by any indenter (sharp or blunt) is approximately radial from the first contact point and it is also characterized by hemispherical iso-strain contours (Fig. 2.4). Based on these evidences, Johnson assumed

the sub-indenter region as composed by an hemispherical core immediately beneath the indenter having a radius *a* encased in an annular plastic region. An hydrostatic component of stress $\bar{p}$ is assumed to exist in the core, whilst the displacement and stress fields proper of an elastic-ideally plastic spherical cavity under the pressure $\bar{p}$ drive the material response outside the core. Let is *c* $(c \geq a)$ the elastic-plastic boundary radius. Within the plastic zone $(a \leq r \leq c)$ the stress components are given by Hill [49],

$$\frac{\sigma_r}{S_{yp}} = -2Ln\left(\frac{c}{r}\right) - \frac{2}{3} \tag{2.20a}$$

$$\frac{\sigma_\theta}{S_{yp}} = -2Ln\left(\frac{c}{r}\right) + \frac{1}{3} \tag{2.20b}$$

whereas in the elastic region it results,

$$\frac{\sigma_r}{S_{yp}} = -\frac{2}{3}\left(\frac{c}{r}\right)^3 \tag{2.21a}$$

$$\frac{\sigma_\theta}{S_{yp}} = \frac{1}{3}\left(\frac{c}{r}\right)^3 \tag{2.21b}$$

At the boundary of the core $(r = a)$, (2.20a) leads to

$$\frac{\bar{p}}{S_{yp}} = 2Ln\left(\frac{c}{a}\right) + \frac{2}{3} \tag{2.22}$$

The in-core pressure $\bar{p}$ may be easily evaluated by analysing the radial displacement field $u(r)$ under the hypothesis of incompressible media. As shown by Hill [49], if the indenter compliance can be

neglected, the radial displacement $u(r)$ is given by the following expression:

$$\frac{\mathrm{d}u}{\mathrm{d}r} = \frac{S_{yp}}{E_M}\left\{3(1-\nu_M)\left(\frac{c}{r}\right)^2 - 2(1-2\nu_M)\left(\frac{r}{c}\right)\right\} \qquad (2.23)$$

Compliant indenters may be considered in this analysis by simply replacing the half-space Young's modulus E_M with the elastic modulus E^* given by Eqn. (2.8). The conservation of core volume leads to

$$2\pi a^2 \mathrm{d}u(a) = \pi a^2 \mathrm{d}h = \pi a^2 \,\mathrm{Tan}\,\beta\,\mathrm{d}a \qquad (2.24)$$

for conical indenters, where β is the complementary angle of the cone apex semi-angle (Fig. 2.5).

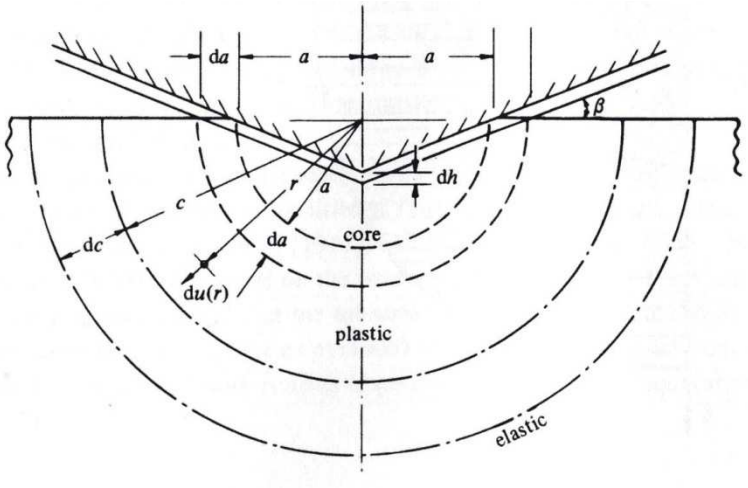

Figure 2.5. Cavity Model for an elastic-plastic indentation by a cone [44].

It is possible to apply the present model also to spherical indenters, by simply observing that $\mathrm{Tan}\,\beta \approx \mathrm{Sin}\,\beta = 2\mathrm{a}/\mathrm{D}$. To locate the elastic-

plastic boundary *c*, it is sufficient to substitute $r = a$ in Eqn. (2.23), accounting for, that due to the geometrical similarity of cone indenters, during the indentation process $\mathrm{d}c/\mathrm{d}a = c/a$. It is obtained:

$$\frac{E_M \operatorname{Tan}\beta}{S_{yp}} = 6(1-\nu_M)\left(\frac{c}{a}\right)^3 - 4(1-2\nu_M) \qquad (2.25)$$

Solving Eqn. (2.25) for and putting the results into Eqn. (2.22), the following expression for the pressure $\bar{p}$is obtained:

$$\frac{\bar{p}}{S_{yp}} = \frac{2}{3}\left\{1 + Ln\left(\frac{E_M \operatorname{Tan}\beta}{3S_{yp}}\right)\right\} \qquad (2.26)$$

Eqn (2.26) shows that the pressure $\bar{p}$ depends on the non-dimensional variable $\left(E_M \operatorname{Tan}\beta/S_{yp}\right)$ which may be seen as the ratio between the strain imposed by the indenter $(\operatorname{Tan}\beta)$ and the elastic strain capacity $\left(S_{yp}/E_M\right)$ offered by the indented material. In other terms, the ratio between the material yield stress and the elastic modulus represents the governing factor of the plastic core evolution in the sub-indenter region during the elastic-plastic regime.

2.2.1 Hill's Similarity Solution

Although the aforementioned theories allow to distinguish the straining processes induced by spherical indenters as a function of the indent depth *h*, the effective role played by the elastic-plastic material properties in the indentation response still represents an open issue: the basic assumption concerning the constitutive law, in fact, does not allow to establish a direct link with the major

experimental findings [1,34,36,40]. Therefore, a theory able to explain the observed phenomena is needed.

It should be noted that early experimental results refer to deep indentations, being aimed at evaluating the materials plastic properties. Under these conditions, a direct link between the fully plastic indentation regime and material plastic properties must be addressed.

Unfortunately, SLT [40,44] is only able to establish the transition from the elastic-plastic regime to fully plastic regime. However, as shown by Hill et al. [50], an analytical model able to furnish such correlations can be developed if the following main hypotheses are assumed.

- At any stage during the indentation, the indenter causes infinitesimal deformations in the sub-indenter region and the strain path in the sub-indenter infinitesimal volumes is monotonic radial.
- Nonlinear elastic behaviour drives the indented material response.

Due to the implications of Hill's model in the development of the subsequent indentation theories, it is of paramount imporance to review in detail the most important parts of such model. It is evident that the aforementioned hypotheses are very significant from the theoretical point of view. Therefore, the constitutive framework and the effects of these assumptions are firstly delineated.

To begin with, let us denote with σ_{ij} the components of Cauchy stress and with ε_{ij}infinitesimal strain tensor, whilst with $\phi(\sigma_{ij})$ and $\psi(\varepsilon_{ij})$ the Legendre potentials which are assumed to be symmetric,

strictly convex and homogeneous with degres of $(n+1)$ and $(m+1)$, respectively. Then,

$$\varepsilon_{ij} = \partial\phi/\partial\sigma_{ij}, \qquad \sigma_{ij} = \partial\psi/\partial\varepsilon_{ij}, \qquad \varepsilon_{ij}\sigma_{ij} = \phi + \psi \tag{2.27}$$

can be treated as the general representation of the elastic response of the indented medium. The Eulero's identity provides the fundamental connexion,

$$(n+1)\phi = (m+1)\psi = \varepsilon_{ij}\sigma_{ij} \tag{2.28}$$

between the potentials. A suitable rearrangement of the Eqn. (2.28) leads to,

$$\phi = m\psi, \qquad \psi = n\phi, \qquad mn = 1 \tag{2.29}$$

Due to the potentials self-similarity, their separate equations can be expressed by positive functions of degree one, as follows:

$$\tau(\sigma_{ij}) = cost., \qquad \gamma(\varepsilon_{ij}) = cost., \tag{2.30}$$

whence τ has the dimension of the stress whilst γ is a dimensionless parameter. Within this framework, if the potentials are assumed to expressed by the following expressions,

$$\phi(\sigma_{ij}) = \kappa\frac{[\tau(\sigma_{ij})/\kappa]^{n+1}}{(n+1)}, \qquad \psi(\sigma_{ij}) = \kappa\frac{[\gamma(\varepsilon_{ij})]^{m+1}}{(m+1)} \tag{2.31}$$

and the Eqn. (2.28) is accounted for, the parameters τ and γ are correlated by the following relationship:

$$\tau = \kappa \gamma^m \tag{2.32}$$

The Eqn. (2.32) proofs how it is possible to derive a constitutive low formally equivalent to that proposed by O'Neill [36] if infinitesimal deformation is assumed to be produced by the indenter in a medium obeying to a nonlinear elastic constitutive law. However, any speculations from now on within this frame and concerning the indentation response of metals cannot be accepted if the equivalence between the metals elasto-plasticity and the constitutive model expressed by the Eqn. (2.32) has been proofed before. In terms of the parameters τ and γ the Eqn. (2.27) can be replaced by,

$$\varepsilon_{ij} = \gamma \partial\tau / \partial\sigma_{ij}, \qquad \sigma_{ij} = \tau \partial\gamma / \partial\varepsilon_{ij}, \qquad \varepsilon_{ij}\sigma_{ij} = \gamma\tau \tag{2.33}$$

Under the assumption of monotonic radial strain path, the gradients of and remain constant, thus turning out:

$$\delta\varepsilon_{ij} = \partial\tau / \partial\sigma_{ij}\delta\gamma, \quad \delta\sigma_{ij} = \partial\gamma / \partial\varepsilon_{ij}\,\delta\tau \quad (\delta\gamma > 0) \tag{2.34}$$

with regards to the incremental response of the indented material. It is apparent that, except for the volume elastic changes, elastic-plastic behaviour of metals is similarly modelled by the relationships (2.34), thus proofing that the nonlinear elastic behaviour can be regarded to model the indentation response of metallic materials in the Meyer's regime, once the strain path is assumed to be essentially monotonic radial in the sub-indenter region.

On the basis of the aforementioned framework, stress and strain fields are driven by the following field equations within the half-space,

$$\varepsilon_{ij} = \gamma \partial\tau/\partial\sigma_{ij} \qquad \sigma_{ij} = \tau \partial\gamma/\partial\varepsilon_{ij} \qquad \varepsilon_{ij}\sigma_{ij} = \gamma = (\tau/\kappa)^n \quad (2.35a)$$

$$\varepsilon_{ij} = \tfrac{1}{2}\left(\partial u_i/\partial x_j + \partial u_j/\partial x_i\right) \qquad \partial\sigma_{ij}/\partial x_i = 0 \quad (2.35b)$$

which must satisfy the following boundary conditions,

$$\sigma_{13} = \sigma_{23} = \sigma_{33} = 0 \qquad (r > a) \quad (2.36a)$$

$$\sigma_{13} = \sigma_{23} = 0 \qquad (r \leq a) \quad (2.36b)$$

where $r^2 = x_1^2 + x_2^2 + x_3^2$, whilst the stress field σ_{ij} must vanish at infinity like $1/r^2$. Here, u_i denote the infinitesimal components of the displacement evaluated at the point x_i. Since the impression profile must be smooth at the contact radius *a*, an additional conditions relates the contact radius to indent depth *h* and indenter diameter *D*. Hence, one of these three parameters or equivalently the ratio a^2/hD can be considered an effective eigenvalue, whereas the others two can be regarded as given. The assumed potentials homogeneity, however, ensures the problem self-similarity, i.e. all the solutions of the field problem (2.36), can be generated from just one by an appropriate scaling. In the present case, if the original field variables are uniformly scaled as follow,

$$a\tilde{x}_i = x_i \qquad a\tilde{r} = r \qquad a\tilde{u}_i = (D/a)u_i(x_k, a, D)$$

$$\tilde{\varepsilon}_{ij} = (D/a)\varepsilon_{ij}(x_k, a, D) \qquad \tilde{\gamma}\left(\tilde{\varepsilon}_{ij}\right) = (D/a)\gamma\left(\varepsilon_{ij}\right) \quad (2.37)$$

$$\kappa\tilde{\sigma}_{ij} = (D/a)^{1/n}\sigma_{ij}(x_k, a, D) \qquad \kappa\tilde{\tau}\left(\tilde{\varepsilon}_{ij}\right) = (D/a)^{1/n}\tau\left(\sigma_{ij}\right)$$

the driving parameters *a*, *h* and *D* enter into the problem as the ratio $c^2 = a^2/Dh$, which is the new expression of the invariant eigenvalue, thus confirming the early observations of Norboury and Samuel [40]. In addition, due to the c^2 invariance, the mean pressure $L/\pi a^2$ over the contact surface can be evaluated as,

$$\frac{L}{\pi a^2} = -\kappa \left(\frac{a}{D}\right)^{1/n} \int_0^1 \tilde{\sigma}_{33}(\tilde{r})\, d(\tilde{r}^2) \tag{2.38}$$

thus proofing that it varies as $\left(\frac{a}{D}\right)^{1/n}$ during the indentation process. Accounting for the constitutive framework behind these results, Meyer and O'Neill experimental findings [34,36] can be regarded as successfully modelled by Hill's theory.

Tabor's formula may be also included in the present theory. Let us suppose that the integral in the Eqn. (2.38) approximately results equal to $\alpha\beta^{1/n}$, where α and β are two constants only depending on the energy density distribution. Then, from Eqn. (2.38), we would have,

$$\frac{L}{\pi a^2} \approx \alpha\kappa \left(\frac{\beta a}{D}\right)^{1/n} \tag{2.39}$$

which is exactly what was found by Tabor [1], after analysing the indentation metal response.

Finally, the Hill's model is also able to relate the exponent *n* to the material piling-up and sinking-in amount, which can be described by the function c^2. To proof this statement, we begin with show how such parameter can be used to describe piling-up and sinking-in phenomena. It is sufficient to consider that, if we denote with the

function *w*(*r*) the depth below the original surface at a distance *r* from the indentation axis, then from simple geometry considerations it results:

$$u_3(r) = h - r^2/D \quad (r \le a) \tag{2.40}$$

or in terms of scaled variables,

$$\tilde{u}_3(\tilde{r}) = 1/c^2 - r^2 \quad (r \le a) \tag{2.41}$$

Thus, the contact perimeter is at a level given by Eqn. (2.41), or equivalently by Eqn. (2.41), and it is below the original surface if $c^2 < 1$, whilst it is above if $c^2 > 1$. It is now evident how the parameter c^2 governs the sinking-in and piling-up phenomena induced by the spherical indenter. Let is *W* the total work spent to reach a generic indent depth *h* and *L* the corresponding applied load. For frictionless indentation, the total work must be equal to the total strain energy stored by the indented half-space, which is equivalent to the volume integral of $\psi(\varepsilon_{ij})$. In other terms, accounting for the relationship (2.28), *W* can be evaluated as,

$$W = \frac{n}{n+1}\int \varepsilon_{ij}\sigma_{ij}dx = \frac{2\pi n}{n+1}\int_0^a p(r)\,u_3(r)d(r) \tag{2.42}$$

where $p(r)$ is the contact pressure. The substitution of (2.40) into (2.42) leads to

$$\frac{n+1}{n}W = Lh - \frac{2\pi}{D}\int_0^a p(r)\,r^3 d(r), \quad L = 2\pi\int_0^a p(r)\,r d(r) \tag{2.43}$$

By considering the configuration which must be produced by a spherical indenter, it can easily proofed that,

$$Lh = (4n + 1)\, W/2n \tag{2.44}$$

Finally, by rearranging the relationships (2.43) and (2.44), it can be concluded that

$$\frac{W}{2n} = \frac{Lh}{4n+1} = \frac{2\pi}{2n-1}\int_0^a p(r)\, r^3 d(r) \tag{2.45}$$

which is equivalent to say,

$$c^2 = \frac{2n-1}{4n+1}\int_0^1 \tilde{p}(\tilde{r})\, \tilde{r} d(\tilde{r}) \Big/ \int_0^1 \tilde{p}(\tilde{r})\, \tilde{r}^3 d(\tilde{r}) \tag{2.46}$$

if the original variables are replaced by the new scaled variables. Here,

$$\tilde{p}(\tilde{r}) = (D/a)^{1/n} p(r)/\kappa \tag{2.47}$$

is the scaled pressure. Eqn. (2.46) allows to appreciate how the material piling-up or sinking-in amounts are related to the strain-hardening coefficient *n*. Based on an appropriate finite element investigation of nonlinear elastic solids (see Eqn. 2.32), Hill et al. [50] derived the following relationships,

$$c^2 = \frac{5}{2}\left(\frac{2-n}{4+n}\right) \tag{2.48}$$

Matthwes [37] proposed an alternative expression,

$$c^2 = \frac{1}{2}\left(\frac{2+n}{2}\right)^{\frac{2(1-n)}{n}} \tag{2.49}$$

to fit the data found by Norbury et al. [40].

2.2.1 Mesarovich and Fleck's model

Although the Hill's theory is able to model all the most significant experimental findings as well as the role played by the strain-hardening coefficient *n* in the crater profile evolution during the indentation process, the validity limits of such theory are not established yet. In addition, it should be noted that Hill's model does not take into account the role of friction onto the material indentation response. Accordingly, a well-established theory able to describe the actual indentation response of metals is not available yet.

It is apparent that, owing to the complexity of the deformation mechanisms promoted by the indenters, the analytical determination of the stress and strain fields evolution as a function of the contact conditions, indent depth and of course of material properties is a challenging essay. It should not be surprising, then, if the major efforts in the comprehension of the indentation phenomena have been spent to built-up numerical models able to simulate the indentation process and interpret their results.

In literature there are many numerical models aimed at determining the spherical indentation response of metallic materials [28,29,38,51-60], but surely the extensive numerical investigation performed by Mesarovic and Fleck [54] can be considered as the most exhaustive with regard to the characterization of indentation response of metals. The finite element model developed by the authors simulates the

indentation response of infinite half-spaces against which rigid frictionless indenters are driven. As regards to the material constitutive behaviour, homogeneity, isotropy and two constitutive laws, the Hollomon power law,

$$\frac{\varepsilon}{\varepsilon_0} = \frac{\sigma}{\sigma_0}, \qquad \sigma \leq \sigma_0 \tag{2.50a}$$

$$\frac{\varepsilon}{\varepsilon_0} = \left(\frac{\sigma}{\sigma_0}\right)^n, \quad \sigma > \sigma_0 \tag{2.50b}$$

and Ramberg-Osgood hardening law,

$$\frac{\varepsilon}{\varepsilon_0} = \frac{\sigma}{\sigma_0} + \left(\frac{\sigma}{\sigma_0}\right)^n \tag{2.51}$$

obeying to isotropic J_2 flow theory, are considered. Here, σ_0 and $\varepsilon_0 = \sigma_0/E$ are the representative strength and corresponding strain of the material respectively, *n* is the strain-hardening coefficient and E_M the corresponding Young's modulus. In the linear elastic-ideally plastic limit, $n \to \infty$, the relationships (2.50) and (2.51) are equivalent. To establish the validity limits of the theories previously described and evaluate how they depends on the constitutive properties the main numerical results obtained by Mesarovic and Fleck [54] concerning the frictionless indentation of linear elastic-ideally plastic media can be accounted for (Figure 2.6). The notation of the authors in which *R* is the sphere radius, *a* the effective contact radius and *h* and *L* respectively the indentation depth and the corresponding applied load to the indenter, is adopted. The results are plotted as a function of the Poisson coefficient ν, of the ratio E^*/σ_0 (being $E^* = E/(1-\upsilon)$) and the parameter $aE^*/(R\sigma_0)$. Johnson experimental

and numerical investigations [44,46] suggest that the elastic constant E^* adequately describes the elastic contribution to the deformation in the elastic-plastic indentation regime, whereas the amount of deformation are dictated by the ratio between the representative strain a/R in the sub-indenter region and the yield strain σ_0/E^*, thus confirming that the indentation degree depends on the dimensionless parameter $aE^*/(R\sigma_0)$. To establish the validity limits of the Hill's model for linear elastic-ideally plastic constitutive behaviours, the corresponding analytical predictions are also included in Fig. 2.6. The plot of the average pressure against the parameter $aE^*/(R\sigma_0)$ reveals that it exist a good agreement between the Hill's model predictions and the numerical results only for values of the ratio $aE^*/(R\sigma_0)$ approximately equal to 40-50. At larger values of this ratio the average pressure falls down and the normalizing parameter $aE^*/(R\sigma_0)$ ceases to uniquely define the amount of the indentation. In other terms, the elastic contribution to the deformation promoted by the indenter starts to be negligible at these values of the contact sizes. Indeed, as shown by the diagram of the average pressure versus the a/R (Fig. 2.6b), the actual normalizing parameter at these stages of the indentation process is effectively the ratio a/R: for values of such ratio greater than 0.16, in fact, the corresponding curves coalesce into a master curve.

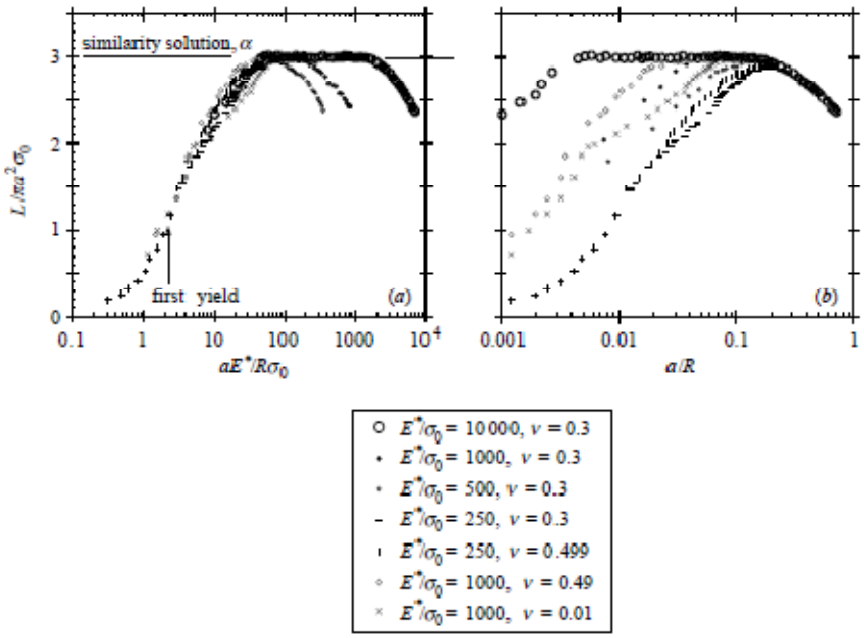

Figure 2.6 Frictionless spherical indentation response of linear elastic-ideally plastic media from [54]: (a) average pressure $L/(\pi a^2\sigma_0)$ as a function of $aE^*/(R\sigma_0)$; (b) average pressure as a function o fa/R.

It should be noted from both mentioned diagrams, however, that the maximum value of the average pressure predicted by the Hill's model is attained only by media having very low values of the yield strain, thus confirming that the self-similarity validity depends on the constitutive properties of the indented materials. In addition, the drop in average pressure with increasing contact size reveals that infinitesimal deformations assumption coupled to a monotonic radial strain path is not longer appropriate: such trend, in fact, can be explained only if the deformation in the sub-indenter region and

especially at points in contact with the indenter surfaces ceases to be infinitesimal and radial.

The validity limits of the Hill's model as well as the various regimes of deformations caused by frictionless indenters into linear elastic-ideally plastic media can be easily found by mapping the average pressure $L/(\pi a^2 \sigma_0)$ and the normalized contact area $a^2/(2hR)$ against the contact size a/R and the yield strain σ_0/E^*, on the base of the finite element computations. Fig. 2.7 shows an example of such maps: the results are obtained for E^*/σ_0 ranging from 3 to 10000 [54]. By analysing the map, five deformations regimes can be recognized. The hertzian regime, pertaining the half-space within which the Von Mises stress is less than the material yield strength, drives the indentation response at contact sizes $a/R < 2.5(\sigma_0/E^*)$. The elastic-plastic regime governing the material response within the region in which the normalized contact pressure increase with increasing parameter $aE^*/(R\sigma_0)$. Such regime is replaced by the similarity regime for yield strains σ_0/E^* values less than about $2\text{x}10^{-4}$ according to the following criterion: $a/R > 800(E^*/\sigma_0)$. On the other hand, if the contact pressure exceeds $2\text{x}10^{-4}$ finite-deformation plasticity regime supersedes the elastic-plastic regime at a contact size a/R of 0.16, approximately.

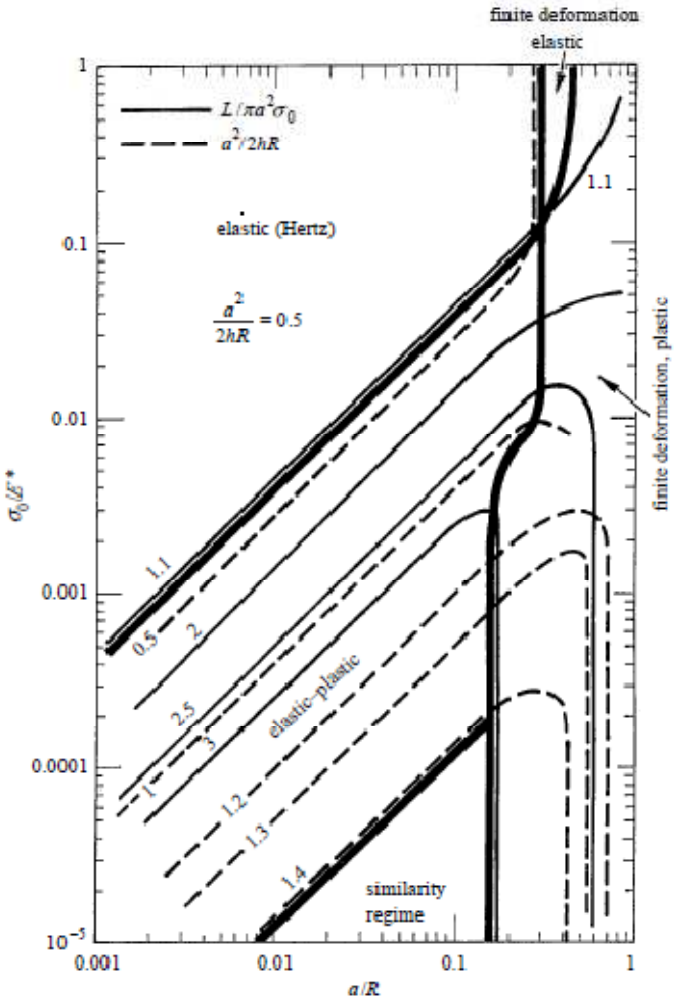

Figure 2.7. Frictionless spherical indentation response of linear elastic-ideally plastic media from [54]: indentation map and deformation regimes. The map also includes the contours of the average pressure (-) and normalized contact area (---). The map is based on the finite element results for E^*/σ_0 ranging from 3 to 10000.

Finally, at very large values of the yield strain ($\sigma_0/E^* > 0.1$) and contact size a/R finite-deformation elastic and plastic regimes dominates the material indentation response.

With regard to the indentation of linear elastic-strain hardening solids, the average pressure and normalize contact size trends versus the dimensionless parameter $aE^*/(R\sigma_0)$ are plotted in Fig. 2.8. Both diagrams refer to selected values of the yield strain and Poisson's ratio, whilst the work hardening *n* coefficient is assumed to be equal to 3. For convenience, as stated by the similarity solution (see equation (2.38)), the average pressure is scaled by the parameter $\sigma_r = \sigma_0[a/(\varepsilon_0 R)]^{1/n}$. The differences and analogies with their response of linear elastic-ideally plastic solids are evident: effects of work hardening and are evident: the parameter $aE^*/(R\sigma_0)$ still drives the trend of the average pressure but it acts differently when Hollomon or Ramberg-Osgood laws is assumed as the representative constitutive relationship. On the contrary, once the similarity regime is entered, the average pressure dependence on the constitutive law assumptions vanishes and no drops in average pressure are observed as the indentation proceeds for the considered value of the work hardening coefficient. This is consistent with the predictions of the Hill's model, being $n = 3$ the condition which corresponds the transition between sinking-in behaviour to piling-up behaviour. On the other hand, the evolution of the normalized contact area $a^2/(2hR)$ as a function of $aE^*/(R\sigma_0)$ allows to appreciate the validity limits of the theory proposed by Hill, even for the linear elastic-plastic hardening materials (Fig. 2.8b): the normalized contact area, in fact, increases in the elastic-plastic regime with increasing $aE^*/(R\sigma_0)$ and, after attaining a constant value (similarity regime), it starts to decrease again in the finite-deformation regime.

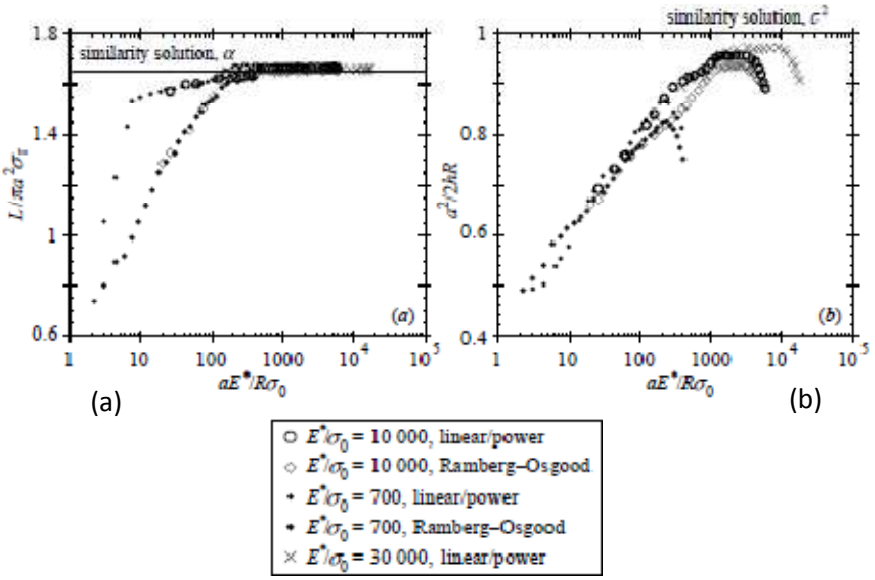

Figure 2.8. Frictionless spherical indentation response of linear elastic-plastic hardening solids [54]: (a) average pressure $L/(\pi a^2\sigma_r)$ as a function of $aE^*/(R\sigma_0)$ and (b) normalized contact area $a^2/(2hR)$ versus $aE^*/(R\sigma_0)$.

The validity limits and the indentation regimes for linear elastic-plastic hardening solids can be better appreciated if the corresponding indentation map is regarded. Fig. 2.9 shows the indentation map of Hollomon materials with $n = 3$. For comparison, the indentation map of linear elastic-ideally plastic solids is reported. Overall, the strain hardening coefficient has a barely effects onto the location of the boundaries separating the regimes, especially with regard to the similarity regime: in this case, in fact, the boundaries are mainly determined by the trend of the normalized contact area $a^2/(2hR)$, being the average pressure constant for a wide range of the contact size.

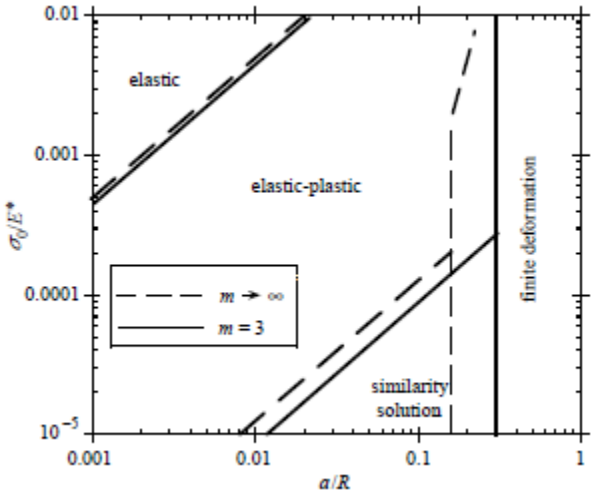

Figure 2.9. Frictionless spherical indentation response of linear elastic-plastic hardening media with $n = 3$ [54]: indentation map and deformation regimes. The boundaries pertaining the deformation regimes of linear elastic-ideally plastics solids are included for comparison.

2.3 Frictional effects onto the spherical indentation metallic materials response

In practical experimental tests the presence of friction between the indenter and the indented surface cannot be ignored. Friction is considered to produce remarkable effects in straining processes promoted by the indenter, and the difficulties which characterize the quantitative evaluation of friction forces and its potential variability during the indentation process makes the knowledge of its role in the material indentation response particularly crucial: material properties evaluation, in fact, cannot be affected by such kind of parameters. Although in literature there are several contributions focusing on this

issues [54,55,60], frictional effects onto the material indentation response are not well-established.

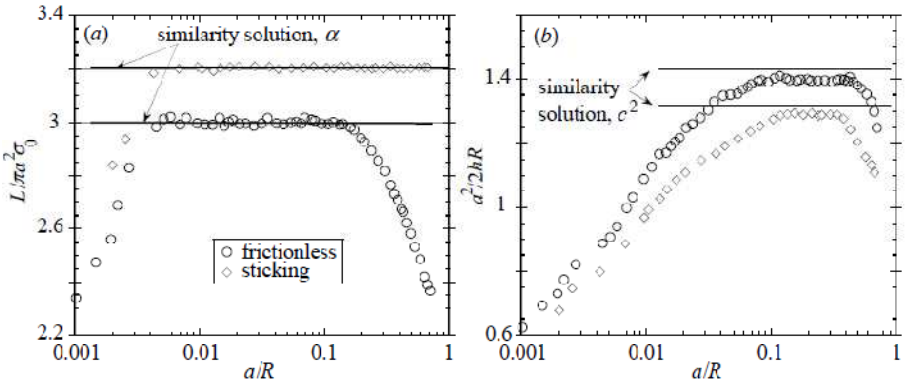

Figure 2.10. Frictionless and sticking indentation response of linear elastic-ideally plastic media with $\nu = 0.3$ [54]: (a) average pressure $L/(\pi a^2 \sigma_r)$ versus contact size a/R; (b) normalized contact area $a^2/(2hR)$ against a/R.

Mesarovic and Fleck [54] investigated the limiting case of sticking friction to establish the sensitivity of the indentation response to the friction level for linear elastic-ideally plastic solids. A comparison of frictionless and sticking indentation is illustrated in Fig. 2.10, for $E^*/\sigma_0 = 10^4$ and $\nu = 0.3$, whereas Fig. 2.11 depicts how the boundaries of deformation regimes are affected by the sticking condition, as obtained by the author's analysis. Figs. 2.10 and 2.11 also include the similarity solutions predictions in order to appreciate how the validity limits of such theory are affected by frictional effects. The attendant average pressure results markedly higher than for the case of frictionless indentation (Fig. 2.10a) and no drop in average pressure can be detected for a wide range of the contact size. In

contrast, a drop in normalized contact areas is detected as the contact size increases (Fig. 2.10b), thus proofing that high friction conditions in any case are not able to prevent any kind of transition among the indentation regimes. The potential transition among the afore described regimes can be better appreciated in Fig. 2.11 where the negligible effects of friction onto the location of the boundary are quite evident. By analysing the trend of the normalized contact area as a function of the contact size, it can be also deduced that sticking strongly reduces the contact area for a given penetration depth. These evidences are consistent with a deformation mechanism characterized by a remarkable plastic constraint on the strain field. In other terms, high friction seems to promote plastic strains mainly in the sub-indenter region, whereas it multi-axial stress conditions in the subsurface annular region surrounding contact zone (radial constraint effect) are induced, thus contrasting the local plastic flow. Accordingly, it should not be surprising if material piling-up results consistently reduced. Experimental measurements concerning crater geometry for lubricated and dry ball indentation performed by Stute [61] and distinct finite element analyses [55,60] confirm this constraint effect.

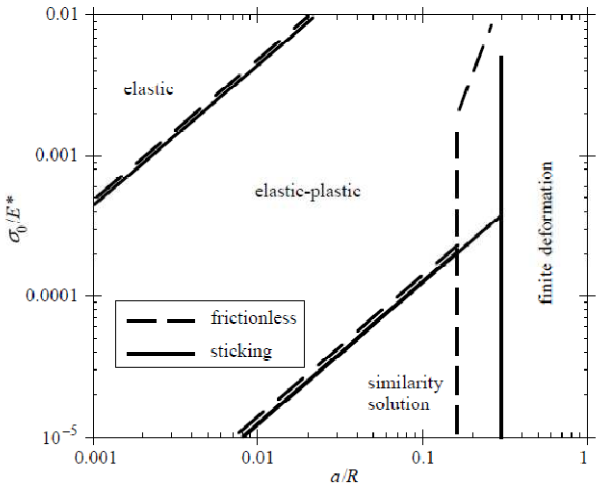

Figure 2.11. Frictionless and sticking indentation response of linear elastic-ideally plastic media with $\nu = 0.3$ [54]: indentation map and deformation regimes.

A similar scenario was found by Lee et al. [55], by analysing the plastic strains distribution in the sub-indenter region induced by spherical indenter for Hollomon media. Friction was introduced adopting the Coulomb's model. Friction coefficients ranging from 0.0 to 0.5 were considered. Taljat et al. [38] extended the investigation about the frictional effects onto the piling-up phenomena at the crater edge. To this purpose a proper finite element analysis of the indentation process was carried out. The craters profile evolution in elastic-plastic strain-hardening materials obeying to the Hollomon power law, having ratios E/σ_0 up to 10^3 and strain hardening exponents *n* ranging from 0.0 to 0.5, was analysed. Friction was implemented according to the Coulomb's model. Author's analysis revealed that frictional effects are relevant for materials having

relatively low yield strengths (i.e. large E/σ_0 ratios) and strain-hardening coefficients (small *n*). For such materials the material piling-up reduces with increasing the friction coefficient μ ($\mu = 0.0 \div 0.1$). Similar findings were obtained by Habbab et al. [62], after examining material piling-up amount for ratios E/σ_0 ranging from 560 and 840 and *n* between 0.132 and 0.250: crater ridge reductions greater than 50% when friction coefficient μ increases from 0.0 to 0.5.

Frictional effects onto the *L*-*h* curve have been also explored [28,54,55,58,59] via finite element analysis. Although there is not a clear comprehension of friction role from this point of view yet, a trend towards increasing values of the applied load *L* at a given penetration depth h was found [28,54,58,59]. Conversely, *L*-*h* curve seems to be barely affected by friction at low and medium relative indent depths h/D [54,55], whereas it cannot be ignored as the indentation achieves very large values of penetrations depth *h*. Recently, Cao et al. [59] extended the analysis of frictional effects on *L*-*h* curves for deep indentations. Elastic-perfectly plastic materials with E/σ_0 in the range 10^2-2x10^3, friction coefficients $\mu = 0.0 \div 0.3$ and relative indentation depths h/D up to 0.15 were considered. An increase of the indentation load *L* of 28% and 14% at relative penetration depths $= 0.15$ were observed for materials with E/σ_0 equal to 2x10^3 and 10^2 were observed, respectively.

2.1 Summary

The evaluation of material properties by instrumented spherical indentation testing requires a deep understanding of the deformation mechanisms promoted by the spherical indenter during the test. The present chapter showed that the characteristic indentation response represented by the characteristic *L*-*h* curve and the crater geometry impression is strongly related to the achieved indentation depth *h* and, depending on such variable, different competing indentation regimes can be experienced by the tested material. Under a set of simplifying hypotheses, analytical and numerical approaches proofed that it is possible to establish the driving material parameters governing each indentation regime, thus providing potential guidelines for developing future methodologies for inferring the constitutive laws of the indented materials. The present review also pointed out that friction plays a very important role in the definition of the material indentation response, especially with regard the stress and strain distributions and impression morphology evolution. On the contrary, minor effects seem to be produced in the characteristic load-indent depth curve if no deep penetrations are considered.

limiti principali: leggi constitutive ideali

manca un legame diretto tra la curva l-h ed la curva s-e del materiale

CHAPTER 3
Stress-Strain constitutive laws evaluation procedures

The previous chapter allowed to identify the typical response metallic materials to spherical indentation. It also allowed to establishing how and which kind of information coming from the indented material are collected by the indentation response: *L*-*h* curve and crater profile evolution. Complex straining mechanisms characterize materials indentation response and many variables affect the experimental data. Accordingly, proper analyses of the materials indentation response are needed to deduce the constitutive properties. Since multiple sources of information can be recognized in the indentation response of any material, different approaches can be adopted for estimating the material behaviour.

The present chapter discusses the most effective evaluation procedures now available in literature, emphasizing for each methods the basic principles and limits. The most critical features which can potentially affect the accuracy of the predictions are especially analyzed. Due to the implications on the evaluation procedures developed subsequently, Tabor's approach and Tabor's approach-based procedures are firstly addressed. Evaluation

procedures based on the analysis of the plastic strain fields in the sub-indenter region and the measured *L-h* curves are subsequently discussed.

3.1 Tabor's approach

Although the analysis of the indentation response of metallic materials can be dated back to the XIX century, the first attempt to deduce their constitutive laws was performed by Tabor [1].
Thanks to an extensive analysis of the experimental data, Tabor derived the following relationship,

$$\varepsilon_p = 0.2\,\frac{d}{D} \tag{3.1}$$

between the indentation representative plastic strain ε_p and the indentation parameters: the indenter diameter D and the impression diameter d. According to Tabor's approach, $d = 2\,a$ is the base diameter of the spherical cap impression caused by the indenter, whereas ε_p denotes the strain at the contact perimeter between the indenter and indented surface. Therefore, according to this approach, sinking-in and piling-up phenomena are ignored. Following the procedure [1], the corresponding stress σ_t is given by:

$$\sigma_t = \frac{p_m}{\psi} \tag{3.2}$$

in which p_m and ψ denote respectively the average pressure corresponding to the applied load L and the *constraint factor*

introduced to take into account that the effective stress state in the sub-indenter region is unlike to that in the uniaxial tension or compression test [41]. $\psi = 3$ and the following expression,

$$p_m = \frac{4\,L}{\pi d^2} \tag{3.3}$$

were proposed by Tabor on the base of the experimental data analysis. Eqns. 3.1-3.3 can be used to obtain the true stress – plastic strain curve of the indented material by performing a sequence of loading and unloading cycles, if the contact diameter d is known for each value of the load *L*.

Tabor's approach is undoubtedly characterized by very important advantages: it is easy to implement and allows to deduce point-to-point any kind of constitutive laws. Conversely, several disadvantages can lead to non negligible errors in the estimation of the material behaviour. At first, the evaluation of ε_p and σ_t requires the knowledge of the contact diameter d corresponding to the applied load *L*. Unfortunately, it is impossible to measure d during the experimental test. An estimation of d can be provided, if the elastic recover is negligible when the load *L* is removed: in this case the contact diameter d can be replaced with the diameter d_r of the residual circular border of the contact area. In other terms, according to the Tabor's approach, ε_p and σ_t can be evaluated on the base of the residual impression geometry only. Secondly, it should be noted that this approach does not account for the piling-up and sinking-in phenomena and the estimation of d_r may be fairly poor. Finally, to obtain the true stress-plastic strain curve, Tabor's approach requires

to perform a sequence of loading and unloading cycles, thus preventing any kind of investigation about the constitutive properties of the indented material in a specific points. To avoid potential alterations in the material indentation response, impressions must be carried out at a sufficient distance.

3.2 Modified Tabor's based approaches

According to the Tabor's approach, the evaluation of true stress-plastic strain curves is based on the assumption that the constraint factor ψ is fixed and equal to 3. However, on the basis of the analysis of a large amount of experimental results [40,41], it was found that the constraint factor ψ is correlated to the strain-hardening coefficient. The choice $\psi = 3$ is appropriate only for describing the indentation response of elastic-ideally plastic solids [1]. Francis [68] also proofed that ψ is a function of the indentation regime occurring in the core beneath the indenter and he proposed the following relationship,

$$\psi = \begin{cases} 1.1 & \varphi < 1.1 \quad \text{Hertzian regime} \\ 1.1 + 0.5 \log \varphi & 1.1 < \varphi < 27.3 \quad \text{Elastic} - \text{plastic regime} \\ 2.87 & \varphi > 27.3 \quad \text{Fully plastic regime} \end{cases} \tag{3.4}$$

for taking into account such dependence. Here, φ is a dimensionless parameter related to elastic strain at yielding onset of the indented material. A similar relationship was also found by Field and Swain [63]. Au et al. Taljat and et al. [64,65] suggested

$$\varphi = \frac{\varepsilon_p E_r}{0.43\ \sigma_t} \tag{3.5}$$

as expression for evaluating φ, where

$$E_r = \frac{1-\nu_1^2}{E_1} + \frac{1-\nu_2^2}{E_2} \tag{3.6}$$

denotes the reduced modulus. Adopting the notation proposed by Hertz, ν_1, ν_2 and E_1, E_2 are the Poisson's ratio and the Young's moduli of the indented material and the indenter, respectively. Haggag et al. [66,67] modified Francis's constraint factor and proposed a constraint factor depending on the strain rate and strain hardening,

$$\psi = \begin{cases} 1.12 & \varphi < 1 \quad \text{Hertzian regime} \\ 1.12 + \tau \log \varphi & 1 < \varphi < 27.3 \quad \text{Elastic} - \text{plastic regime} \\ \psi_{max} & \varphi > 27.3 \quad \text{Fully plastic regime} \end{cases} \tag{3.7}$$

where $\psi_{max} = 2.87$ and $\tau = (\psi_{max} - 1.12)/Ln(27)$.

It is apparent that a more accurate definition of the constraint factor ψ leads to a better estimation of the constitutive law of the indented material.

Further improvements to the Tabor's approach can be brought by implementing the results obtained by Taljat et al. and Au et al. [64,65]. As derived by Au et al. [64], it is possible to deduce the effective value of d, once the residual base diameter d_r is known, thus eliminating one of the uncertainness sources characterizing the Tabor's procedure. By applying Hertz theory [42,43], Au et al. [64] found that the following relationship,

$$d = \left(\frac{3LD}{E_r}\frac{h_r^2+(d/2)^2}{h_r^2+(d/2)^2-h_rD}\right)^{1/3} \quad (3.8)$$

between the aforementioned diameters, where h_r is the residual crater depth. Conversely, on the basis of an extensive finite element analysis, carried out to explore the material indentation response of elastic-plastic hardening solids, Taljat et al. [65] found that Eqn. (3.8) can be replaced by the following expression,

$$d = [h(D-h)]^{1/2} \quad (3.9)$$

in which h indicates the penetration depth at the load L. Therefore, using Eqn. (3.9), it is possible to deduce the constitutive law of the indented material by a single instrumented indentation test.

Although the aforementioned improvements allow to markedly reduce the potential error in the constitutive properties evaluation, it should be noted that the Tabor's procedure and modified Tabor's procedures are always based on an ideal representation of the impression produced by the spherical indenter. As discussed in Chapter 2, piling-up and sinking-in phenomena strongly characterize the crater geometry. A strong correlation between the material piling-up and sinking-in was found by Hill et al. [39]. Neglecting these phenomena leads to non negligible errors in the estimation of the average pressure p_m (see Eqn. (3.3)) and consequently in the computation of the stress σ_t. An interesting method based on this theoretical background and able to take into account the effective crater geometry in the stress-strain curve evaluation was proposed by Beghini et al. [56]. The evaluation procedure foresees the

determination of the strain-hardening coefficient n and the yielding stress σ_y of materials obeying to the Hollomon power law,

$$\sigma = \begin{cases} E\varepsilon & \varepsilon \leq \varepsilon_y \\ \sigma_y\left(\varepsilon/\varepsilon_y\right)^n & \varepsilon > \varepsilon_y \end{cases} \tag{3.10}$$

Here, ε indicates the total strain (elastic plus plastic), ε_y the strain at yielding onset and E the elastic modulus. The influence of the actual crater geometry d onto the stress-strain curve estimation was included by analysing the ratio, $C_d = d/d_r$, between the effective diameter d at the load L and the diameter d_r of the residual impression, as function of the applied load L, the strain-hardening coefficient n and the yielding onset σ_y. To this purpose an extensive Finite Element analysis (FE) was performed and the following power law dependence was finally derived by the authors [56],

$$C_d = C_0\left(n, \sigma_y\right)L^{M\left(n,\sigma_y\right)} \tag{3.11}$$

by fitting (via least square method) the FE results over a wide range of values of n and σ_y, $\left(200 \leq \sigma_y \leq 800, 0.0 \leq n \leq 0.5\right)$. Based onto this results, the authors developed an iterative procedure (Fig. 3.1) for deducing the unknowns n and σ_y of metallic materials obeying to the Hollomon power law. After collecting a sequence of K couples (L_k, h_k) at increasing loads and another sequence K couples (L_k, h_{rk}) pertaining to the unloading cycle, the effective diameter d, for anyone of the k^{th} couple is computed by Eqn. (3.9).

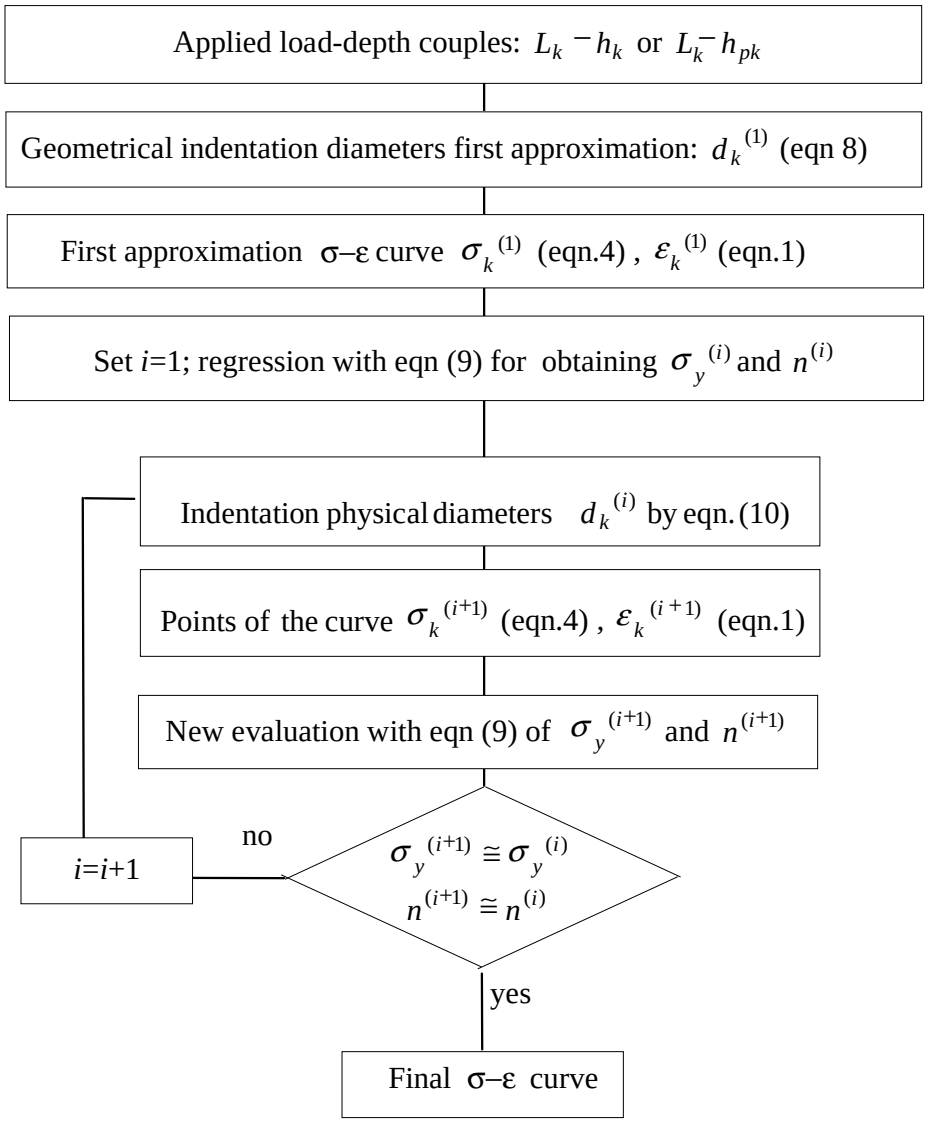

Figure 3.1. Beghini's iterative procedure for evaluating the strain-hardening coefficient n and the yielding stress σ_y of elastic-plastic hardening material obeying to the Hollomon's power law [56].

Therefore, putting the results of such computation Eqns. (3.1) to (3.3) and assuming the constraint factor $\psi = 2.87$, a first estimation of the

stress-strain curve k^{th} point can be obtained. Then, using Eqn. (3.9), the unknowns n and σ_y can be computed via least square fitting.These results can be subsequently used for making a better estimation of the effective contact diameter d by Eqn. (3.11). Obviously, the iterative procedure is repeated until an appropriate convergence criterion is satisfied.

Although the aforementioned methodologies allow to infer the constitutive properties of any generic metallic material, their validity is strongly limited by the practical difficulty to proof the reliability of the predictions referring to the crater geometry. It is a very difficult task to measure the crater profile left by the indenter. In addition, it should be noted that the afore described procedures do not account for the friction which plays a key role in the evolution of the crater profile [3,13,14].

3.3 Evaluation procedures based on the Reference Point Concept

3.3.1 Reference Point Concept

Adopting the Tabor's approach the determination of constitutive laws via spherical indentation can be solely performed for values of the plastic strain less than 0.2, as prescribed by Eqn. 3.1. However, this threshold is usually exceeded in many practical applications such as metal forming processes, thus representing an important limit to the application of the instrumented indentation. Accordingly, a theory

able to accurately predict stress-strain curves at large plastic strains is mandatory. Hill et al. and Sinclair et al. [39,68] showed that this limit can be easily overcome, following the Tabor's approach, by simply changing the point in which the plastic strain is evaluated. Therefore, to infer the constitutive behaviour at large plastic strains, it is sufficient to select a new *reference point* from which higher values than 0.2 of the plastic strain ε_p can be extracted. It is apparent that, changing the reference point, where the plastic strain ε_p is evaluated, leads to a new formulation of the constraint factor ψ. Also, new relationships correlating the indentation parameters to the plastic strain are needed. Finally, the definition of new reference points is not straightforward, being the strains distribution into the sub-indenter region affected by the contact conditions which are practically unknown during the test and generally characterized by high gradients [55]. In the next two sections the most powerful and interesting evaluation procedures based on this concept are presented.

3.3.2 Taljat's evaluation procedure

The procedure developed by Taljat et al. [65] probably represents one the most interesting applications of the reference point concept. It allows to determine the constitutive behaviour of indented materials at very low and large strains simultaneously. To this purpose, two reference points were defined. To deduce the constitutive behaviour at large values of the plastic strain, a first reference point was

selected where the plastic strains distribution attains maximum values. Conversely, the second reference point was selected in those regions in which the plastic strain field reaches minimum values, thus making it possible to infer constitutive relationships near the yielding point. In both cases, the selection was performed after exploring the plastic strains distribution beneath the indenter.

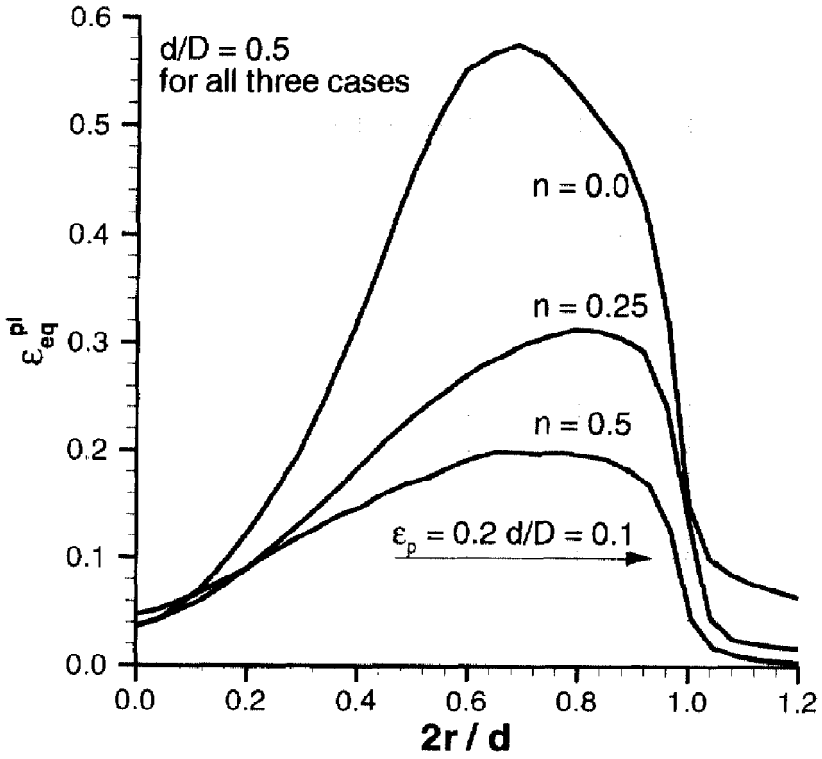

Figure 3.2. Taljat's evaluation procedure [65]: equivalent plastic strain distribution at the indentation edge for strain-hardening coefficients n between 0.0 and 0.5.

The analysis of the plastic strain field was performed via FE modelling of the indentation process into materials having strain-hardening coefficient n ranging from 0.0 to 0.5 and constant Young's

modulus and yield stress of 200 GPa and 400 MPa, respectively. Frictional and indenter compliance effects were also taken into account. Fig. 3.2 summarizes the results obtained by the authors with regard to the trend of the equivalent plastic strain ε_{eq}^{pl} at the indentation edge as a function of the normalized distance r/d from the indentation axis (r denotes the radial distance from the indentation centre). The plotted trends refer to a friction coefficient $f = 0.1$. The role played by the strain-hardening coefficient n can be also appreciated.

As shown by the FE results, the equivalent plastic strain ε_{eq}^{pl} reaches a maximum value at certain distance from the indentation axis, which is a function of the contact conditions. In the discussed case, maximum values up to 0.6 were attained. Therefore, if the reference point is fixed in this location, it is possible to determine the stress-strain curve up to these values of the plastic strain. By fitting the computed data, the authors established the following relationship,

$$\varepsilon_p = \left(0.5n + \frac{1.44}{\sqrt{n+0.1}} - 1.6\right)\left(\frac{d}{D}\right)^2 \qquad (3.12)$$

between the equivalent plastic strain ε_p and the indentation parameters. Since the correlation (3.12) contains the strain-hardening coefficient n, it also accounts for the piling-up and sinking-in phenomena. The constraint factor ψ dependence on the dimensionless parameter φ, the following expression,

$$\psi = \begin{cases} -0.65 + \ln(\varphi) & \text{Elastic} - \text{plastic regime} \\ -0.81 + \frac{2}{\sqrt{n+0.2}} & \text{Fully plastic regime} \end{cases} \qquad (3.13)$$

was finally derived by simply fitting the FE results. A plot of ψ versus φ is shown in Fig. 3.3.

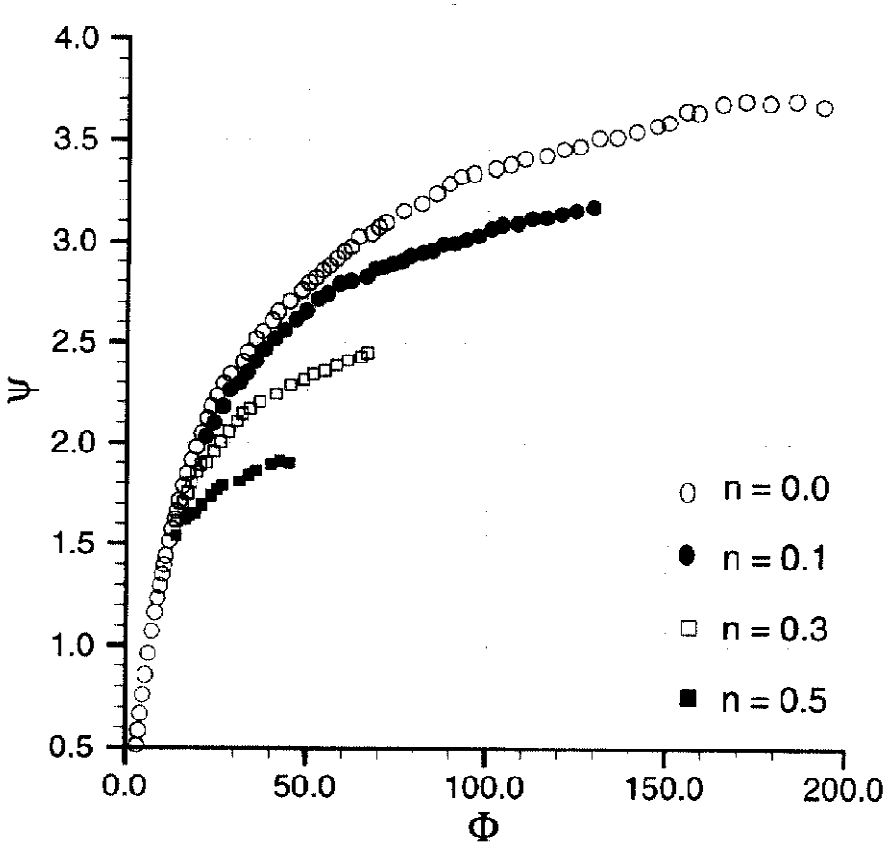

Figure 3.3. Taljat's evaluation procedure [65]: ψ versus φ trends for the representative stress and strain values at the contact edge and for different values of the strain-hardening coefficient n.

Following this procedure, the correlations between the plastic strain corresponding to the second reference point and the constraint factor ψ, from one side, and the indentation parameters and the strain-

hardening coefficient n, on the other side, can be derived. According to the authors [] analysis,

$$\varepsilon_p = \left(-2 + 0.87n + \frac{1.47}{\sqrt{n+0.36}}\right)\left(\frac{d}{D}\right)^{2.45-0.85n} \quad (3.14)$$

is the correlation correlating ε_p to the ratio d/D, whereas the dependence of ψ on n was found to be given by the following expression:

$$\psi = (3.65 - 4.30n^2 + 4.36n^3)\left(\frac{d}{D}\right)^{\left(-3.18n^2+2.89n^3\right)} \quad (3.15)$$

The set of Eqns. (3.12) to (3.15) coupled to Eqns. (3.2) and (3.3) can be used to determine the constitutive behaviour, once a estimation of the strain-hardening coefficient n is provided. Taljat et al. [65] suggested several possibilities for determining this unknown variable: via an appropriate analysis of the *L-h* curve or by measuring the residual crater profile. More details about this estimation can be found in [17].

Although the evaluation procedure developed by Taljat et al. [65] appears a very attractive tool for evaluating any kind of stress-strain curves for any values of the plastic strain, a deeper analysis of the method and its basic principles reveals several crucial issues which may affect the accuracy of the results. These criticalities can be easily recognized by examining the trend of the equivalent plastic strain ε_{eq}^{pl} at the indentation edge (see Fig. 3.2). The distribution of the equivalent plastic strain in this point is clearly characterized by high gradients and is surely dictated by the friction conditions

between the contacting bodies [39,54,65]. Therefore, it should not be surprising, if the high strain gradients, on one side, and the tangible effects of friction, on the other side, make really hard to have a reliable estimation of stress-strain curves. Moreover, the reference point selection does not take into account the dependence on the penetration depth. As shown by Hill et al., Johnson and Mesarovic and Fleck [39,44,54], the plastic strains distribution varies during the indentation process, thus resulting in a potential modification of the locations where the equivalent plastic strain field takes the maximum or minimum values. Finally, in developing the evaluation procedure, Taljat et al. [65] did not include the variation of the yield strain. The method is valid only for a specific value of the yield strain, thus lacking of practical use.

3.3.3 Lee's evaluation procedure

A partial answer to the issues characterizing Taljat's evaluation procedure can be found in the investigation performed by Lee et al. [55]. The authors analysed the plastic strains field into the sub-indenter region at the maximum indentation depth and probed the existence of a reference point location, in which the strain gradients and frictional effects can be neglected. FE modelling of the indentation process into metallic materials obeying to the Hollomon power constitutive law was performed to this purpose. Frictional effects were also included, by considering friction coefficients f ranging from 0.0 to 0.5.

Fig. 3.3 illustrates the trends obtained by the authors for the equivalent plastic strain ε_p as a function of the normalized distance from the indentation axis $(2r/d)$ and normalized depth (l/D) under the indented surface.

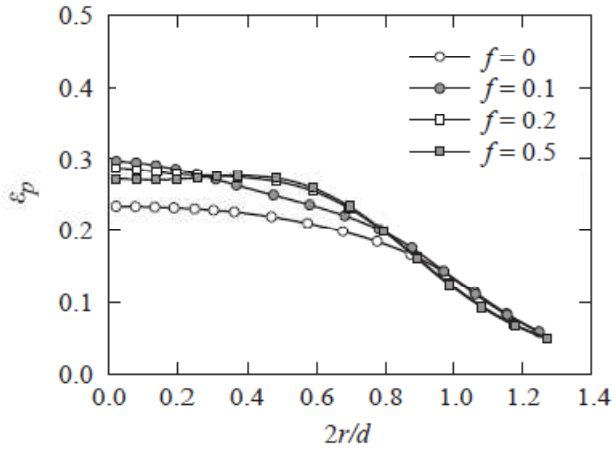

(a)

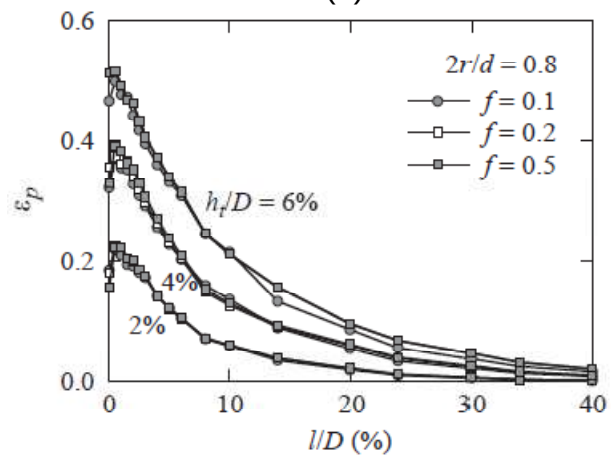

(b)

Figure 3.3. Lee's evaluation procedure [55]: equivalent plastic strain distributions versus (a) the normalized distance from the indentation axis $(2r/d)$ at a normalized depth $l/D = 0.1$ and (b) against l/D at $2r/d = 0.8$.

Both plots refers to the stage (d/D) of the indentation process corresponding to the maximum indentation depth.Both plots proofs that trictional effects can be ignored if the reference point location is fixed at a normalized distance $2r/d = 0.8$ (Fig. 3.3a) and normalized depth $y/D = 0.1$ under the indented surface (Fig. 3.3b). At this location, strain gradients are also negligible. This point was selected by Lee et al as new reference point.

Based on these results, Lee et al. [55] developed a novel numerical approach for obtaining automatically the elastic-plastic properties of metallic materials. The constitutive framework is represented by the Hollomon power law,

$$\frac{\varepsilon}{\varepsilon_y} = \begin{cases} \sigma/\sigma_y & \sigma \le \sigma_y \\ \left(\sigma/\sigma_y\right)^n & \sigma > \sigma_y, \end{cases} \qquad 1 < n \le \infty \tag{3.16}$$

in which ε and ε_y denote the total strain (elastic plus plastic) and the yield strain respectively, whereas σ_y and n the yield stress and the strain-hardening coefficient.

To find the constitutive properties without having recourse to extra processes, as in Taljat et al. and Haggag's [65-67] indentation theories, the material properties defining the constitutive framework were firstly inter-correlated. To this aim, it is sufficient to note that Eqn. (3.16) can be rearranged as below,

$$\sigma = \sigma_y\left(\varepsilon/\varepsilon_y\right)^{1/n} = K\varepsilon^{1/n} \tag{3.17}$$

by a regression of the stress-strain data. As Eqn. (3.17) is also valid for $\sigma = \sigma_y$, then

$$\sigma_y = K\varepsilon_y^{1/n} \tag{3.18}$$

whilst the elastic stress-strain relation takes the following form

$$\sigma = E\varepsilon_y \tag{3.19}$$

at the yielding point. Here, E is the Young's modulus of the indented material. By rearranging Eqns. (3.17) to (3.19), the following inter-correlation between the material properties can be obtained:

$$\sigma = (K^n/E)^{1/(n-1)} = E(K/E)^{n/(n-1)} \tag{3.20}$$

The evaluation procedure obviously follows the Tabor's approach. The actual projected contact diameter d at loaded state with pile-up and sink-in,

$$d = 2\sqrt{hD - h^2} = 2\sqrt{c^2 h_t D - (c^2 h_t)^2} \tag{3.18}$$

is evaluated from the geometric shape of the spherical indenter, where h and D denotes the actual indentation depth at loaded state and the indenter diameter. h_t is the nominal depth measured from the original surface.

As aforementioned, one of most important limitations in Taljat's procedure [65] is represented by the fact that the methodology lacks of practical use, since the role played by the yield strain was not taken into account. As shown by Lee et at. [55], it is possible to implement this dependence by correlating the yield strain to the effective crater geometry, the equivalent plastic strain ε_p at the reference point and, finally, the corresponding constraint factor ψ.

Such correlations can be easily determined by simulating the spherical indentation process via FE method. The ratio $c^2 = h/h_t$ was introduced to evaluate the effects of the yield strain onto the crater geometry.

The dependence of the aforementioned parameters on the yield strain can be determined once the relationships between c^2, ε_p and ψ , from one side, and the strain-hardening coefficient n, from the other side, are known. If the Young's modulus E and yield strength are fixed, the following functional forms can be used,

$$c^2 \equiv h/h_t = f^c(h_t/D\,, n) \tag{3.19}$$

$$\varepsilon_p = f^n(h_t/D\,, n) \tag{3.20}$$

$$\psi = f^{\psi}(h_t/D\,, n) \tag{3.21}$$

for expressing the dependence between c^2 , ε_p and ψ and the indentation parameters and strain-hardening coefficient n . To establish the formulae (3.19) to (3.21), Lee et al. [55] analyzed 13 values of the strain-hardening coefficient n, ranging from 1.001 to 50, and the following relationships,

$$c^2 = f_0^c(n) + f_1^c(n)\ln\left(\frac{h_t}{D}\right),\ f_i^c(n) = a_{ij}n^{-j},\ i = 0{,}1,\ j = 0,,4 \tag{3.22}$$

$$\varepsilon_p = f_i^{\varepsilon}(n)\ln\left(\frac{h_t}{D}\right)^i,\ \ f_i^{\varepsilon}(n) = b_{ij}n^{-j}, \qquad i = 0,,3,\ \ j = 0,,4 \tag{3.23}$$

$$\psi = f_i^{\psi}(n)\ln(h_t/D)^i,\ f_i^{\psi}(n) = c_{ij}n^{-j}, \quad i = 0,,3,\ \ j = 0,,4 \tag{3.24}$$

relating c^2 , ε_p and ψ to n were found on the basis of the FE results.

To establish the relationships between these three characteristic parameters $(c^2, \varepsilon_p, \psi)$ and the yield strength ε_y, Lee et al. [55] analysed 364 cases in which the Young's modulus E and the yielding stress σ_y were considered to vary between 100 GPa and 400 GPa and 200 MPa and 800 MPa, respectively, thus covering a wide range of the engineering materials. In this case the regression of the FE solutions provided the following expressions:

$$c^2 = f_0^c(\varepsilon_y, n) + f_1^c(\varepsilon_y, n)\ln(h_t/D), \qquad f_i^c(\varepsilon_y, n) = a_{ij}(\varepsilon_y)n^{-j},$$

$$i = 0,1, \qquad j = 0,,4$$

$$a_{ij}(\varepsilon_y) = \alpha_{ijk}\varepsilon_y^k \qquad k = 0,,3 \tag{3.25}$$

$$\varepsilon_p = f_0^\varepsilon(\varepsilon_y, n) + f_1^\varepsilon(\varepsilon_y, n)\ln(h_t/D), \qquad f_i^\varepsilon(\varepsilon_y, n) = b_{ij}(\varepsilon_y)n^{-j},$$

$$i = 0,,3, \qquad j = 0,,4$$

$$b_{ij}(\varepsilon_y) = \beta_{ijk}\varepsilon_0^k \qquad k = 0,,3 \tag{3.26}$$

$$\varepsilon_p = f_0^\psi(\varepsilon_y, n) + f_1^\psi(\varepsilon_y, n)\ln(h_t/D), \qquad f_i^\psi(\varepsilon_y, n) = c_{ij}(\varepsilon_y)n^{-j},$$
$$i = 0,,3, \qquad j = 0,,4$$
$$c_{ij}(\varepsilon_y) = \gamma_{ijk}\varepsilon_y^k \qquad k = 0,,3 \tag{3.27}$$

As regards to the coefficients, the values can be found in the annexes of the quoted contribution [55]. It is now clear how the constitutive properties (see Eqn. (3.16)) can be estimated. Starting from the *L*-*h* curve, Eqns. (3.22) to (3.27) can be used to calculate the characteristic parameters $(c^2, \varepsilon_p, \psi)$ and actual projected contact

diameter d at loaded state for each *L*-*h* depth data point on the *L*-*h* curve and used to evaluate the values of n, K and ε_y from the stress-strain relationship. The Young's modulus may be computed following the procedure developed by Oliver et al. or Pharr et al. [24,26,69].

From the analysis of the evaluation procedure developed by Lee et al. [55] three important criticalities emerge: the selection of the reference point, the assessment of the prediction concerning the crater geometry and finally the accuracy of the fitting procedures. The reference point is selected by analyzing the plastic strain distribution when the maximum penetration depth *h* is attained. However, as shown by Mesarovic and Fleck [54], the size of the region affected by the contact conditions is a function of the penetration depth. Consequently, the choice of the reference point should be also related to the penetration depth. Secondly, due to the difficulties to accurately measure the impression during the experimental indentation test, it is impossible to carry out a validation of the numerically predicted crater profiles. Finally, the presented fitting procedures were performed always on numerical data but it lacks an estimation of the error which these fitting procedures introduce in the final prediction of the material stress-strain curve.

3.4 Evaluation procedures based on the Representative Strain Concept

3.4.1 Representative Strain Concept

The estimation of the material properties via instrumented indentation using the Dimensional Analysis was firstly rationalized by Cheng and Cheng [35,70-72]. Subsequently, Dao et al. [73] applied the dimensional analysis results to introduce the concept of the Representative Strain as a new tool for evaluating stress-strain curves of ductile materials. In both cases, sharp indenters were considered. Cao et al. [58,59] extended the definition of representative strain to spherical indentation and presented new evaluation procedures for obtaining stress-strain curve from the load-indentation depth curve.

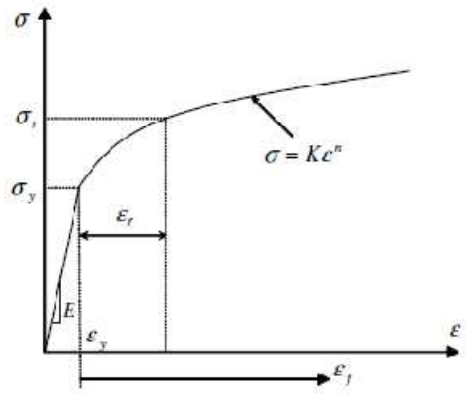

Figure 3.4. Hollomon constitutive law. Schematic representation and associated nomenclature [58].

Since this concept is based on a specific set of assumptions and is centered on a particular constitutive framework, before presenting the most important evaluation procedures based on this concept, it is mandatory to deeply discuss the background beyond the definition of the representative strain.

Although in some cases it may produce a poor description of the materials plastic behavior, the classical Hollomon power law (see Eqn. 3.16) provides a good approximation of the material response, when the yielding onset is exceeded, for many ductile materials. The importance of this constitutive law increases, if it is considered that, as observed by Lee et al. [55] the yielding onset is well defined and only two independent parameters are sufficient to describe the material behavior at these stress states: the yield stress σ_y and the strain-hardening coefficient n.

Adopting this constitutive framework, during the loading cycle of the indentation process and when the yielding occurs, the indentation load *L* must depend on the following independent parameters only: the Young's modulus, E_1, and the Poisson's ratio, ν_1, of the indented material, the Young's modulus, E_2, and the Poisson's ratio, ν_2, of the linear-elastic indenter, the yield strength, σ_y, the strain-hardening coefficient, n, the indentation depth, h, and, finally, the indenter radius, R. In a functional form:

$$L = f(E_1, \nu_1, E_2, \nu_2, \sigma_y, n, h, R) \tag{3.28}$$

Using the reduced Young's modulus E^*, Eqn. (3.28) can be rewritten as

$$L = f(E^*, \sigma_y, n, h, R) \tag{3.29}$$

When $\sigma > \sigma_y$, the constitutive equation (3.16) can be rearranged as follow,

$$\sigma = \sigma_y \left(1 + \frac{E_1}{\sigma_y}\varepsilon_f\right)^n \quad (3.30)$$

where in this case ε_f indicates the total effective strain accumulated beyond the yield strain ε_y (Fig. 3.4). Let us denote with σ_r the flow stress defined at $\varepsilon_f = \varepsilon_r$. As indicated by Eqn. (3.30) σ_r is a function of ε_r. In terms of σ_r, Eqn. (3.29) can be rewritten as

$$L = f(E^*, \sigma_r, n, h, R) \quad (3.31)$$

where σ_r can be computed by Eqn. (3.30). As shown by Barenblatt [74], by applying the Π theorem, Eqn. (3.31) involving $k = 5$ independent variables can be equivalently reduced to an equation of $k - m$ dimensioless parameters, being m the number of the fundamental used units. In this case, $m = 2$ and consequently, Eqn. (3.31) takes the following form:

$$L = \sigma_r h^2 \Pi_1 \left(\frac{E^*}{\sigma_r}, n, \frac{h}{R}\right) \quad (3.32)$$

where the dimensionless function Π_1 relates the material indentation response to the material properties, once the indentation depth h and the indenter radius R are fixed. It is possible to select a representative strain ε_r, in order to obtain a dimensionless function Π_1 independent on the strain-hardening exponent, thus making it possible to deduce the unknown plastic properties (σ_y, n) only by evaluating Eqn. (3.32) at two different penetration depths: by means of Eqns. (3.30) and (3.32), in fact, two different values of the representative stress are sufficient to obtain the yield stress σ_y and

the strain-hardening coefficient n. However, the determination of these two variables strongly depends on the knowledge of how the representative strain ε_r is correlated to the indentation response. In other terms, the knowledge of the correlation between the representative strain ε_r and the normalized indentation depth h/R is needed. Such dependences can be easily obtained by performing a proper numerical analysis of the indentation process aimed at establishing how the indentation response depends on the normalized indentation depth h/R and on the constitutive properties of the indented material.

In developing new methodologies for obtaining the constitutive properties of ductile materials, Zhao et al. and Cao et al. [28,58] successfully implemented the representative strain concept. to underline the criticalities of the evaluation procedures based on the representative strain concept, the aforementioned methods are described in detail in the next two sections. It should be noted that adopting the representative strain concept leads to a very important limit regarding the constitutive law which can be determined by analysing the material indentation response. With respect to the above presented procedures, here only Hollomon power laws can be inferred. From this point of view, Tabor's approach is much more powerful.

3.4.2 Cao's evaluation procedure

As discussed in the previous section, the evaluation of the relationship between the representative strain ε_r and the normalized indentation depth h/R is mandatory for the determination of the plastic properties of ductile materials obeying to Hollomon power law, when the representative strain concept is adopted. Such relationships can be easily established via Finite Element modelling, by exploring how the characteristic *L-h* curve varies as a function of the elastic-plastic properties, i.e. the Young's modulus E, the yield stress σ_y and the strain-hardening coefficient n. To this purpose, Cao et. al [58] developed a new FE model able to simulate the indentation process induced by rigid and frictionless indenters. With regard to the properties of the indented material, the Hollomon power law was assumed. In the investigation the Young's modulus was varied from 10 to 210 GPa, the yield stress from 30 to 2000 MPa and, finally, the strain-hardening coefficient from 0.0 to 0.5. Indeed, Poisson's ratio was fixed to 0.3.

On the basis of the numerical results, dimensionless function $\Pi_1$was determined. Fig. 3.5 illustrates the effect of the selection of ε_r on the form of the dimensionless function Π_1 for a normalized indentation depth $h_g/R = 0.06$. It is apparent that the representative strain $\varepsilon_r = 0.0316$ makes the dimensionless function Π_1 independent on the strain-hardening exponent n. The relationship relating the representative strain ε_r to the normalized indentation depth h_g/R is shown in Fig. 3.6.

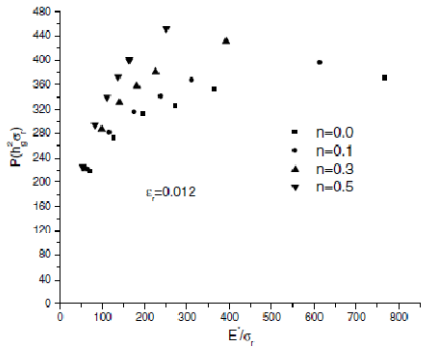

(a)

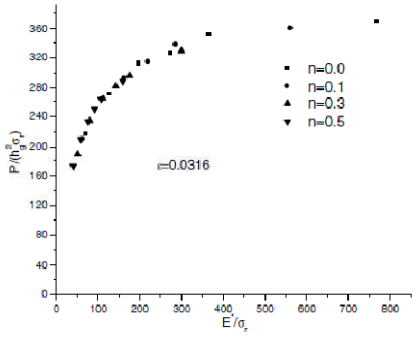

(b)

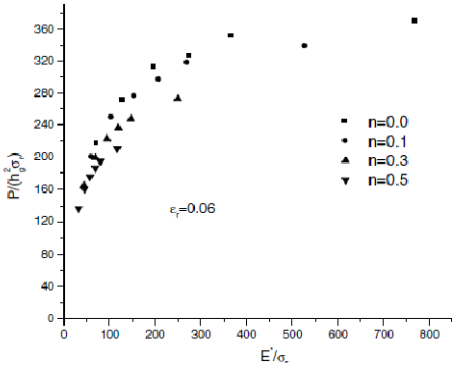

(c)

Figure 3.5. Dimensionless function Π_1 for the normalized indentation depth $h_g/R = 0.06$ and three different values of the representative strain ε_r [58]: (a) $\varepsilon_r = 0.012$, (b) $\varepsilon_r = 0.0316$ and (c) $\varepsilon_r = 0.060$.

Second-order polynomials were found to fit very well the function $\varepsilon_r = \varepsilon_r(h_g/R)$ and the following expression was provided by the authors,

$$\varepsilon_r\left(\frac{h_g}{R}\right) = 0.00939 + 0.435\frac{h_g}{R} - 1.106\left(\frac{h_g}{R}\right)^2 \qquad 0.01 \le \frac{h_g}{R} \le 0.1 \quad (3.33)$$

as a functional form of $\varepsilon_r = \varepsilon_r(h_g/R)$, whilst the dimensionless function Π_1 was expressed as

$$\Pi_1\left(\frac{E^*}{\sigma_r}\right) = C_1 Ln^3\left(\frac{E^*}{\sigma_r}\right) + C_2 Ln^2\left(\frac{E^*}{\sigma_r}\right) + C_3 Ln\left(\frac{E^*}{\sigma_r}\right) + C_4 \quad (3.34)$$

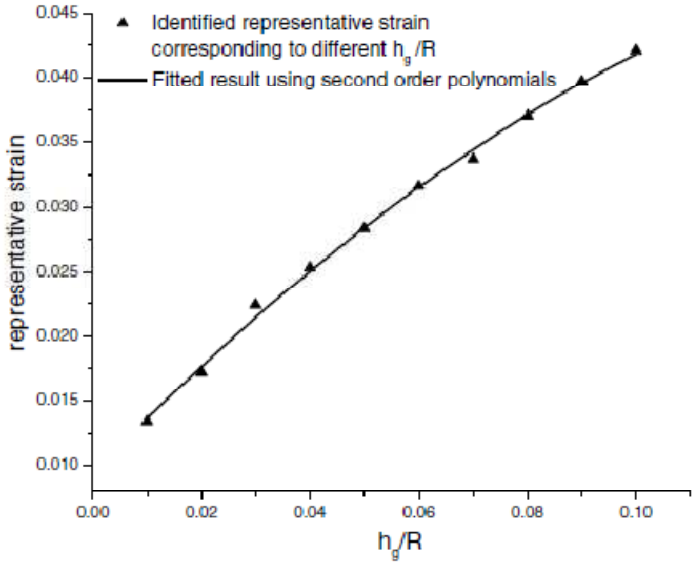

Figure 3.6. Cao's plastic properties evaluation procedure: representative strain ε_r against normalized indentation depth h_g/R and fitted trend by second-order polynomials [58].

Therefore, after extracting from the characteristic *L-h* curve two distinct couples of points (h, L), two distinct values of the representative stress σ_r can be calculated via Eqns. (3.32) and (3.34). Then, putting these results into Eqns. (3.30) and (3.33), the unknown plastic properties σ_y and n can be finally deduced. With regard to the evaluation of the reduced modulus E^*, the procedures developed by Oliver et al. and Pharr et al. [24,26,69] or Dao et al. [73] can be used.

It should be noted that the evaluation of the plastic properties of the indented material according Cao's procedure is performed in a frame in which the friction between the contacting bodies is neglected. However, during an experimental test the presence of friction cannot be ignored a priori [55]. The determination of the role played by the friction and how it affects the representative strain ε_r versus the normalized indentation depth h/R should be deeply assessed. A partial analysis of the role played by the friction together to novel definitions of the representative strain can be found in [59].

3.4.3 Zhao's evaluation procedure

If the methodology developed by Cao et al. [58] is analysed in detail several crucial steps can be recognized. First of all, the definition of the representative strain ε_r; secondly, the accuracy of fitting functions on which the estimation of the plastic properties critically depends; thirdly, the ranges amplitudes inside which the reference properties are allowed to vary and are used to evaluate the correlation between

the representative strain and the normalized indentation depth h/R and the dimensionless function Π_1. Finally, the numerical model architecture used to explore the material indentation response. Of these criticalities, Zhao et al. and Ogasawara et al. [28,75] probed that the definition of the representative strain ε_r and the range used to evaluate the functions $\varepsilon_r = \varepsilon_r(h/R)$ and $\Pi_1(E^*/\sigma_r)$ are surely the most crucial aspects: the latter can especially hide significant errors. These can be easily recognized in the Cao's procedure by analysing Fig. 3.5b. In Eqn. (3.30) $\sigma_r = \sigma_y$ when $n = 0$, whilst it rapidly increases as n increases for any value of ε_r. Hence, the ranges of both $\frac{L}{\sigma_r h^2}$ and $\frac{E^*}{\sigma_r}$ for larger values of n become much more smaller when compared with those corresponding to $n = 0$: as shown by Fig. 3.5b, in fact, the largest value of $\frac{E^*}{\sigma_r}$ is about 700 for $n = 0$, whereas it is smaller than 200 when $n = 0.5$. Accordingly, even though $\frac{L}{\sigma_r h^2}$ seems to be independent on the strain-hardening coefficient, this is probably due to the fact that the considered range of values are to small for larger values of n.

With these key issues in mind, Zhao et al. [] proposed a new procedure for determining the elastic-plastic properties of ductile materials obeying to Hollomon power law. Inspired by a work of Ogasawara et al [75], Zhao et al. [28] defined the representative strain ε_r as the plastic strain ε_p contribution to the total effective strain ε, thus assigning a strong physical meaning to the representative strain concept. On the basis of this assumption, Eqn. (3.30) takes the following form:

$$\sigma = \sigma_y \left[\frac{E^*}{\sigma_y}\left(\frac{\sigma_r}{E^*} + \varepsilon_r\right)\right]^n \tag{3.35}$$

Consequently, for two values of the indentation depths, $(h_1/R = 0.13\,, h_2/R = 0.3)$, corresponding to two distinct values of the applied load, (L_1, L_2), the following expressions,

$$\begin{cases} L_1 = \sigma_r h_1^2 \mathrm{f}_1\left(\frac{E^*}{\sigma_r}, n\right) \\ L_2 = \sigma_r h_2^2 \mathrm{f}_2\left(\frac{E^*}{\sigma_r}, n\right) \end{cases} \tag{3.36}$$

can be derived by Eqn. (3.32).

As probed by Meyer [34], during the loading cycle of an indentation process the applied load does not scale exactly with h^2 and the representative strain concept as used by Cao et al. [58] does not work well. In other terms, there is no a representative strain ε_r such that the dimensionless function $\mathrm{f}_1\left(\frac{E^*}{\sigma_r}, n\right)$ and $\mathrm{f}_2\left(\frac{E^*}{\sigma_r}, n\right)$ in Eqn. (3.36) are independent on the strain-hardening coefficient n. It is possible, however, to minimize this apparent dependence by adjusting the representative strain and stress (see Eqn. 3.35) via least square methods.

To evaluate the correlation between the representative strain ε_r and the normalized indentation ratio h/R as well as the dimensionless functions $\mathrm{f}_1\left(\frac{E^*}{\sigma_r}, n\right)$ and $\mathrm{f}_2\left(\frac{E^*}{\sigma_r}, n\right)$, the authors developed a new Finite Element model able to simulate spherical indentation processes induced by rigid spherical indenters. The FE model was built-up taking into account the friction between the contacting bodies. Friction was implemented according to the Coulomb's friction law and

a value of 0.1 was chosen for the friction coefficient. With regards to the material properties of the indented bulk, the ratio $\frac{E^*}{\sigma_r}$ was varied between 2 and 3000, whilst n from 0 to 0.6. Fig. 3.7 depicts the best fitted dimensionless functions $\mathrm{f}_1\left(\frac{E^*}{\sigma_r}, n\right)$ and $\mathrm{f}_2\left(\frac{E^*}{\sigma_r}, n\right)$ provided by the computational analysis. In both plots the dependence of the two functions on the strain-hardening coefficient n can be appreciated, when the ratio $\frac{E^*}{\sigma_r}$ is fixed, thus confirming the fact that the applied load L does not scale exactly with h^2. Nevertheless, although this apparent dependence on the strain-hardening coefficient n, the novel definition of the representative strain coupled to the minimization via least square methods of the dependence on n of the dimensionless functions $\mathrm{f}_1\left(\frac{E^*}{\sigma_r}, n\right)$ and $\mathrm{f}_2\left(\frac{E^*}{\sigma_r}, n\right)$, enable the determination of the plastic properties of the indented material: as seen in the previous section, in fact, Eqns. (3.35) and (3.36) are sufficient for obtaining the yielding stress σ_y and the strain-hardening coefficient n, thus definitely defining the Hollomon power law used for describing the constitutive behaviour of the indented material, if the Young's modulus is assumed to be known. Nevertheless, as probed by Zhao et al. [28], it is also possible to deduce the Young's modulus by applying the representative strain concept. To this purpose, it is sufficient to apply the dimensional analysis to the correlation between the contact stiffness S and the material elastic properties, i.e. the reduced Young's modulus E^*.

Eqn. (3.37) represents the results:

$$S = h_2 E^* \mathrm{g}\left(\frac{E^*}{\sigma_r}, n\right) \tag{3.37}$$

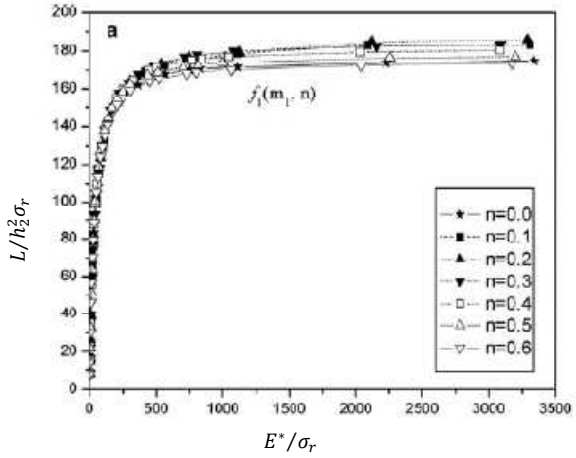

(a)

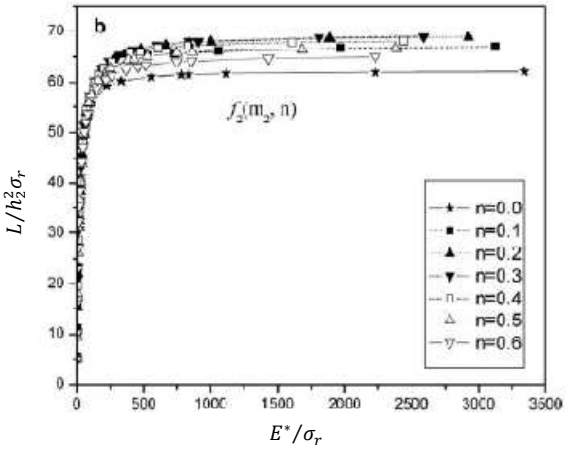

(b)

Figure 3.7. Zhao's evaluation procedure [28]: (a) dimensionless function $\mathrm{f}_1\left(\frac{E^*}{\sigma_r}, n\right)$ and (b) $\mathrm{f}_2\left(\frac{E^*}{\sigma_r}, n\right)$ against the ratio $\frac{E^*}{\sigma_r}$.

Once the dimensionless function $\mathrm{g}\left(\frac{E^*}{\sigma_r}, n\right)$ has been determined, by fitting the numerical results according to the procedure described above, eqn. (3.37) can be added to the set of eqns. (3.35) and (3.37), thus obtaining a set of equations which can be used for inferring uniquely the elastic-plastic properties of the indented materials.

3.5 Evaluation procedures based on the Load-Penetration Depth Curve Analysis

Guessing the constitutive properties by comparing the experimental *L-h* curve of the indented material with an *L-h* curve artificially generated and corresponding to a known constitutive framework can represent a very attractive and powerful alternative. However, to successfully implement this idea a constitutive framework and a comparison criterion must be firstly defined. Moreover, being impossible to create an infinite database of curves for covering all the possible combinations of the constitutive parameters chosen to describe the material behaviour, an automatic procedure for generating a generic *L-h* curve from a finite number of predefined curves must be identified, thus ensuring the existence of a comparison term for any measured experimental curve.

approaches based on a direct correlation between the *L-h* curve and the corresponding stress-strain curve can be found in Nayebi et al. [76,77]. The proposed method foresees the approximation of the *L-h* curve by a polynomial function determined via FE modelling of spherical indentation processes into elastic-plastic materials obeying

to Hollomon power law (see eqn. (3.16)). With regards to the functional form of the characteristic *L*-*h* curve, the authors assumed that the indentation depth h was related to the applied load L trough the following expression:

$$h = A(\sigma_y, n) L^{B(\sigma_y, n)} \tag{3.38}$$

where $A(\sigma_y, n)$ and $B(\sigma_y, n)$ are two functions determined by fitting the FE solutions. Yield stresses σ_y and strain-hardening coefficients n ranging from 200 to 800 MPa and 0.08-0.24 were considered for obtaining the dependences on σ_y and n of the functions A and B. Indeed, the Young's modulus of the indented materials was maintained fixed and equals to 210 GPa. Using an optimization procedure, the error between the proposed theoretical curve (eqn. (3.38)) and the experimental *L*-*h* curve was minimized and the two unknown variables (σ_y, n) finally determined. Although the procedures developed by Nayebi et al. [76,77] are characterized by a remarkable simplicity, it lacks of practical use because of only a materials class has been accounted for evaluating the theoretical form of the *L*-*h* curve. Moreover, the authors do not specify how the optimization procedure works and which type of error is minimized.

A more elaborated method based on the same idea was proposed by Beghini et al. [57]. In this case too, the constitutive framework represented by the Hollomon power law was considered for generating the theoretical *L*-*h* curves. Several combination of the material parameters (E, σ_y, n) were considered in order to map a wide domain, thus covering the properties of the most common

metallic materials. More exactly, the authors analysed three distinct classes of materials: Al-alloys having a Young's modulus $E = 70$ GPa, Cu-alloys with $E = 120$ GPa and steels for which E was assumed to be equal to 205 GPa. As the Young's modulus can be considered approximately constant within each material class, whereas the Poisson's ratio is near to 0.3 for almost all metals, the constitutive parameters were reduced to the yielding stress σ_y and the strain-hardening coefficient n. For these three materials classes, specific ranges, within the yielding stress and strain-hardening coefficient were allowed to vary, were identified and database of *L*-*h* curves finally defined via FE modelling.

By analysing the whole database of simulated *L*-*h* curves, the following expansion [78] ,

$$\frac{L}{ED^2} = \sum_{k=1}^{3} A_k \left(\frac{h}{D}\right)^{k/2} \tag{3.39}$$

was found to accurately fit each curve within any considered materials class. Here, D indicates the indenter diameter, whereas E the elastic modulus denoting each material class. The best fitting coefficients A_k were computed for any combination of the yielding stress σ_y and the strain-hardening coefficient n. The fitting coefficients A_k were also calculated for the three materials classes. Least square fitting method and the following two-dimensional polynomial function

$$A_k = \sum_{i=1}^{6} \sum_{j=1}^{6} \alpha_{ijk} \sigma_y^{i-1} n^{j-1} \tag{3.40}$$

were used to evaluate the fitting parameters A_k. The following expansion,

$$\frac{L}{ED^2} = \sum_{k=1}^{3}\sum_{i=1}^{6}\sum_{j=1}^{6}\alpha_{ijk}\sigma_y^{i-1}n^{j-1}\left(\frac{h}{D}\right)^{k/2} \quad (3.41)$$

were obtained by the authors as the representative expression of the theoretical *L*-*h* curve.

The reverse analysis was performed after choosing a proper criterion for comparing the experimental L^{exp}-h^{exp} curve with a reference L^{th}-h^{th} curve corresponding to a known couple of values σ_y and n. The typical output provided by an instrumented indentation test is represented by a sequence of M couples of measured values $L_m^{exp} - h_m^{exp}$ with $m = 1, \dots, M$. Thus, the authors proposed the following function

$$\chi(E, \sigma_y, n) = \sum_{m=1}^{M}\left[L^{th}\left(h_m^{exp}, E, \sigma_y, n\right) - L_m^{exp}\right]^2 \quad (3.42)$$

to measure the global distance between the experimental points $L_m^{exp} - h_m^{exp}$ and the theoretical curve corresponding to the material properties (E, σ_y, n). For inferring the constitutive parameters of the Hollomon power law from the experimental *L*-*h* curves, the estimation of the constitutive parameters is carried out by implementing Eqn. (3.42) in an optimization procedure [78] which scans the domain (σ_y, n) and selects the theoretical curve which minimizes the function $\chi(E, \sigma_y, n)$. According to the authors, the problem convexity ensures the existence of the minimum and the rapid convergence to the solution for any considered set of experimental points.

3.5 Summary

The most promising evaluation procedures developed to deduce the constitutive laws of the elastic-plastic materials were reviewed in the present chapter. The review were especially carried out in order to highlight the main criticalities which can potentially affect the accuracy of the predictions. The analysis showed that the estimation of the constitutive properties of metallic materials can be carried out by analysing the crater geometry and the plastic strains field beneath the indenter or the characteristic load-indentation depth curve. Numerical modelling was observed to play a key role for exploring the materials indentation response. Many computational FE models based on different simplifying assumptions were developed, but the effects of such assumptions onto the model response were not well documented. The lack of an experimental validation of the numerical predictions arose and a frontier between the experimental response and the numerical predictions emerged. Numerical predictions were always obtained for ideal materials and did not take into account the effective experimental conditions. From this point of view, the role of friction was not deeply analyzed, even if it is known that it affects the crater profile evolution and the plastic strains field in the sub-indenter region significantly.

CHAPTER 4
Materials and methods

The previous review of the indentation theories and procedures, aimed at investigating the behaviour of metallic materials on the basis of their indentation response, probes the lack of a bridging between the experimental response and the predictions of analytical and/or numerical models. It is author's opinion that it is impossible to accurately and reliably describe the indentation response of any material adopting only one of these two tools, even though properly designed. An integration of the experimental and analytical and numerical methods is needed, especially if the investigation of the indentation response is aimed at building-up new methodologies for inferring the materials constitutive properties from instrumented indentation testing. For an appropriate interpretation of the experimental response, it is paramount to establish and understand the phenomena behind the experimental data. Therefore, one of the goals of this Ph.D project is to develop a new integrated tool able to fully describe the spherical indentation response of metallic materials and provide all the information to be used for correctly interpreting the experimental measurements. The present chapter is accordingly devoted to present the new testing machine and the computational

model specifically developed for exploring the indentation response of metallic materials and how these two distinct tools can be successfully integrated for inferring the constitutive properties of ductile materials by the analysis of their indentation response.

4.1 Indentation testing machine

4.1.1 Technical Specifications and Features

To characterize the spherical indentation response of ductile materials from the experimental point of view, a new testing machine, denominated *Diaptometro* (from the Greek: device for measuring indentation depth), was specifically designed and developed. The design and its development was carried out in collaboration with the University of Pisa and Scienzia Machinale S.r.l. and Fig.4.1 shows one of the first two prototypes produced by Scienzia Machinale, now available at the University of Trento.

For sake of brevity, a general description of the adopted design solutions will be provided in the present section in order to show how the high level of the experimental measurements accuracy are achieved by the *Diaptometro*. However, the interested reader can found a detailed description of this new testing machine in [79].

Inspired to the evaluation procedure proposed by Beghini et al. [57,80], the *Diaptometro* is at the moment able to measure the characteristic load-indentation depth curves and deduce from the indentation response the elastic-plastic properties of three common classes of engineering materials (Steels, Cu-alloys and Al-alloys) via

a proper software based on the results of this Ph.D. project. Thanks to the promising results obtained by Beghini et al. [57,80] from this new testing machine, the evaluation procedure was patented [81].

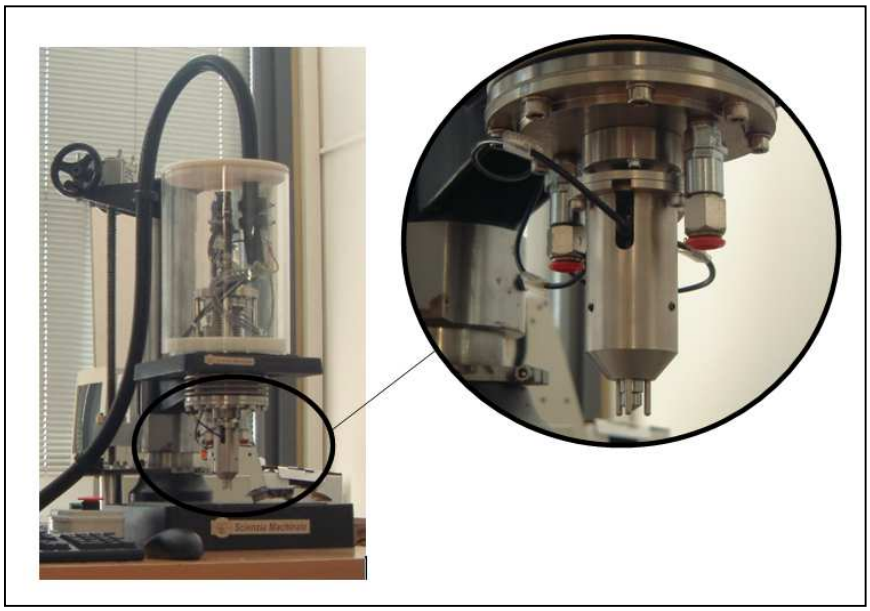

Figure 4.1. The new testing machine used to characterize the indentation response of metallic materials, now available at the University of Trento.

The design of the testing machine was based on the Technical Specifications summarized in Tab. I.

Table 4.I. *Diaptometro* Technical Specifications.

LOADING AXIS	Maximum linear excursion	2 mm	Maximum error	5 μm
LOAD CELL	Maximum load	2000 N	Maximum error	10 N
INDENTER	Tungste-Carbide Ball		Diameter	1.5 – 5.0 mm

The new testing machine can perform instrumented indentation tests onto any kind of ductile materials and a maximum load of 2000 N can be attained, with a resolution of 0.2 N, during the experimental test, thus making it possible to investigate even the indentation response of the hardest metallic materials. If requested, the *Diaptometro* can also carry out repeated loading-unloading indentation cycles. No potential strain-rate effects are involved in the experimental measurement, because of the maximum velocity with which the indenter is driven against the specimen is 1 μm per second, thus ensuring that the experimental data are collected under quasi-static conditions. Indentations are performed via Tungsten-Carbide balls having a diameter varying in a wide range of diameters, from 1.5 to 5 mm. The choice of the more appropriate indenter diameter is left to the user, even if it should be related to the characteristic size of the indented material microstructure: to obtain, in fact, a response which can be actually considered as representative of the whole material, a certain number of grains must be deformed. The approach suggested by Ashby [82] for selecting the most appropriate materials for a specific design solution was adopted.

The *Diaptometro* performs the indentation test under displacement control and range of 2 mm was chosen as maximum indenter excursion. The testing machine is equipped with instruments ensuring accuracy and resolution on the indenter displacement of 4 μm and 0.2 μm, respectively. Thanks to its reduced dimensions, the *Diaptometro* can be successfully used on very small samples (characteristic sample length: 20mm). A portable version is also

under development and it will allow to analyze in-service components.

4.1.2 Testing machine Supporting System

The new testing machine is composed by two main mechanical parts: the Indentation Unit (IU) and the Supporting System (SS) (Fig. 4.2). While the IU is designed to effectively perform the indentation onto the target material, the SS represents the frame of the testing machine and drives the alignment of the IU. Depending on the user needs, different SS design solutions can be adapted to the testing machine. It is apparent that the IU represents the most important part of the *Diaptometro*, being this unit designed to carry out the indentation process and collect the indentation data, i.e. the applied load *L* and the attendant penetration depth *h*. The IU composes of two mechanical components: the mechanical actuator and the loading unit. While the primer component is devoted to the movement of the indenter, the latter contains the spherical indenter and the acquisition system for measuring the load, via load cell, and the indentation depth curve via LVDT transducers.

The mechanical actuator was designed in order to minimize the overall dimensions. To reduce the manufacturing costs and especially to prevent the proliferation of mechanical components which can also affect the accuracy of the results, the most simple design solution was challenged.

Figure 4.2. The *Diaptometro* Supporting System (SS) and Indentation Unit (IU).

To avoid the presence of mechanical components requiring low tolerances and over constraining the whole system, gearboxes and worm gears were excluded and the classical handling mechanism of hydraulic presses was adopted as inspiring principle (Fig. 4.3).

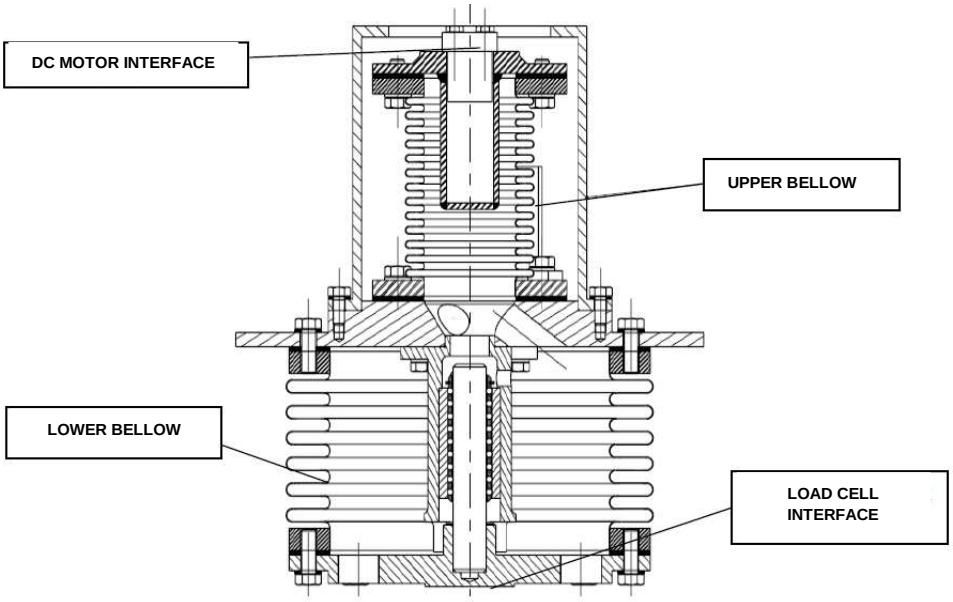

Figure 4.3. The Diaptometro main mechanical parts [79]: section view of the hydraulic actuator adopted by the *Diaptometro* for the indentation head handling. The mechanical bellows and the interfaces with the load cell and the DC motor are outlined.

However, the IU handling was not entrusted to the classical actuating system composed by cylinders, O-Rings and pistons, because of it needs of lubrication, low tolerances and especially because it may introduce un-controlled stick-slip phenomena affecting the accuracy of the *L*-*h* curve measurements, especially if repeated loading-unloading indentation cycles are programmed by the user. An handling system composed by two metallic bellows containing hydraulic oil at a pressure of 2.5 bar was preferred, thus obtaining high levels of deformability from the actuating system. Since a non-conventional handling system was adopted, a proper Finite Element Analysis, aimed at evaluating the relationship between the resulting

load *L* applied to the indenter and the displacement of both bellows, was carried out [79]. The designed system was found to be free of any phenomena of dry friction and backlashes which can affect the IU control.

4.1.3 Testing machine Indentation Unit

The 2D-drawing showing the longitudinal section view of the IU is reported in Fig. 4.4.

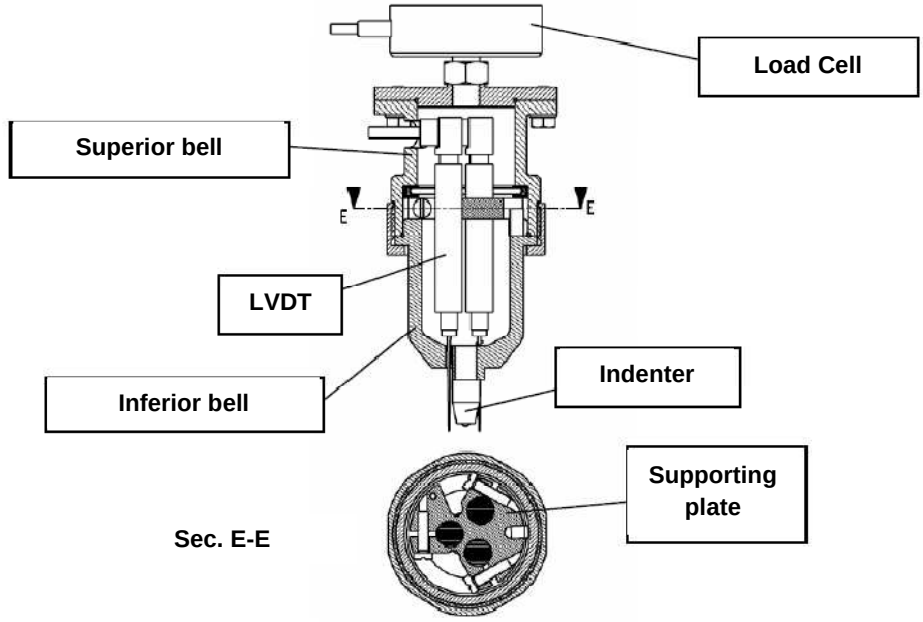

Figure 4.4. The *Diaptometro* main mechanical parts: longitudinal section view of the IU. In the first prototype, the acquisition system was composed by three LVDT placed at different radial distances from the spherical indenter and angularly spaced of 120°.

The IU composes of six main parts: two metallic bells, a supporting bell acting as IU frame, the load cell and the LVDT transducers representing the measuring apparatus and finally the indentation head which support the spherical indenter.

Two main constraints were taken into account in the design of this part and especially with regard its layout. On one side, the overall dimensions of the IU must be as small as possible, thus making it possible to adapt this solution to a portable testing machine; on the other side, the measuring apparatus must be located such that the spurious effects on the measurement of the penetration depth, due to the loading axis compliance, are minimized.

With regard the choice of the position sensors, linear contacting displacement sensors were preferred: roughness, conductive properties of the target and ferromagnetism can interfere, in fact, with the operating principles of non-contacting displacement sensors, thus limiting their range of applicability. Among the available options, LVDT transducers were adopted. This kind of analogical sensors are inexpensive and compatible with the expected range of measurement and can also provide high values of resolution. In order to minimize the planarity errors of the target and their effects onto the experimental data, the measuring apparatus was firstly provided by three LVDT transducers placed at different radial distances from the indenter along directions angularly spaced of 120°. In order to simplify the design and reduce the overall dimensions of the IU, in the last version of the IU the transducers were mounted at the vertexes of an equilateral triangle inscribed into a circle 7 mm in

radius. No modifications were observed in the experimental results adopting this new design solution. Finally, to measure the applied load *L*, the IU were equipped with a miniaturized load cells consisting of a resistive membrane strain-gauge.

4.1.4 Testing machine zero setting

Fig. 4.5 shows a schematic representation of the typical output provided by the *Diaptometro* with regard the experimental trend of the load-indentation depth curve. This output is provided via an software implemented in the *Diaptometro*. Loading and unloading cycles are recorded by the testing machine. However, the experimental data are characterized by an unknown offset along both coordinate axes *L* and *h*. This evidence is obviously related to the impossibility in establishing a priori the effective start of the indentation process. It is apparent that these data cannot be processed for obtaining any kind of information about the material properties of the indented material. Therefore, a definition of the zero point representing the beginning of the experimental test is needed.

As regards to the offset of the experimental curve along the *L* axis, the definition of zero is obtained by applying the Chauvenet's criterion [83], usually used for determining the potential outliers of a samples set. The beginning of the test, in fact, is characterized by a phase during which the load cell does not measure any significant load variations, even though the three LVDT are in contact with the target.

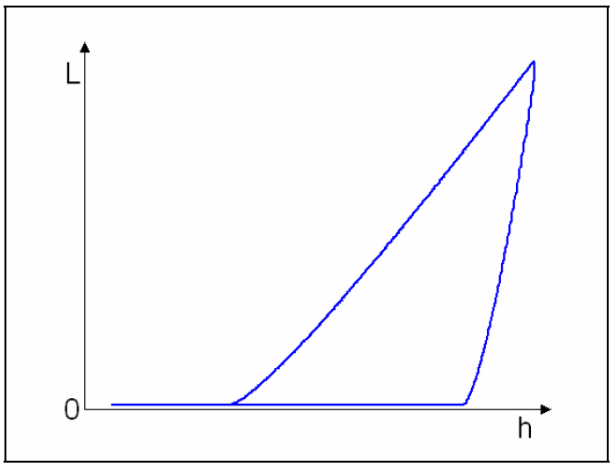

(a)

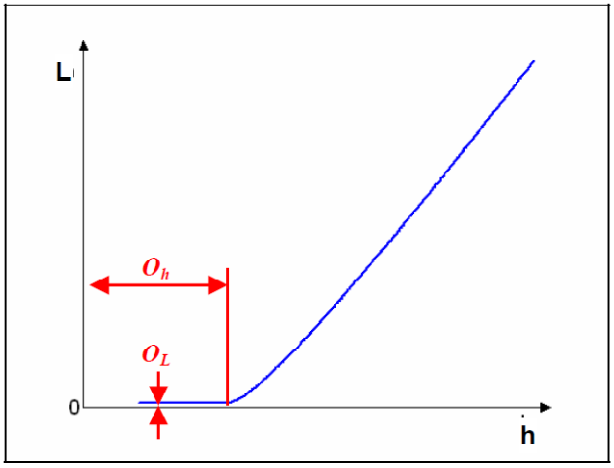

(b)

Figure 4.5. Experimental data analysis system [83]: (a) schematic representation of the experimental load-indentation depth curve measured by the *Diaptometro* showing the unknown data offset along both coordinate axes and (b) loading curve offset driving parameters.

Load variations can be appreciably detected only when the indentation process effectively starts to occur. The threshold below which the experimental points couples must be rejected, can be determined by evaluating the moving average of an increasing set of experimental points and comparing the obtained results, according to the Chaunevet's criterion, with a prescribed tolerance. Once this tolerance is exceeded, the set of the experimental points, which must be rejected, is fully defined and the corresponding threshold established. In this frame, a effective estimation of the offset can be represented by the load average O_L of the selected experimental points couples (L, h) and it can be used to translate all the experimental points couples (L, h) along the *L* axis, thus obtaining the new definition of the zero. The selected experimental points couples (L, h) used to compute O_L are obviously erased before translating the curve.

The Chaunevet's criterion can be indirectly used to define the new zero along the *h* axis: the set of experimental data, obtained after removing the points couples which satisfy the Chaunevet's criterion, can be interpolated by an appropriate function. It is apparent that the interpolation function must be the same used to deduce the elastic-plastic properties of the indented material. For example, adopting the evaluation procedure proposed by Beghini et al. [57], Eqn. (3.41) can be used to interpolate the set of experimental points couples. Therefore, once the interpolation function is defined, the determination of the offset along the *h* axis, O_h, is determined. To this purpose it is sufficient to evaluate the intersection between the interpolation function and *h* coordinate axis.

The software implemented in the *Diaptometro* is able to automatically determine these two quantities, thus enabling any kind of data processing for estimating the constitutive behaviour of the indented material. It should be noted, however, that the final output depends on the choice of the interpolation function used to represent the experimental *L*-*h* curve of the target material.
In chapter 6 the most appropriate interpolating function adopted for representing the characteristic *L*-*h* curve is presented. This function is now implemented in the *Diaptometro* and used to define the new "zero".

4.2 Computational modelling of the spherical indentation test

4.2.1 Model Formulation

To investigate the indentation response of ductile materials and correlate the experimental data with the phenomena occurring in the region beneath the indenter, a new parametric Finite Element Model able to simulate spherical indentation processes was developed with the Ansys Rel.11.0 software [84]. As any numerical predictions cannot be accepted without a previous experimental validation, the effective experimental test conditions were taken as reference in FE model development, thus making it possible the comparison between the numerical results and the experimental findings. In other terms, the FE model was built-up in order to reproduce as truly as possible the indentation process performed by the *Diaptometro*. The FE

computational model was built-up by deeply investigating the role played by each modelling assumption on the model output.

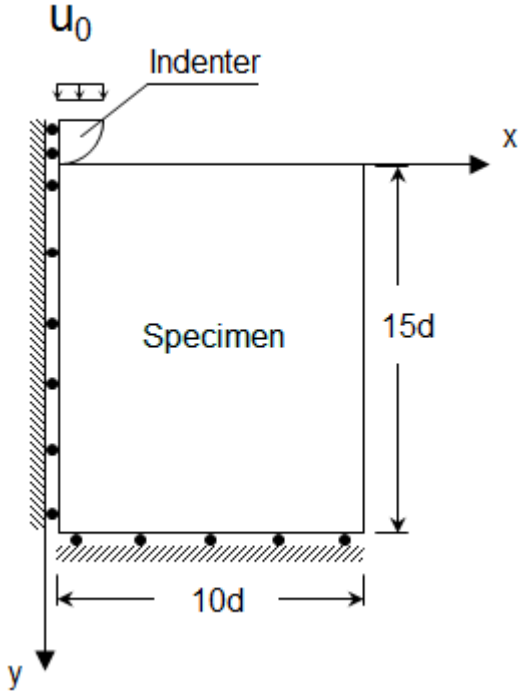

Figure 4.6. Spherical indentation test modelling: conceptual scheme of the computational model developed to simulate the indentation process.

The conceptual scheme of the FE model is depicted in Fig. 4.6. As the deformation processes involve the indenter and the target, only these two parts were modelled. Taking advantage of the problem axi-symmetry, the indenter was modelled as an hemi-sphere of diameter *d*. According to the spherical indenter used in the experimental test, the diameter *d* was chosen. Targets were implemented into the FE model as cylinders 10*d* in radius and 15*d* in height. These dimensions were found to correctly reproduce the traction free

surface condition at the lateral surface of cylinder, thus eliminating the boundary effects in the model response [56,57].

Roller boundary conditions were applied at the bottom surface of the specimen by constraining the displacements along *y* direction, whereas the axi-symmetric behaviour was implemented by imposing the appropriate symmetry boundary conditions along the indentation axis. As regard to the loading conditions, these were implemented by enforcing a uniform displacement u_0 on the equatorial cross-section of the hemi-sphere along *y* direction, toward the specimen. Accordingly, the attendant force applied to the indenter was evaluated as the sum of the reaction forces acting on the indenter along the *y* direction.

Both the indenter and the specimen were assumed to be homogeneous and isotropic. As regards to the constitutive behaviour of the indenter, linear-elastic behaviour was assumed. The Young's modulus E and the Poisson's ratio ν were taken equal to 630 GPa and 0.22, respectively: these values are identical to those of the material (WC-Co) effectively used for manufacturing the spherical indenters employed by the *Diaptometro*. The typical behaviour and especially the high compressive and tensile strengths of these advanced materials ensure the correctness of linear-elastic behaviour assumption. However, to evaluate the effects of the indenter compliance onto the model response, the rigid indenter formulation was also accounted for.

The classical frame of metals elasto-plasticity was implemented for the target. Von Mises's criterion and J_2 flow theory were adopted as yielding criterion and flow rule, respectively. Since it is impossible to

establish a priori how the stress states evolve in the sub-indenter region during the indentation process, both kinematic and isotropic hardening rules were implemented. The elastic-plastic portion of the true stress-true strain curve was finally input into the model via piecewise linear curve approximation.

Target were meshed using both four-nodes supporting the full and reduced integration as element technology for evaluating the stiffness element matrix. Eight-nodes structural axi-symmetric element was not used because the corresponding shape functions produce a different prediction capability at element corner-nodes and mid-nodes, thus introducing discontinuities in the predicted strain field. This phenomenon was also observed by Mesarovic and Fleck and Lee et al. [54,55]. The same four nodes element type was used to mesh the indenter when the indenter compliance effects was investigated. In order to establish the mesh density ensuring mesh independent results, different meshes were developed and analysed.

The modelling of contact was implemented by meshing the contact surfaces with two-nodes *surface to surface* elements. *Node to node* and *node to surface* contact elements were not used because they are not appropriate to model this kind of contact conditions [85]. With regards to the contact algorithm, Augmented Lagrangian Multipliers method (ALM) was preferred to the Penalty method for implementing the contact between the indenter and the target. This choice was motivated by the fact that, the ALM method minimize the effects of driving contact parameters, especially the contact stiffnesses, onto the model response [85]. For these parameters, in fact, due to their intrinsic nature, it is very difficult, if not impossible, to establish the

appropriate value, even by carrying out extensive sensitivity analyses [85]. As the role of friction still represents an open issues, friction was taken into account, according to the Coulomb's model, using friction coefficients ν ranging from 0.0 to 0.5, being this a reasonable range within which the friction coefficient ν can vary when a WC-Co indenter is driven against a metallic materials.

Finally, to take into account the stiffness changes resulting from the modifications of elements shape and orientation and occurring when the indentation depth *h* reaches medium or high values, with respect to the indenter diameter, large strain and deflection effects were activated.

4.2.2 Basic Issues of computational modelling qualification

Although blunt indentation tests may appear easy to model, the large number of different numerical approaches available in literature and the multiple choices required by the simulation of this kind of problems confirm that the simulation of such processes is not a straightforward task. The criticality of such modelling especially increases when the aim of the computation model is the estimation of the indented material properties. The role played by each numerical parameter and the effects of each assumption must be investigated, in order to prevent non negligible errors which can significantly the accuracy and reliability of the material properties evaluation. For these reasons, a considerable effort of the present research was

devoted to firstly qualify the computational model used to simulate the indentation processes into metallic materials.

The extensive review of the evaluation procedures, carried out in the previous chapters, outlined the most crucial issues concerning the numerical modelling of spherical indentation tests. By comparing the large number of developed numerical models, the mesh density, the element technology, the indenter compliance and, finally, the role of friction between the contacting bodies, result to be the most important factors. The computational model qualification was consequently carried by analysing the model response keeping in mind these issues. However, only the first three issues are investigated in this section, whereas the role of friction onto the model response will be analyzed in the next chapter, being it a key parameter for the indentation response.

As observed by Mesarovic and Fleck, Lee et al. and Taljat et al. [54,55,65], in fact, this parameter remarkably affect the evolution of the plastic strain field during the indentation process, thus resulting in a paramount parameter for the choice of the best stress-strain curve evaluation procedure.

4.2.3 Mesh density and mesh typology convergence

In order to establish the mesh density ensuring mesh-independent model response, different meshes having the elements characteristic size e in the contact region varying between 0.5% and 0.001% of the indenter diameter D were tested.

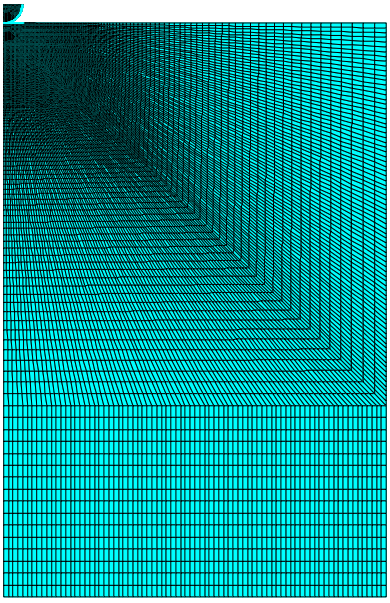

(a)

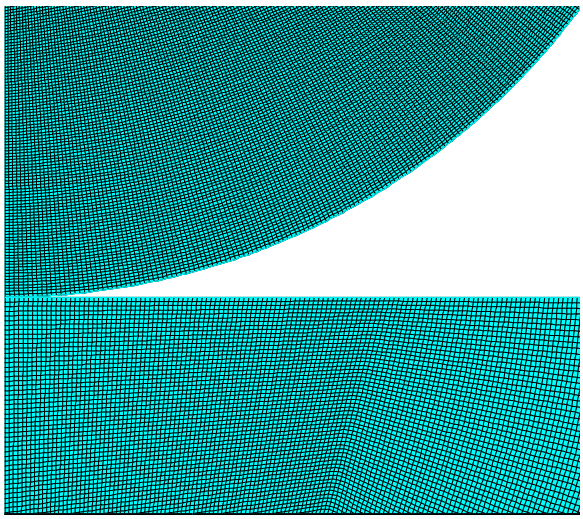

(b)

Figure 4.7. Finite Element discretization of deformable indenter-target system: (a) the global view of mesh and (b) detail of the contact region.

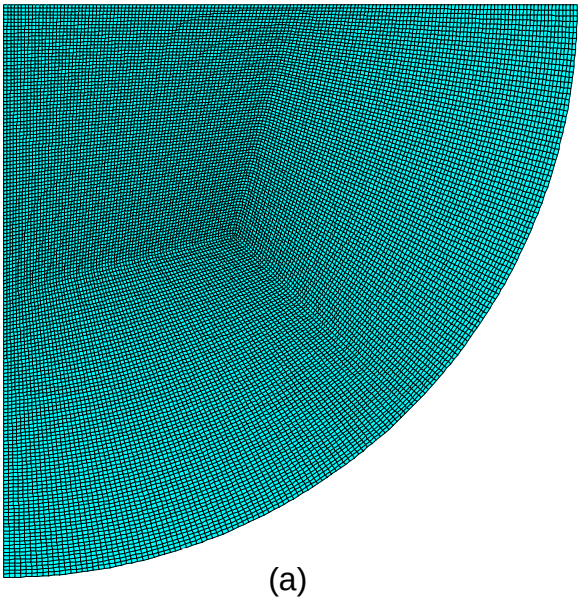

(a)

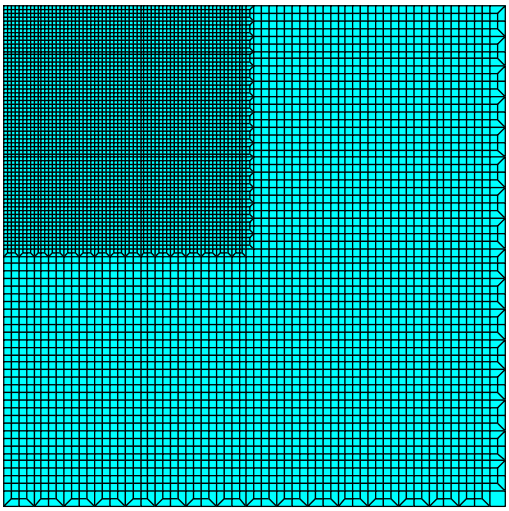

(b)

Figure 4.8. Specimen sub-indenter region discretization: (a) radial mesh typology, (b) rectangular mesh typology with transitions mapped quadrilateral meshes.

Fig. 4.7 shows an example with a detail of the contact region of the global mesh used to investigate the indentation process of targets by

compliant indenters.As the indentation response is mainly dominated by the phenomena occurring into the sub-indenter region, the sensitivity analysis was carried out also considering two different mesh typologies, usually adopted for attaining the right balance in terms of computational effort and results accuracy (Fig. 4.8). The first mesh typology is represented by so called radial meshes: as shown by Fig. 4.8a, this mesh typology is characterized by an elements distribution which dimensions are constant within an hemi-spherical core, having usually the same radius of the indenter, while they increase continuously and uniformly in the surrounding annular region. The rectangular meshes represent the second mesh typology and it is characterized by the presence of transitions mapped quadrilateral meshes for reducing the total number of elements (Fig. 4.8b).

The sensitivity analysis, carried out under the assumption of deformable indenter, revealed that elements characteristic size e of 0.0016% of the indenter diameter D in both mesh typologies are needed for obtaining an accurate description of the crater morphologies. The predicted craters profiles corresponding to two different radial meshes having elements characteristic sizes e/D of 0.0016% and 0.001% of the indenter diameter D are reported in Fig. 4.9a for comparison. The results refer to an Hollomon material having a Young's modulus E, a Poisson's ratio ν and yielding onset σ_y of 170 GPa, 0.22 and 600 MPa, respectively. In the present case, the maximum relative difference was found to be about 0.1%. In any case, the relative discrepancies were found to be lower than 0.5% in the range of explored material properties and attain the maximum

value when piling-up phenomena characterize the indentation response of the indented material.

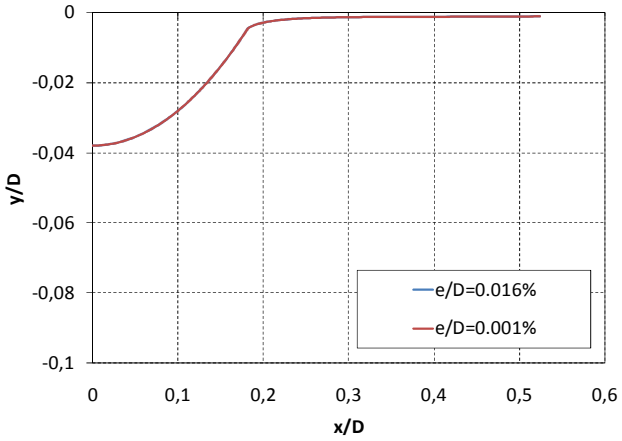

(a)

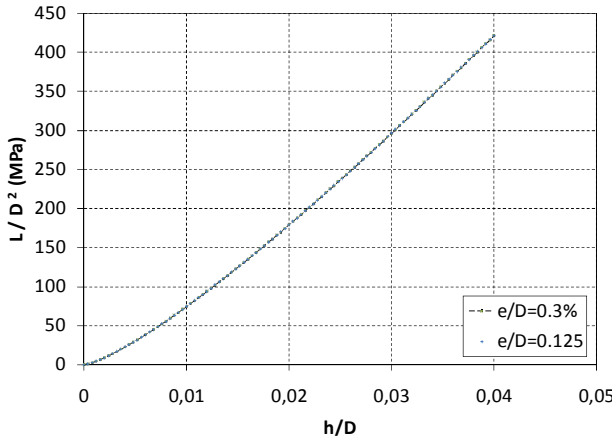

(b)

Figure 4.9. Elements characteristic size effects onto the computational model response: (a) crater profile (normalized indentation depth $h/D = 4\%$) (b) load-indentation depth curve. The model response refers to the frictionless indentation of target obeying to an Hollomon power law characterize by a Young's modulus E, a Poisson's ratio ν and an yielding onset σ_y of 170 GPa, 0.22 and 600 MPa, respectively. Indenter compliance is also taken into account.

With regards to the phenomenological response of indentation tests, i.e. the load-indentation depth curve, the convergence is just achieved at elements characteristic size $e/D = 0.3\%$ (Fig. 4.9b). Similar results were obtained by Lee et al. [55]: according to their results, in fact, mesh-independent estimations of piling-up and sinking-in amounts can be obtained if the characteristic elements size e in the contact region is lower than 0.0125% of the indenter diameter D, whilst characteristic elements sizes e approximately equal 0.125% of the indenter diameter D are sufficient for an accurate determination of the load-indentation depth curve.

4.2.4 Indenter compliance and element technology effects

As regards to the indenter constitutive behaviour, Taljat et al. [65] observed that the indenter compliance does not modify the predicted indentation response if the indenter elastic modulus is at least three time higher than the elastic modulus of the indented material. Indeed, as clearly shown by Fig. 4.10, different indentation responses are induced when rigid or deformable indenter are driven into the material. The reported results refer to two different target materials whose constitutive properties are equivalent to those of an aluminium alloy $(E = 70\ \mathrm{GPa})$ and a steel $(E = 210\ \mathrm{GPa})$. For evaluating the indenter compliance effects, WC-Co ball was considered $(E = 622\ \mathrm{GPa})$. In order to solely distinguish the contribution of the indenter compliance, no friction effects were accounted for and full integration for evaluating the elements stiffness matrix was adopted.

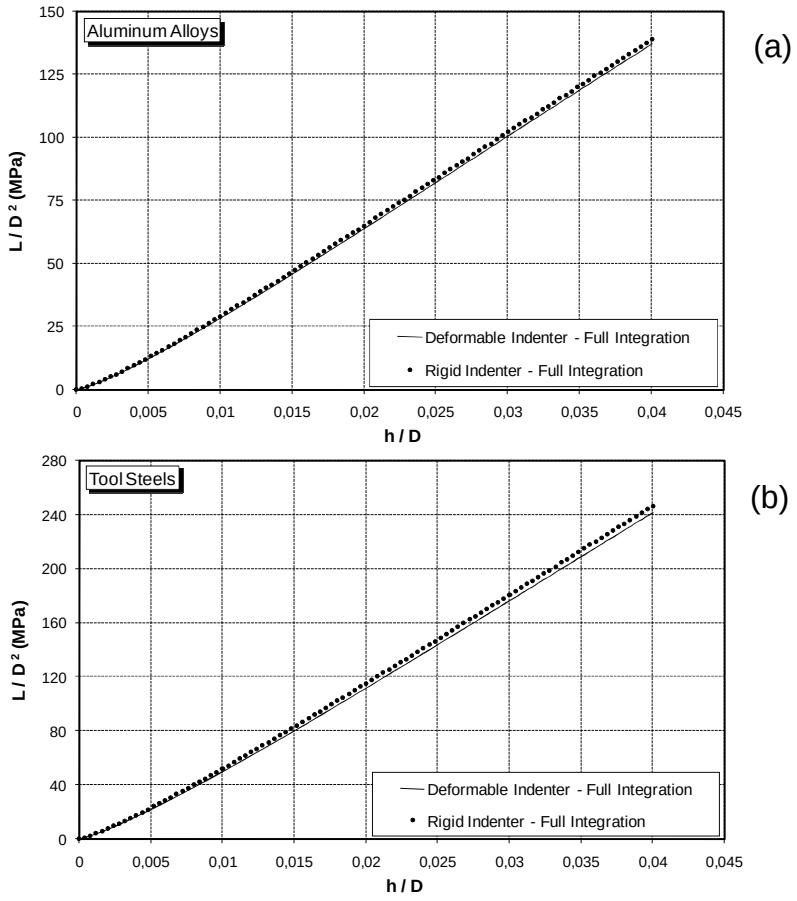

Figure 4.10. Indenter compliance and effects onto the load-indentation depth curve: (a) aluminum alloys having a Young's modulus of 70 GPa and (b) tool steels with a Young's modulus of 210 GPa.

In both cases, neglecting the indenter compliance leads to a systematic overestimate of the applied load L in the characteristic load-indentation depth curves. Such overestimation is significant even though it exists a remarkable difference between the elastic moduli of the indenter and the target and it depends on the

normalized indentation depth h/D: for the aluminum alloys, in fact, the relative difference between the predicted load-indentation depths curve ranges from 1.2% to 9.0%. The greatest relative differences $(> 3\%)$ are especially encountered at low normalized indentation depths $(h/D < 0.008)$. However, the compliance effects cannot be neglected even thought medium-high normalized indentation depths are attained: for normalized indentation depths $h/D > 0.02$, the relative differences are always greater than 1.0%.

Due to the consequences that this assumption can determine in the evaluation of the constitutive properties of ductile materials, when based on the information collected by their characteristic load-indentation depths curves, a systematic analysis of the indenter compliance effects over a wide range of constitutive properties, ranging from light alloys to stainless steels, was performed. The numerical simulations confirmed that ignoring the indenter compliance always determines an overestimation of the load *L* varying between the 5% and 12% with respect to the results obtained by considering the effective indenter compliance. Therefore, it should not be surprising if discrepancies characterize the constitutive properties estimations with respect to the real properties of the indented material, whenever the used evaluation procedure is based on the rigid representation of the spherical indenter.

Although to a lower extent, the rigid indenter assumption also determines modifications in the prediction of the crater profile.

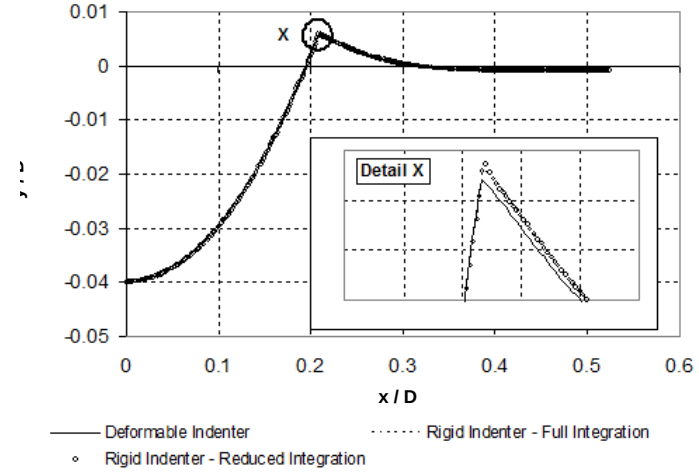

(a)

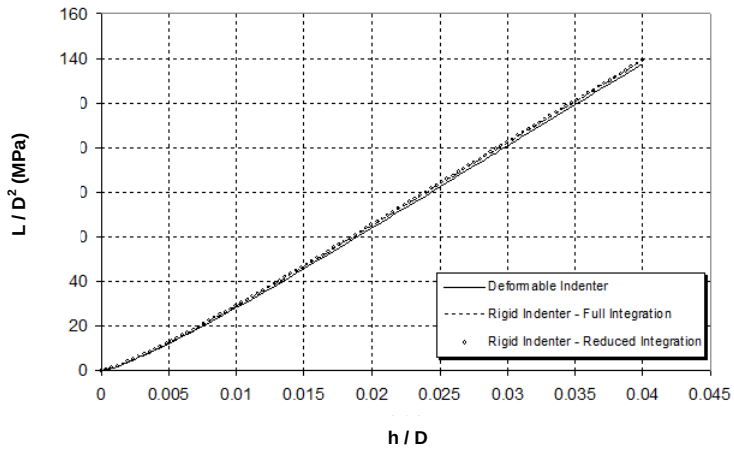

(b)

Figure 4.11. Indenter compliance and element technology effects onto the crater profile (a) and load-indentation depth curve (b) predictions. Reference target: aluminum alloys having a Young's modulus E, a Poisson's ratio ν and an yielding onset σ_y of 70 GPa, 0.3 and 350 MPa, respectively.

These modifications are especially evident at the effective contact radius between the indenter and the indented surface, where the

material piling-up and/or sinking-in phenomena occur (Fig. 4.11a): when the indenter compliance is not accounted for, in fact, larger impressions and higher values of piling-up than those obtained using the deformable indenter are produced. For the examined aluminum alloy, the increment in the piling-un amount is about 4%.For the reference material the effects of the element technology used for evaluating the element contact stiffness are also reported in Fig. 4.11, both for the crater profile prediction and load-indentation-depth curve estimation. By analysing the predicted indentation response, it can be drawn that the evaluation of the elements stiffness matrix barely affects the model response. A trend towards an overestimation of the impression size and load *L* can be recognized when the reduced integration is adopted, but the relative discrepancies with respect to the prediction obtained by using the full integration rule are small, less than 0.8%. Similar results were also found by analysing the typical behaviour of different metallic materials like light alloys (Mg-alloys), Cu-alloys and cast irons, thus confirming that the methods for formulating the elements stiffness matrix is independent on the constitutive properties of the indented bulk.

4.3 Integration of the Experimental and Numerical Methods

4.3.1 Basic issues of the integration

It is obvious that the interpretation of any experimental phenomena via numerical modeling cannot leave out of consideration the

validation of the used computational model. However, in the case of the simulation of indentation processes, a computational model can be considered validated only once the agreement between the predicted and experimental residual impressions and also between the numerical and experimental load-indentation depth curves are probed. As shown by Chen et al. [29], these agreements are mandatory to conclude that the predicted straining processes promoted by the indenter into the sub-indenter region are identical to those occurring during the experimental test.

However, it should be noted that the computational models, described in the previous sections, is not able to account for the real compliance of the testing machine. Model validation without a previous testing machine calibration lacks consequently of meaning. In other terms, for integrating the numerical and experimental approaches, the knowledge of the constitutive behaviors and the indentation responses of two different real materials, from now on denominated reference materials, is necessary: it is obvious, in fact, that calibration and validation cannot be carried out using the information coming from the same material.

However, it should be remembered that the computational model is based on two very important hypotheses referring to the material homogeneity and isotropy. Therefore, to calibrate the testing machine and validate the computational model, the selection of the reference materials should be carried out among the most common metallic materials satisfying these two requirements as truly as possible. The selection must be also performed among metallic materials having different constitutive behaviours so that the validity

of the integration procedure can be ensured over a wide range of materials properties.

For ensuring the widest validity of the integration procedure, it was decided to select the reference materials among the most common aluminum alloys and steels. Although this choice may appear merely arbitrary, there are no doubts that these two classes of materials are the most popular alloys used for engineering applications, and, depending on the used manufacturing processes, can satisfy the above mentioned requirements. To this purpose a wide experimental campaign was carried out and it was found that goods levels of material homogeneity and isotropy are achieved by Al 6082-T6 alloy rolled plates and by AISI H13 steel plates obtained via multidirectional forging and subsequently annealed at temperatures near to the solidus temperature. Being these two alloys very popular and manufactured via traditional industrial processes, they were selected as reference materials for calibrating the testing machine and validating the numerical model.

4.3.2 Experimental constitutive behaviours of the reference materials.

The determination of the constitutive behaviour of each material was carried out by standard tensile tests [86]. The experimental tests were conducted on an universal servo-hydraulic testing machine (INSTRON 8516). Being both materials produced via forming processes and available in the form of plates, the degree of isotropy of each material was checked by manufacturing an adequate number

of specimens along the Longitudinal directions (L-specimen) and along the Transversal direction (T-specimen). Specimens were manufactured from 1000x1000x12 mm plates.

Fig. 4.12 shows for both tested materials the Upper (UB) and Lower (LB) bounds of the true stress-true strain curves $(\sigma_t - \varepsilon_t)$ sheaf obtained by elaborating the standard tensile tests both for the L- and T-specimens, whereas the characteristic tensile properties are summarized in Tab. 4.II for comparison. Homogeneity and isotropy can be easily recognized in both materials. After elaborating the experimental data, it was found that the relative differences between the Young's modulus, the yielding stress and the ultimate stress corresponding to the L and T direction are lower than 8.0% and 2.0%, for the tested materials, thus confirming that the level of anisotropy is sufficiently low in both cases, especially for AISI H13 alloy. With regard to the material homogeneity, it can be appreciated if the narrow band delineated by the upper and lower bounds is considered.

Table 4.II. Experimental tensile properties of tested materials.

	Al6082-T6		**AISI H13**	
Material Properties	L-Direction	T-Direction	L-Direction	T-Direction
Young's modulus E (GPa)	69±1	65±2	196±0.5	195±0.7
Yielding stress σ_{yp} (MPa)	331±2	315±2	393±2	388±2
Ultimate stress σ_u (MPa)	354±2	333±4	753±4	743±4
Elongation at rupture ε_u (%)	7.1±0.6	7.7±0.9	15.3±0.6	17.2±0.7

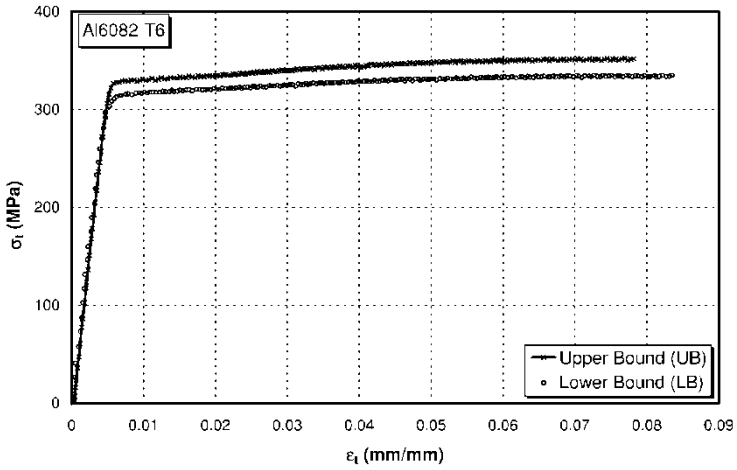

(a)

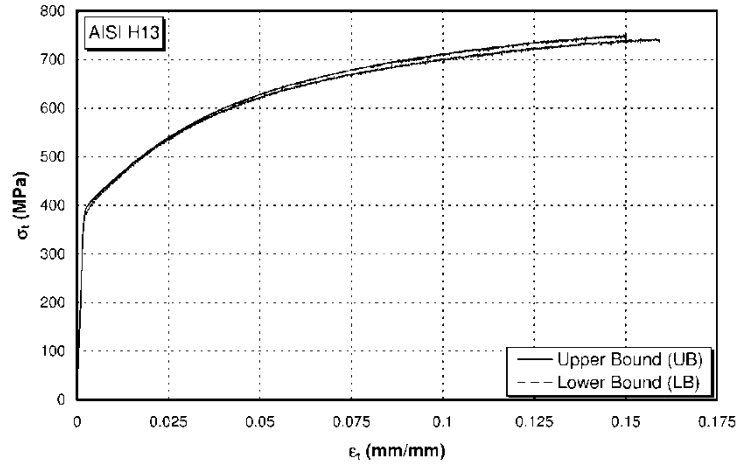

(b)

Figure 4.12. Experimental true stress-true strain curves of the two reference materials: (a) Al 6082-T2 alloy, (b) AISI H13 alloy.

As expected, both materials are characterized by a different constitutive behaviour especially with regard to the strain-hardening behaviour. Although it was found that the Hollomon's model can be solely used for a rough representation of both true stress-true strain

curves, the strain-hardening coefficient n, estimated adopting this constitutive framework resulted in 0.2 for the tool steel and 0.08 for the aluminum alloy. For the above mentioned evidences, these two materials were judged as the most appropriate candidate materials for calibrating and validating the computational model.

4.3.3 Experimental indentation response of the reference materials

With regard to the evaluation of the indentation response of the reference materials, the characteristic load-indentation depth curves were experimentally determined by the *Diaptometro*. The ASTM E10 prescriptions [8] for evaluating the Brinell hardness of metallic materials were adopted. To this purpose, 25x25x12 mm polished targets were manufactured from the same plates used for determining the true stress-true strain curves of each reference material. Tests were carried out in displacement control and the load-indentation depth curves were measured with a resolution of 1 N and 0.4 μm on the load *L* and penetration *h*, respectively. In both cases a maximum normalized depth $h/D = 0.04$ was attained, corresponding to maximum indentation loads *L* of 860 N and 1500 N for Al6082-T6 and AISI H13 alloys, respectively. Finally, experimental indentation tests were performed using a Tungsten Carbide (WC-Co) spherical indenter having a diameter $D = 2.5$ mm. Moreover, a WC-Co spherical indenter having a diameter $D = 5$ mm was also used for estimating potential microstructure effects onto the indentation response, but in both cases no appreciable modifications of the load-indentation depth curves were found, thus confirming that the chosen

diameter $D = 2.5$ mm and the penetration depths reached during the tests are able to capture the overall response of the two reference materials.

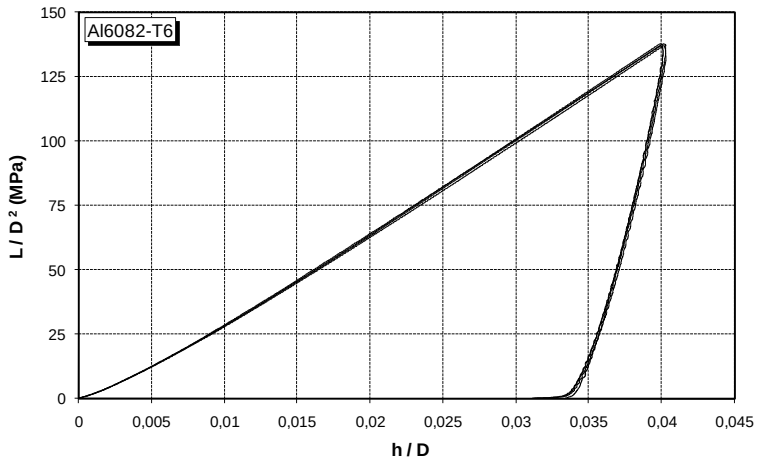

(a)

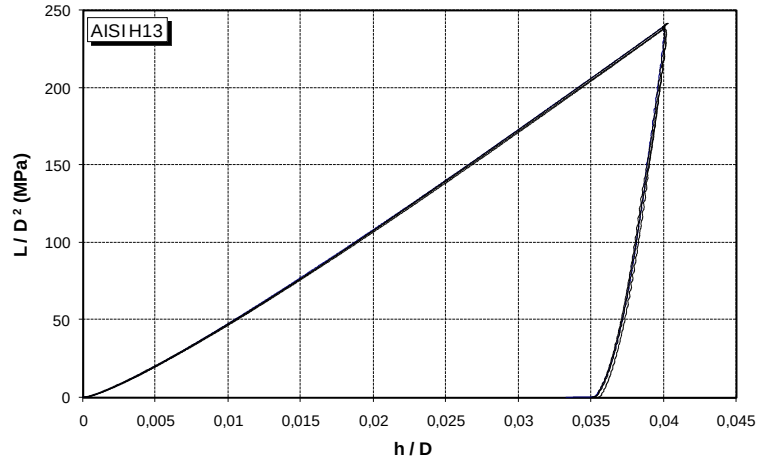

(b)

Figure 4.13. Experimental *L-h* curves corresponding to four indentations performed on each tested materials: (a) Al6082-T6 alloy, (b) AISI H13 alloy.

Fig. 4.13 illustrates the experimental load-indentation depth curves obtained by Al6082-T6 and AISI H13 alloys. Both diagrams report the

load-indentation curves corresponding to four indentation tests, performed onto different targets. The very high repeatability of the experimental results confirms that both materials are characterized by an high degree of isotropy. The maximum relative differences in terms of load were found to be lower than 1%, for both materials.

4.3.4 Residual crater profile analysis

As mentioned in the previous section, the computational model validation must be also carried out by comparing the numerically predicted residual crater profile and with the experimental impressions left by the indenter. To this purpose, the experimental residual crater profile at the end of each indentation tests was measured according to a procedure specifically developed.

To measure the residual impressions, contacting profilometers were preferred to non-contacting profilometers: the latter class of instruments, in fact, were found to be unable to accurately measure the residual impressions geometries. It was especially found the measurement fails when the instrument try to capture the cavity portion characterized by steep gradients: different non-contacting profilometers were used but the inner regions of the cavity near to the crater rims resulted always undetectable. Therefore, in the present investigation the determination of the residual impressions geometries was carried using a contact stylus profilometer (Talyscan 150, Taylor Hobson, UK) having a measurement range and in-depth resolution of 370 μm and 660 nm, respectively.

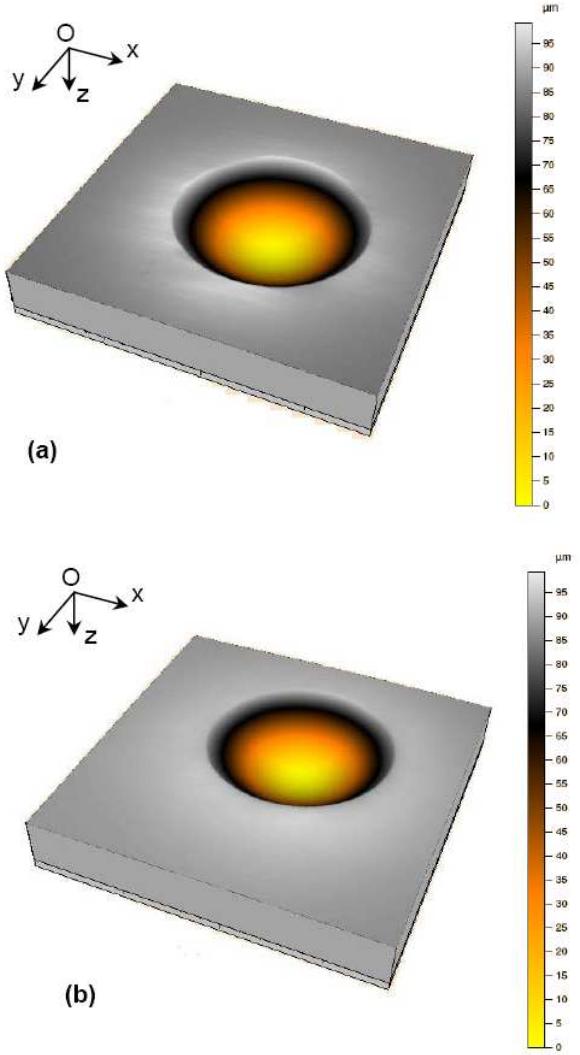

Figure 4.14. Figure 3. Experimental 3D residual crater profiles for one of the four indentations performed on the tested materials. (a) Al6082-T6 alloy, (b) AISI H13 alloy.

Each impression was determined by scanning a square region around the crater which sides have been chosen far enough from the impression, thus including the overall region interested by the straining processes promoted by the indenter. Scansion region size

was iteratively determined by analysing the peripheral regions profiles: the final size was established once no appreciable modifications in the surface profile trend were observed. Crater shape acquisition was carried out through a multiple indented surface scansion with a step of 1 μm along the *y* direction and a spatial resolution of 0.5 μm along *x* direction.

An example of a 3D reconstruction of the experimental residual craters profiles corresponding to the indentation tests conditions described in the previous section are reported in Fig. 4.14 for both materials. In the reconstruction misalignments were compensated by enforcing rigid roto-translations to the set of the experimental data around the x and y axes and along by z axis. The corresponding angles and translational vector were evaluated via least square method applied to the z coordinates of the most peripheral points.

In order to compare the experimental residual profiles with those numerically predicted, the experimental data were further processed for obtaining the Upper (UB) and Lower (LB) Bounds within which the residual crater profiles may vary (Fig. 4.15). Here, the UB and LB represent the crater profile sections lying in the $\{O, x, z\}$ and $\{O, y, z\}$ planes characterized by the maximum and minimum residual crater depths, respectively, among all the performed measurements.

The narrow bands delineated by the UB and LB, within which the residual crater profile may vary, confirms for both materials the high degree of homogeneity and isotropy, especially for AISI H13 alloy. By contrast, an appreciable scatter characterizes the residual piling-up amount around the impression for Al6082-T6 alloy. A possible

explanation of this evidence can be provided by analysing the 3D reconstruction shown in Fig. 4.14a.

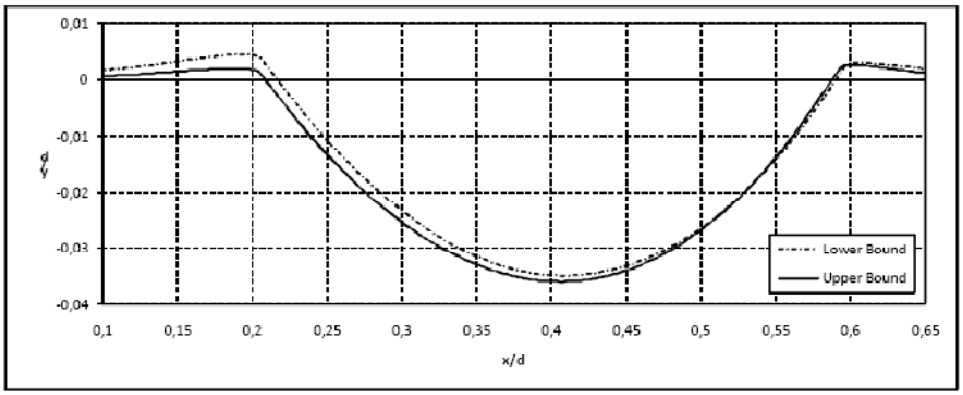

(a)

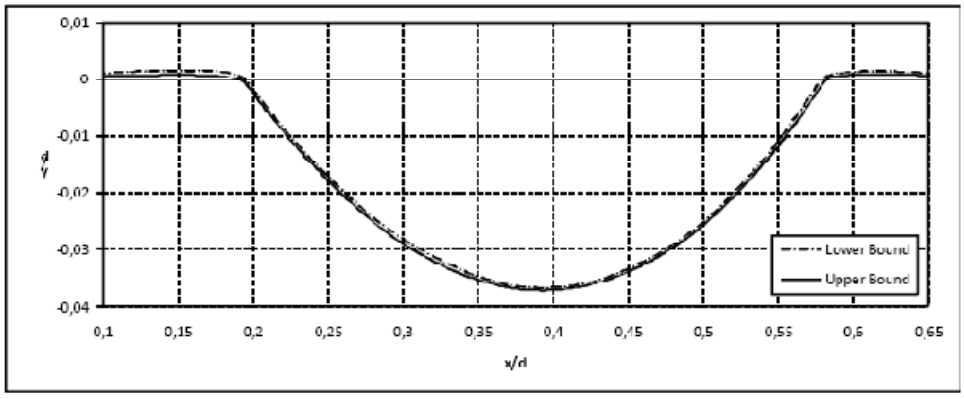

(b)

Fig. 4.15. Experimental Upper and Lower Bounds of the residual craters profiles for (a) Al 6082-T6 alloy and (b) AISI H13 alloy.

A detailed analysis of the crater rim allowed to recognize that the amount of material piling-up around the impression seems to be depend on the direction. Two orthogonal directions, along which the piling-up amount takes the maximum values, can be especially

detected, thus inducing to consider that even small levels of anisotropy may affect the piling-up or sink-in material behaviour.
This evidence was also confirmed by analysing the experimental data corresponding to the residual impressions for all indentation tests performed onto the aluminum alloy. Consequently, the material characterization procedures based on the numerical correlations between the crater geometry and the constitutive properties seem to be crucial: obtaining an accurate measurement of the crater profile appears to be very difficult, thus making it impossible to validate any numerical predictions regarding the impression left by the indenter.

4.3.5 Testing machine calibration

As regards to the testing machine calibration, the experimental and numerical results provided by the experimental characterization and numerical modelling for AISI H13 steel were used for determining the calibration curve. The calibration curve were determined by comparing the experimental and numerical *L*-*h* curves. The selection of AISI H13 steel as the reference material for the testing machine calibration was motivated by the fact that high levels of homogeneity and isotropy were experimentally found for this alloy: the estimation of the calibration curve, in fact, must not be dependent on the constitutive law implemented in the computation model for determining the corresponding *L*-*h* curve. In other terms, adopting this material for the determination of the calibration curve does not introduce any source of uncertainness in the evaluation of the

calibration curve. As clearly shown by Fig. 4.16, no appreciable differences characterize the predicted *L-h* curves when the upper and lower bounds of the true stress-true strain experimental curves sheaf for this material are used in the FE model. In this case, the maximum relative difference between the two *L-h* curves was found to be less than 0.2%. Therefore, the choice of the constitutive law used to generate the corresponding *L-h* curve does not affect the estimation of the calibration curve if this material is adopted as reference material.

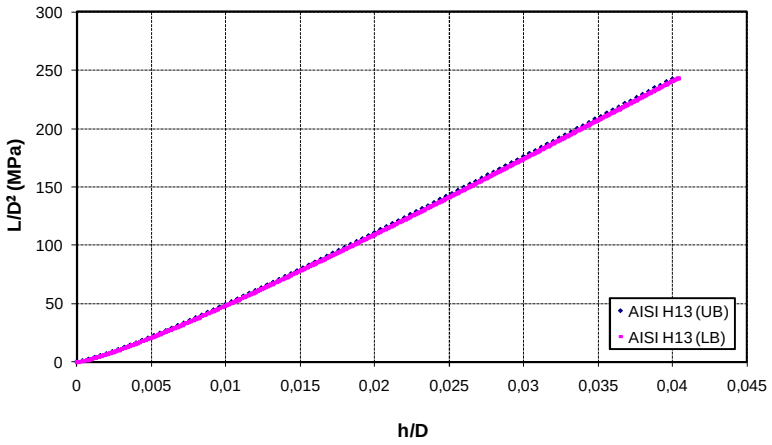

Figure 4.16. *L-h* curves for AISI H13 steel corresponding to the upper and lower true stress-true strain curves. The results refer to frictionless indenter having a diameter $D = 2.5$ mm.

Although the results refer to a frictionless indentation process and the maximum normalized penetration depths h/D was fixed at 0.04, neglecting the frictional effects and limiting the penetration depths at $0.04D$ should not to be viewed as limits for the evaluation of the calibration curve. There is at first a wide agreement about the

negligible effects of friction onto the trend of *L*-*h* curves at these levels of indent depth and, as will be shown in the next chapter, this evidence was also found in the present investigation. Secondly, both the analytical and numerical models confirm that plastic strains ε_p values up to 20% are induced by the spherical indenter when it reaches these degrees of penetration into the target. Therefore, such indentation depths can be used for inferring at least the first part of the true stress-true strain curves which is surely the most important portion from the engineering point of view: material yielding stress and the strain-hardening capabilities are, in fact, contained in this range of plastic strains.

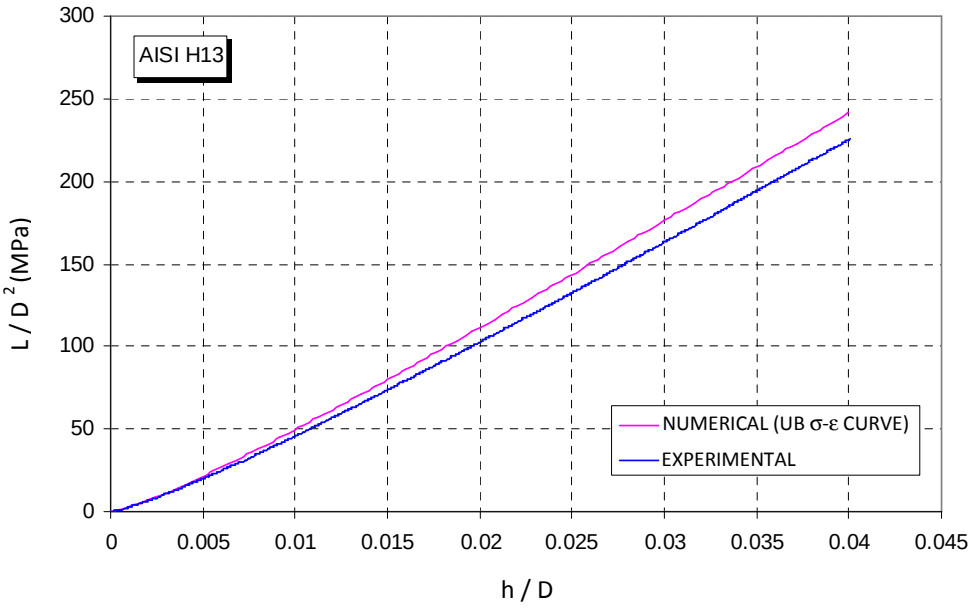

Figure 4.17. The experimental and numerical *L*-*h* curves for AISI H13 steel. The numerical *L*-*h* curve is obtained by using the UB curve of the true stress-true strain experimental curve sheaf and by neglecting the frictional effects.

The experimental and numerical *L*-*h* curves for the AISI H13 steel are plotted in Fig. 4.17. As expected, the computational model predicts a stiffer behaviour with respect to what is experimentally observed: the FE model, in fact, does not take into account the real testing machine compliance. However, by analysing the gap between the two curves, the amount of correction appears very limited: at the maximum applied load the difference between the experimental and predicted indentation depths is about 4 μm, thus representing the 4% of the maximum indentation depth $(h = 100\ \mu m)$ achieved during the test. This satisfactory result must be related to the very good design of the *Diaptometro* and the excellent computational model developed for simulating the indentation processes.

With regard to the correction of the experimental data, the calibration procedure proposed by Beghini et al. [87] was adopted. However, instead of using the interpolation function proposed by the authors (see eqn. (3.39)) for correlating the load *L* to the indentation depth *h* in both curves, the following relationship

$$\frac{L}{ED^2} = \sum_{k=1}^{4} A_k \left(\frac{h}{D}\right)^{c_k} \qquad (4.1)$$

between the two variables was used. Here, A_k and c_k are fitting parameter depending on the material properties. As will be proofed in Chapter 6, this new interpolation function ensures a better representation of the experimental and numerical *L*-*h* curves. Following the calibration procedure developed by Beghini et al. [87], the estimation of the calibration curve was then carried out by

subtracting the experimental *L*-*h* curve to the numerical one over the range of the considered loads.

4.3.6 Computational model validation

Being the computational model mainly aimed at interpreting the experimental indentation response of metallic materials, its validation was carried out by comparing the numerical and experimental results concerning the main features characterizing the indentation response, i.e. the characteristic *L*-*h* curve and the residual crater profile. As anticipated, the experimental indentation response of Al 6082-T6 alloy was used as the first comparison term. Unlike AISI H13 steel, the experimental characterization of Al 6082-T6 alloy revealed that a low but appreciable gap characterizes the upper and lower bounds of true stress-true strain experimental curve sheaf. Consequently, it should not be surprising if differences in the indentation response are found when the true stress-true strain curves representing the upper and lower bounds of the experimental curves sheaf are used as input in the computational model. Being impossible to uniquely define an *average* true stress-true strain curve for Al 6082-T6 alloy, to check the accuracy and reliability of the FE model, it was decided to carried out the FE model validation using as input in the FE model the constitutive curve yielding the maximum differences between numerical predictions and the experimental findings.

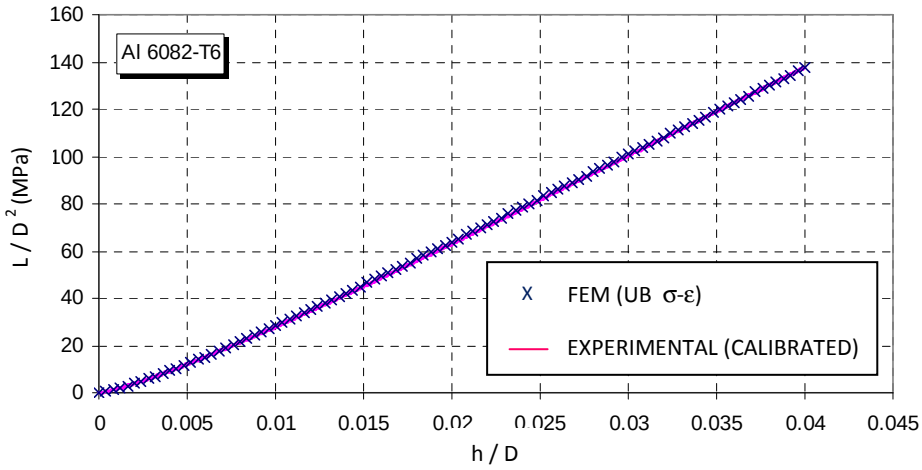

(a)

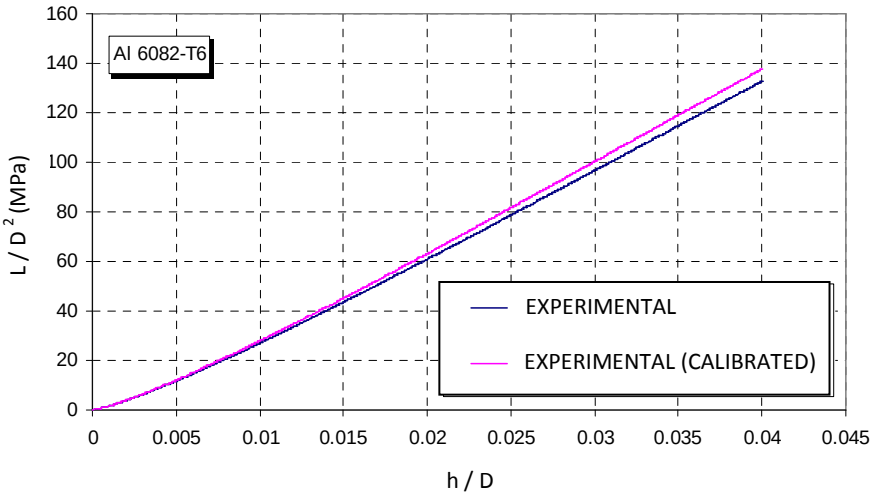

(b)

Figure 4.18. Computational model validation: (a) comparison between the experimental and numerical *L*-*h* curves for Al 6082-T6 alloy and (b) experimental *L*-*h* curves for Al 6082-T6 alloy before and after calibration. The numerical *L*-*h* curve is obtained by using the UB curve of the true stress-true strain experimental curve sheaf and by neglecting the frictional effects.

For the Al 6082-T6 alloy such condition was obtained by implementing into the FE model as true stress-true strain curve the upper bound of the true stress-true strain experimental curves sheaf and the comparison between the corresponding numerical *L*-*h* curve with the experimental one after calibrating the experimental measurements are plotted in Fig. 4.18a.The effects of the calibration onto the experimental data are also reported (Fig. 4.18b).

As shown by Fig. 4.18a, it exists a very good agreement between the experimental measurements and the numerical results for the second reference material. Data processing revealed that the relative differences between the two curves are always lower than 0.5%.

Similar results were found when the numerically predicted craters profiles were compared to those obtained by the experimental campaign for both the reference materials (Fig. 4.19). Except for the predictions of the piling-up amounts, relative scatters were found to be less than 2%. With regard to the estimation of the material piling-up amount, the poor agreements obtained in both cases, especially for Al 6082-T6 alloy, should not be surprising: the numerical results, in fact, are based on two important assumptions concerning the material isotropy and the absence of friction between the contacting bodies. It is reasonable to think that these two assumptions, especially the latter, are not fully satisfied during the experimental tests.

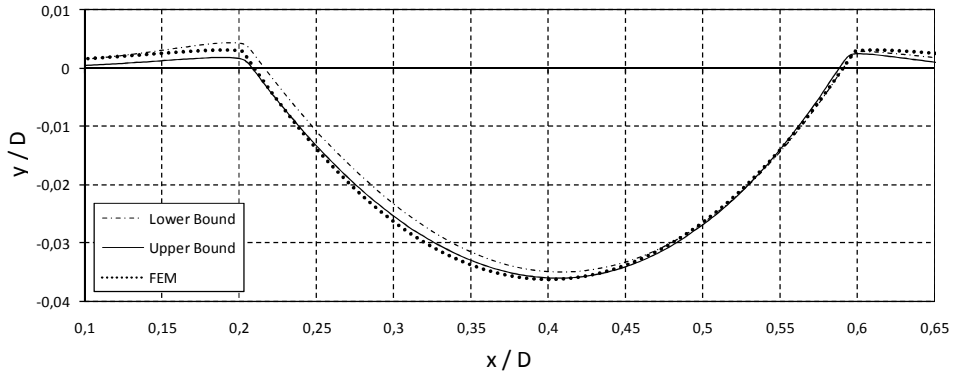

(a)

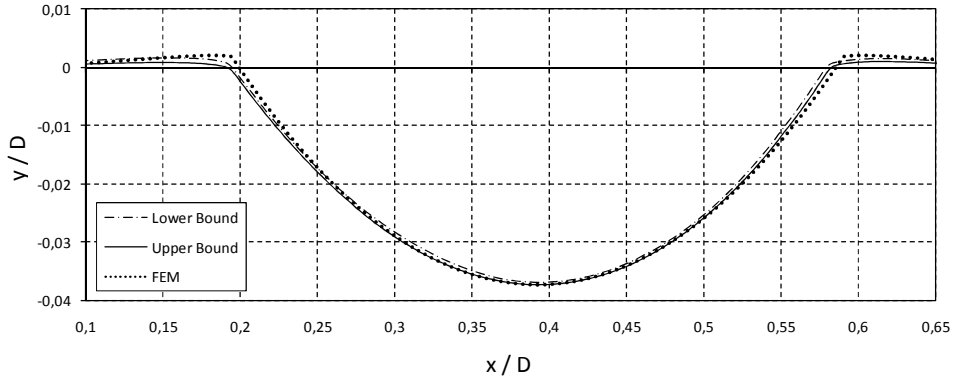

(b)

Fig. 4.19. Computational model validation: comparison between the experimental Upper and Lower Bounds of the residual craters profiles and the corresponding numerical predictions for (a) Al 6082-T6 alloy and (b) AISI H13 steel.

4.4 Summary

There are no doubts that for interpreting the experimental indentation response, i.e. the characteristic L-h curve and the crater profile evolution, the knowledge of the straining phenomena occurring in the sub-indenter region is mandatory, especially if the indentation response is used to deduce the constitutive properties of the

indented material. Unfortunately analytical or numerical approaches and experimental campaigns, even though properly designed, are not able to achieve this purpose, if they are not properly integrated.

The present chapter showed how it is possible to obtain a new integrated numerical-experimental tool for investigating the straining processes which are at the base of the materials indentation response, once a testing machine and a computational model are properly defined and interrelated. Therefore, the new testing machine and computational model specifically developed to explore the indentation response of metallic materials were presented and the most crucial issues concerning the design and development of these two tools illustrated. A special emphasis was dedicated to show how these two different tools can be integrated, once the experimental indentation response of two reference materials is established.

From the point of view of the design of the testing machine, it was found that an appropriate design of the indentation system of the testing machine is mandatory to minimize the testing machine compliance and consequently the amount of correction of the experimental data. As regards to the computational modelling, mesh density and typology as well as the adopted element technology may play a very important role in the definition of the model response, is not adequately set-up. On the contrary, the indenter compliance is a key factor and ignoring the deformable behaviour of the indenter leads to predict a different material indentation response, thus undermining the reliability and accuracy of those methodologies aimed at the estimation of the constitutive properties of the indented material.

CHAPTER 5
Numerical analysis of plastic deformation process in spherical indentation

The knowledge of the straining phenomena induced by a spherical indenter as a function of the indentation depth is of paramount importance for establishing if the experimental indentation response is effectively representative of the indented material, from one side, and distinguishing, from the other side, the most reliable experimental source of information from which the constitutive behavior of the indented material can be deduced. Moreover, it allows to estimate the effects of those experimental parameters which take part in the test, as friction between the indenter and the target surface. From these points of view, the reviewed indentation theories only provide a general description of the deformation mechanisms activated by the indenter into the target. Also, ideal constitutive behaviours are always at the base of the description of straining phenomena. Finally, the friction conditions are only taken into account from a phenomenological point of view.

To establish a direct correlation between the materials indentation response and the constitutive behaviour, the present chapter[1] is aimed at describing the evolution of the plastic strain distribution during the indentation test in real materials. To this purpose, the analysis of the deformation processes was focused onto Al 6082-T6 alloy and AISI H13 steel, being known their constitutive behaviours from the experimental characterization. The plastic strains distribution and the volume of the material plastically strained were determined by using the computation model presented in the previous chapter. Since the loading cycle of the indentation test represents the source of information from which the plastic properties can be deduced, the investigation was restricted only onto this phase of the indentation process. All the features characterizing the indentation response were examined: plastic flow diffusion in the sub-indenter region, crater profile evolution and the characteristic load-indentation depth curve. Among the experimental parameters, which can affect the material indentation response, friction coefficient is undoubtedly the most important: it is known very well that it modifies the plastic strains distribution significantly. It is also a parameter which value cannot be established during the test and can undergo potential variations. Therefore, the determination of the frictional effects onto the plastic strain and crater profile evolutions, from one side, and onto the load-indentation depth curve, from the other side, were included in the investigation.

[1] The present results are partially published in J. Mater. Res. Vol. 24, pp. 1270-1278 (2009) [60].

5.1 Plastic strains field evolution into the sub-indenter region

5.1.1 Plastic strains field evolution promoted by frictionless indenter

The evolutions of the plastic strains distribution during a frictionless indentation test for Al 6082-T6 alloy and AISI H13 steel are plotted in Figs. 5.1 and 5.2. For both materials, the results were obtained by implementing in the computational model the upper bounds curves of the true stress-true strain experimental curves sheaf. The contours plots refer to the distribution of the accumulated equivalent plastic strain ε_{eqv} at the most interesting stages of the loading cycle. Maximum indentation depth $(h/D)_{max}$ and the indenter diameter D were chosen in order to reproduce the effective experimental conditions. Accordingly, $(h/D)_{max}$ was set at 0.04 in both cases, whereas the indenter diameter D was fixed at 2.5 mm.

A preliminary analysis of the maps sequence reveals that the elastic-plastic indentation regime drives the response of both materials. During the entire loading cycle an hemispherical shape can be recognized for the plastic core and the accumulated equivalent plastic strain gradient is fairly gradual and it is akin to that produced by an expanding spherical cavity into a infinite medium, as predicted by Johnson [44]. The interaction between the plastic core and the surrounding elastic medium is apparent and it allows to establish the phases of the loading cycle which correspond material sinking-in and piling-up.

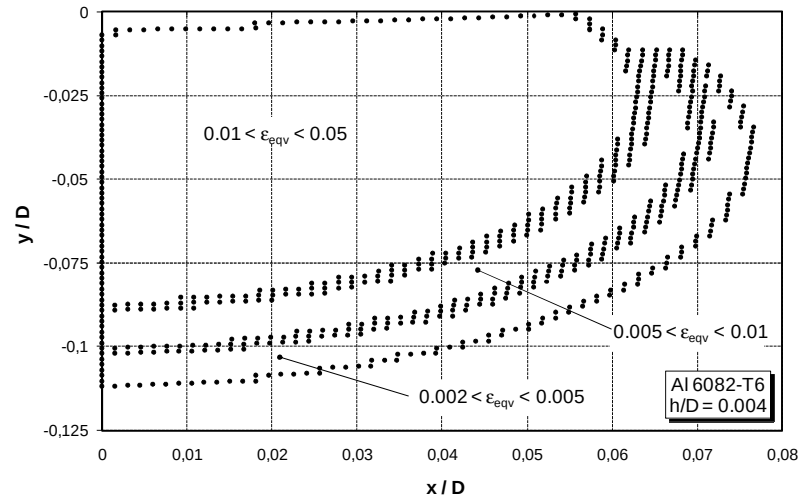

(a)

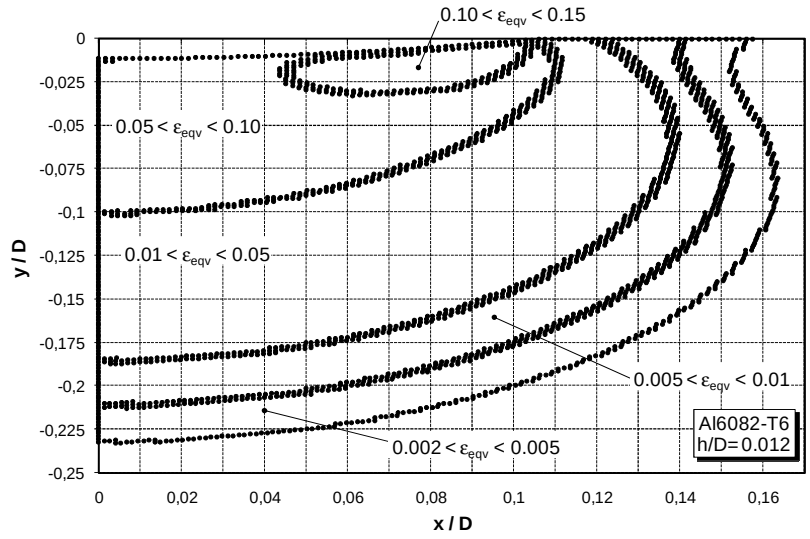

(b)

Figure 5.1. Accumulated equivalent plastic strain ε_{eqv} field at different normalized indentation depths h/D induced by frictionless indenters in Al 6082-T6 alloy: (a) $h/D = 0.004$, (b) $h/D = 0.012$, (c) $h/D = 0.02$ and (d) $h/D = 0.04$.

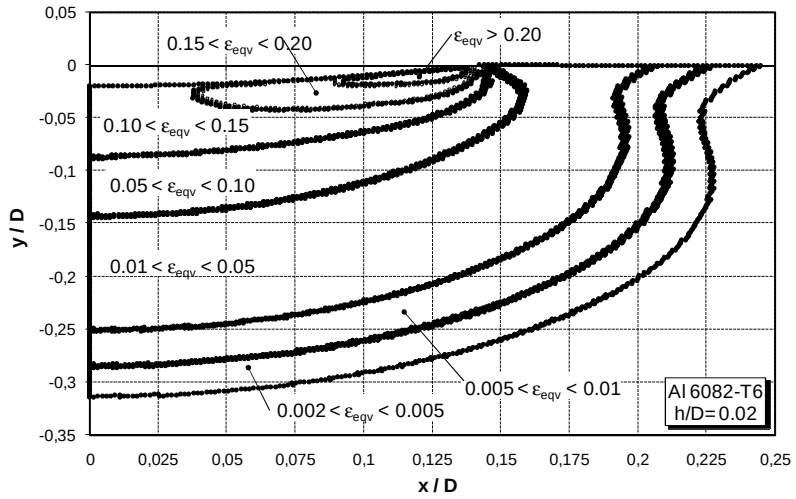

(c)

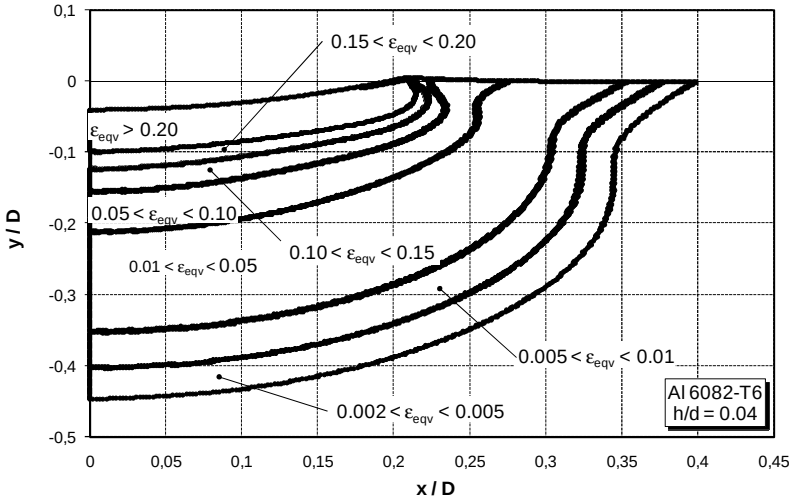

(d)

Figure 5.1 (Continued).

For Al 6082-T6 alloy the plastic deformation process is still active at very low normalized indentation depths ($h/D < 0.004$). A significant plastic core beneath the indenter, in fact, can be clearly observed at $h/D = 0.004$ (Fig. 5.1a). It is interesting to note that, even if the indentation depth h takes very low values, plastic strains ranging from 1% to 5% are promoted in a appreciable volume in the sub-indenter region (Fig. 5.1a). Approximating the volume plastically strained with an hemisphere, the plastic strains spread till a radius of $0.1D$, approximately. Small increments of the penetration depth ($0.004 \leq h/D < 0.012$) promotes both an increase of the plastic volume (Fig. 5.1b), especially along the indentation axis, and an increment of the plastic strains values. A value of $0.2D$ can be regarded as a first estimation of the radius of the plastic core at these stages of the indentation process, whilst plastic strains varying between 5% to 10% are shared out in a hemispherical volume having a radius of $0.1D$, approximately.

At deeper penetration depths ($0.02 \leq h/D < 0.04$), a remarkable increase of the volume plastically strained is especially observed both along the indentation axis (Fig. 5.1c) and along the radial direction (Fig. 5.1d), thus confirming that material piling-up is occurring at the indenter contact edge. According to the numerical results, plastic strains spread till a radial distance of $0.4D$, approximately, once the maximum indentation load ($h/D = 0.04$) is achieved (Fig. 5.1d). Conversely, corresponding increments in the plastic strain are not detected. Plastic strains greater than 105 are confined in a small core having a radius equal to $0.1D$, approximately.

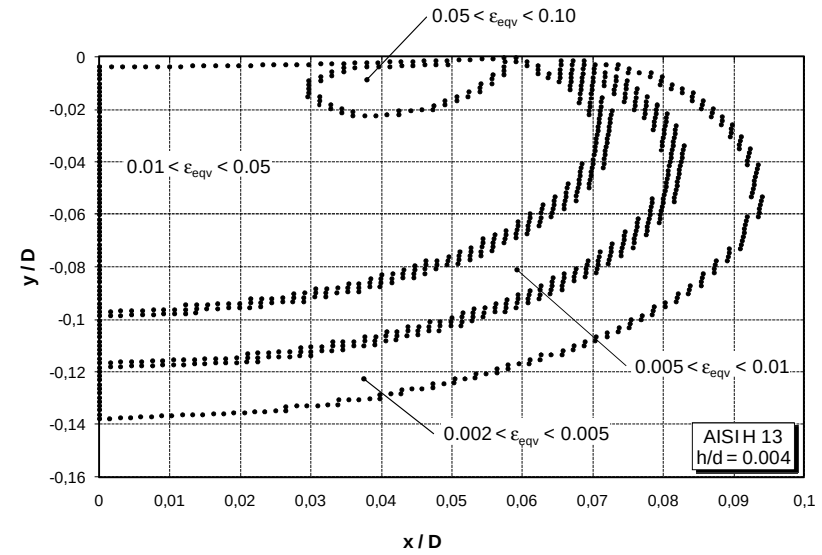

(a)

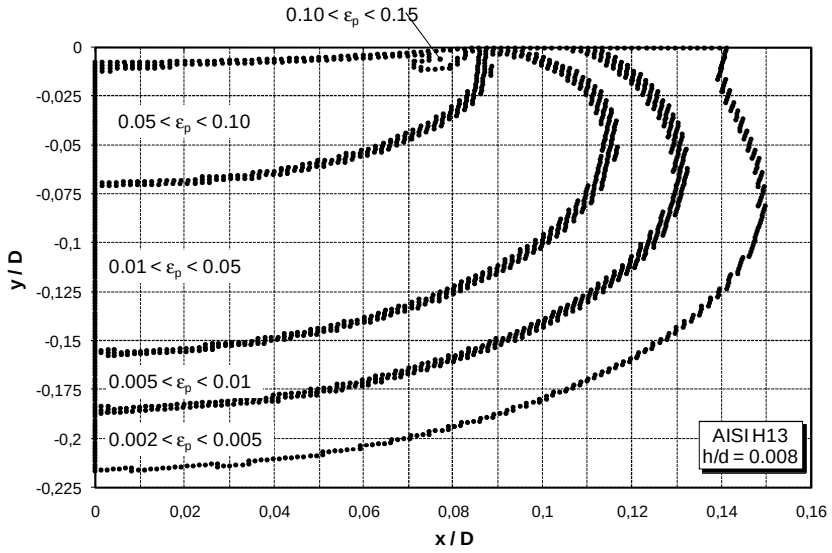

(b)

Figure 5.2. Accumulated equivalent plastic strain ε_{eqv} field at different normalized indentation depths h/D induced by frictionless indenters in AISI H13 steel: (a) $h/D = 0.004$, (b) $h/D = 0.008$, (c) $h/D = 0.02$ and (d) $h/D = 0.04$.

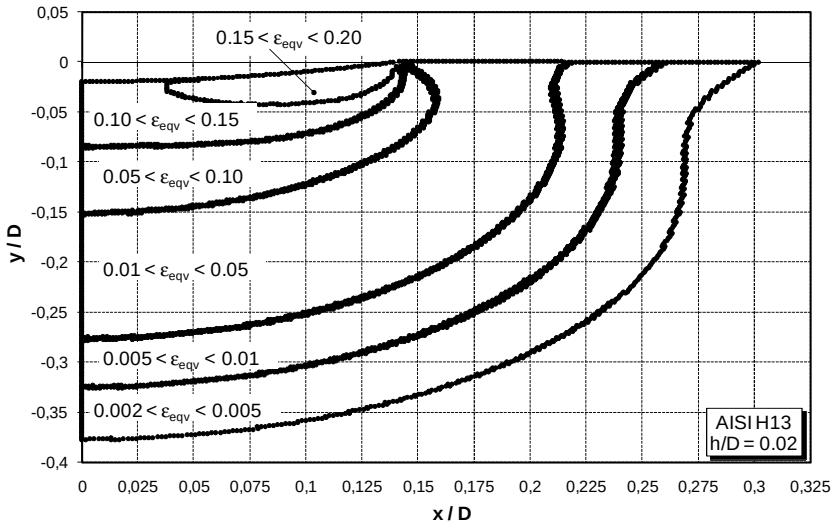

(c)

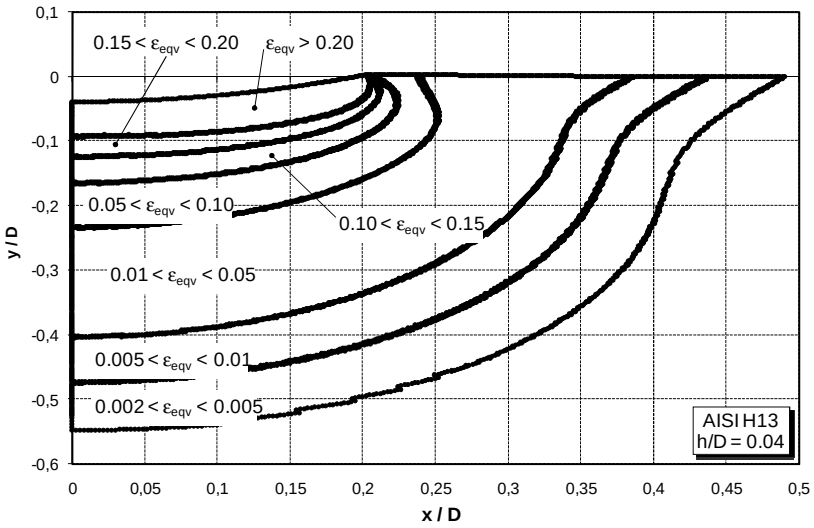

(d)

Figure 5.2. (Continued).

As regards to the response of AISI H13 steel, the evolution of the plastic strains field is akin to that observed in Al 6082-T6 alloy. The main differences between the response of two materials concern the plastic core size. For AISI H13 steel an appreciable increment of the plastic volume with respect to Al 6082-T6 alloy can be easily recognized at all stages of the indentation process. By comparing the evolution of the plastic strains (Fig. 5.2) with that corresponding to Al 6082-T6, it can be deduced that the radius, separating the plastic core from the surrounding elastic medium, increases of 20%, approximately. In this case too, large penetrations depths do not promote plastic strain increments equivalent to the increments of the plastic volume in the sub-indenter region. However, it should be noted that, for frictionless indentation, an adequate material volume is strained in a real material at these degrees of penetration depth. Therefore, the material indentation response can be surely considered as representative of the indented material.

From the point of view of the material properties estimation, it is easy to establish the direct correspondence between the stress-strain curve and the indentation depth, if the local plastic strain in a reference point is monitored. Conversely, if the estimation is based onto the analysis of the characteristic *L-h* curve, in consideration of the fact that it represents an averaged material response, it must be concluded that the indentation response corresponding to these stages of the indentation process must be correlated to the first portion of the stress-plastic strain curve of the indented material.

5.1.2 Frictional effects onto the plastic deformation process

Mesarovic and Fleck, Lee et al. and Taljat et al. [54,55,65] observed that friction significantly affects the plastic strains distribution in the sub-indenter region during the indentation process. Friction was especially found to be responsible of a radial constraint effect [54]. From a phenomenological point of view, friction simultaneously promotes yielding processes in the region beneath the indenter and prevents the lateral spreading of the plastic flow. The final result consists in remarkable reductions of material piling-up amounts and larger plastic strains, as compared to those induced by frictionless indenters, along the indentation axis. According to Mesarovic and Fleck [54], these effects must be related to the tri-axial stress states promoted by the contact conditions in the region around the indenter contact edge.

A similar scenario is found in the straining responses of Al 6082-T6 alloy and AISI H13 steel when friction between the indenter and target is taken into account. Figs. 5.3 and 5.4 show the evolution of the accumulated equivalent plastic strain ε_{eqv} in Al 6082-T6 alloy and AISI H13 steel, respectively, for a friction coefficient $\mu = 0.5$. In this case too, the numerical results were obtaining by implementing in the computational FE model the upper bounds curves of the true stress-true strain experimental curves sheaf of both materials. Although the chosen value for the friction coefficient can appear too high for metallic materials, it allows to establish the lower bound as regards to the response of metallic materials as compared to that corresponding to frictionless indentation.

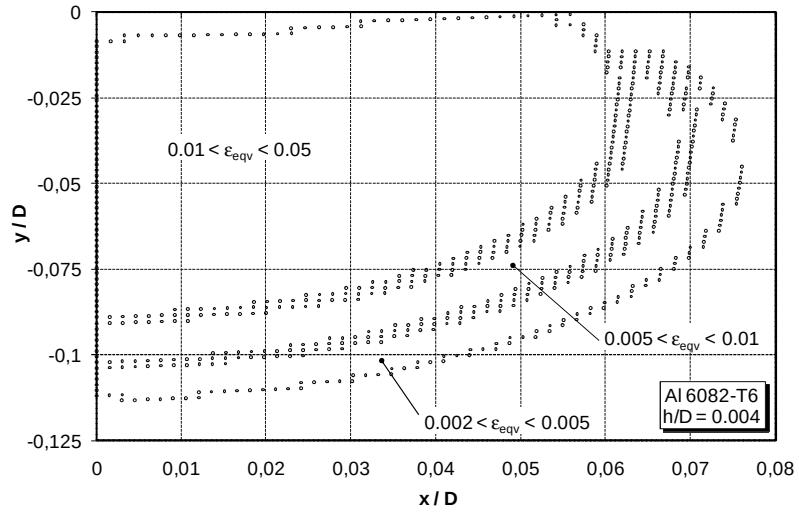

(a)

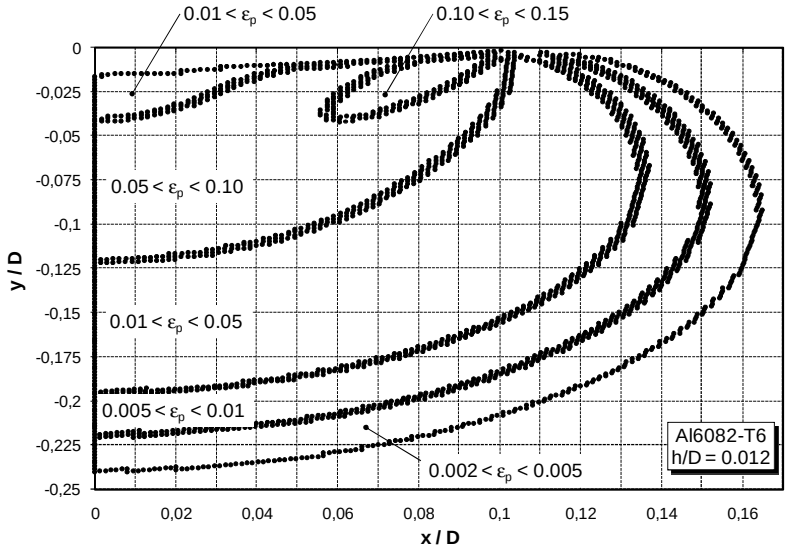

(b)

Figure 5.3. Frictional effects onto accumulated equivalent plastic strain ε_{eqv} field at different normalized indentation depths h/D in Al 6082-T6 alloy: (a) $h/D = 0.004$, (b) $h/D = 0.012$, (c) $h/D = 0.02$ and (d) $h/D = 0.04$. Friction coefficient $\mu = 0.5$.

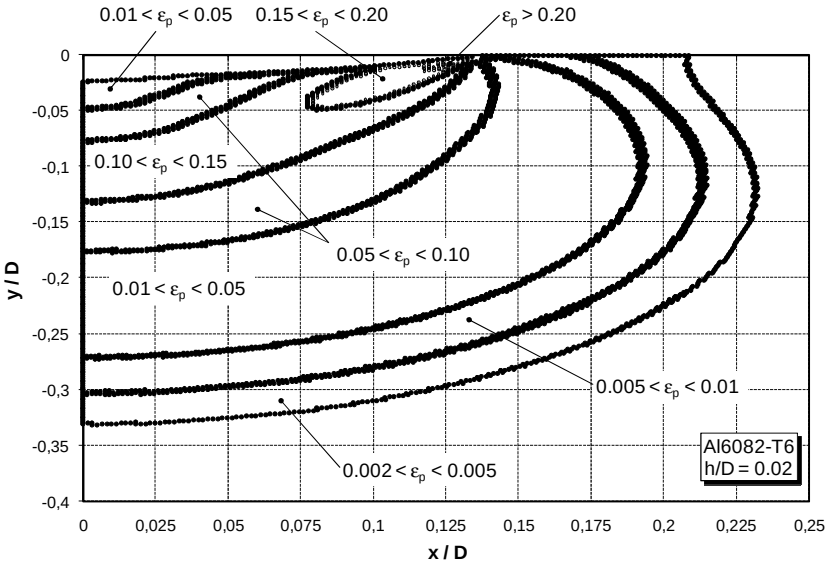

(c)

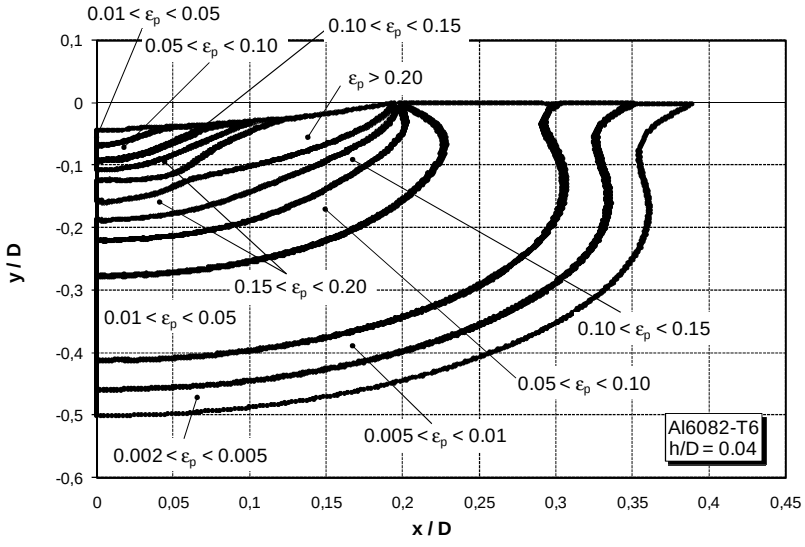

(d)

Figure 5.3. (Continued).

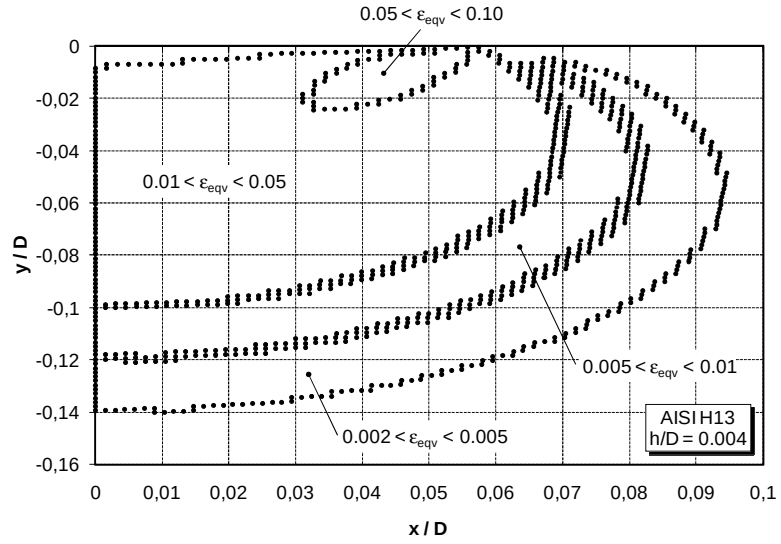

(a)

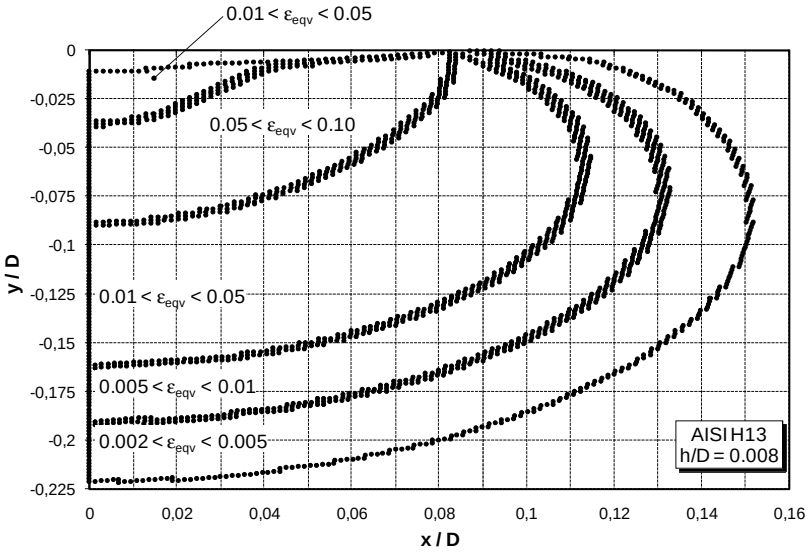

(b)

Figure 5.4. Frictional effects onto accumulated equivalent plastic strain ε_{eqv} field at different normalized indentation depths h/D in AISI H13 steel: (a) $h/D = 0.004$, (b) $h/D = 0.08$, (c) $h/D = 0.02$ and (d) $h/D = 0.04$. Friction coefficient $\mu = 0.5$.

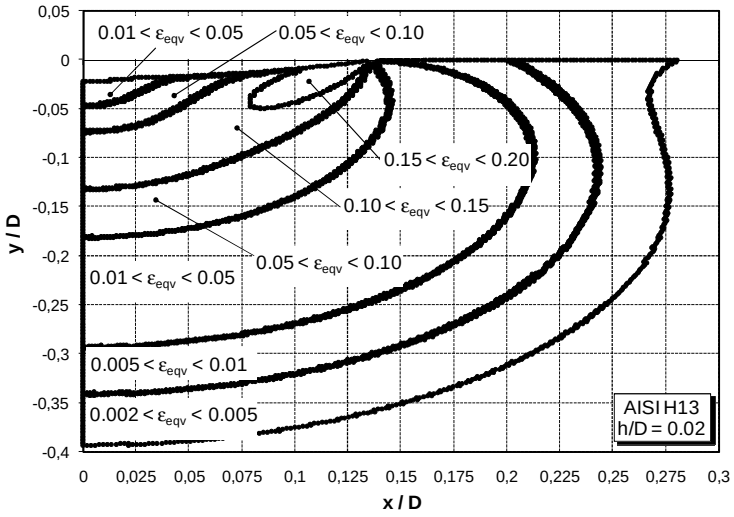

(c)

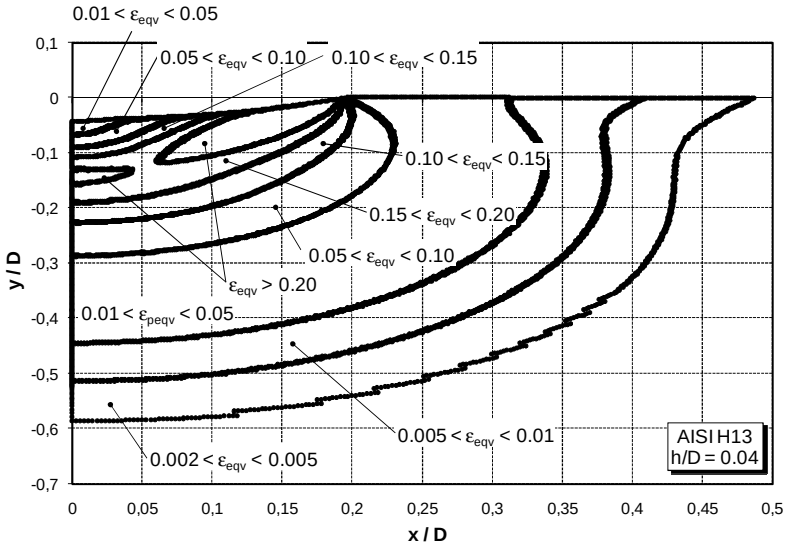

(d)

Figure 5.4. (Continued).

A preliminary analysis of the sequence of maps (Figs. 5.3 and 5.4) confirms that friction plays a crucial role in the definition of the plastic strains distribution in the sub-indenter region. The effects promoted by the friction onto the plastic strain field are various and depend on the penetration depth achieved by the indenter. Probably the most important feature, emerging from the analysis of the plastic zone evolution, concerns the increasing impact of frictional effects onto the material response as the indentation depth increases. The radial constraint effect is particularly significant at low penetration depths and it can be easily recognized in the reduced plastic activity in the sub-surface region around the indenter. For Al 6082-T6 alloy and AISI H13 steel the constraint effect is clearly detectable at a normalized penetration depth $h/D = 0.012$ (Fig. 5.3b) and $h/D = 0.008$ (Fig 5.4b), respectively. At these levels of penetration the low values of plastic strains in the narrow layer immediately beneath the indenter also suggest that tri-axial stress states dominate the straining processes in the sub-indenter region. As anticipated by Mesarovic and Fleck [], the final result is mainly represented by the development of a plastic core in the sub-indenter region characterized by higher plastic strains gradients, especially when the indentation depth takes the maximum values (Figs 5.3c-d and 5.4c-d). However, although friction plays a key role in the definition of the plastic strains distribution, it does promote a significant increment either of the material volume plastically strained or the plastic strain amount. For both investigated materials, the maximum depths reached by the plastic strains along the loading axis varies between $0.5D$ and $0.6D$, approximately (see Figs 5.3d and 5.4d).

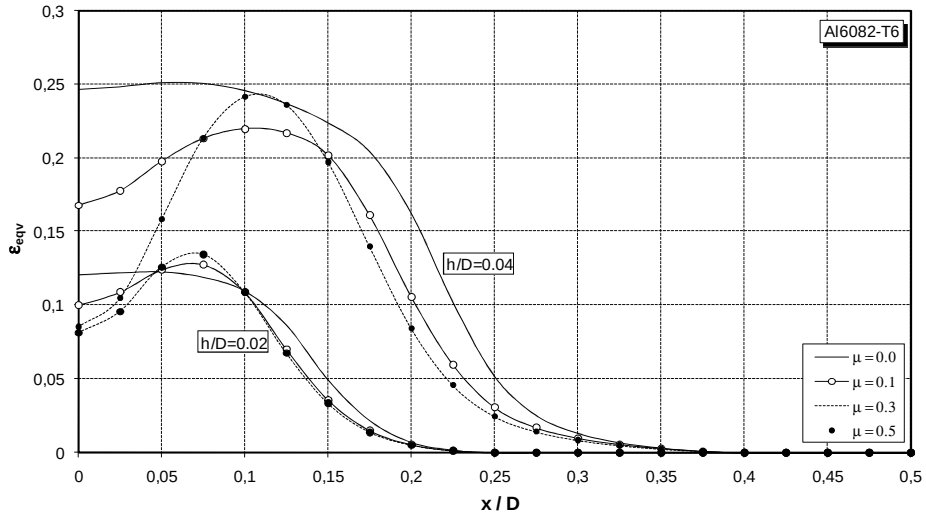

(a)

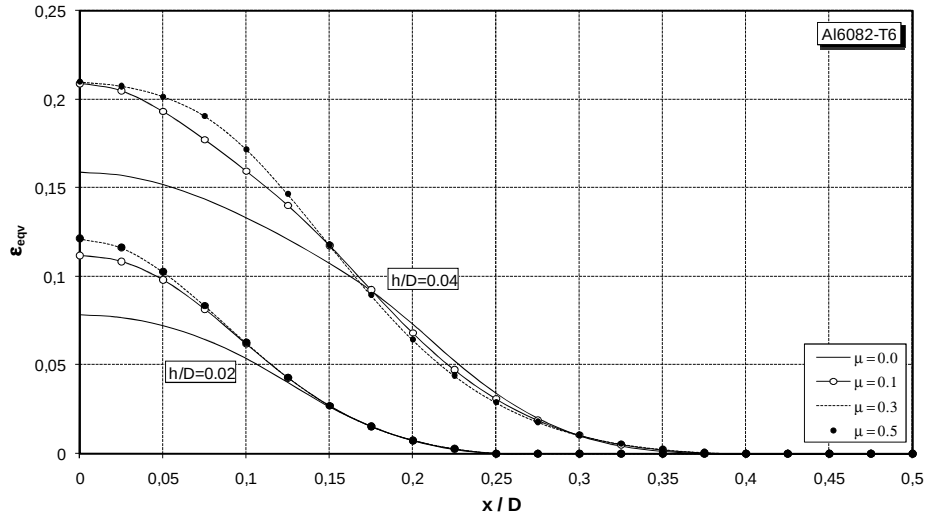

(b)

Figure 5.5. Accumulated equivalent plastic strain ε_{eqv} field at different normalized depths (y/D) in Al 6082-T6 alloy for the investigated friction conditions: (a) $y/D = 0.05D$, (b) $y/D = 0.10D$, (c) $y/D = 0.40D$.

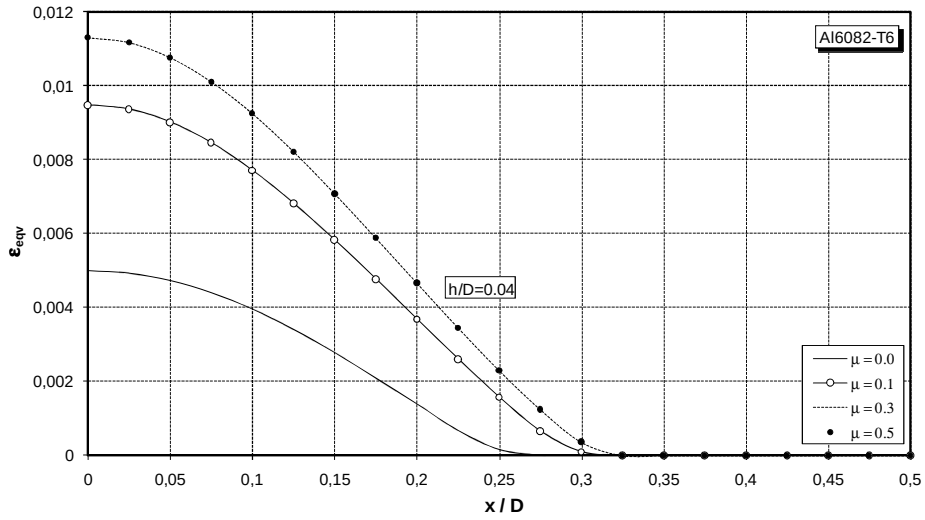

(c)

Figure 5.5. (Continued).

As shown by Figs. 5.1d and 5.2d, similar depths are attained by the plastic strains during frictionless indentation processes. As regards to the plastic strain amount, plastic strain values greater than 20% are confined in very limited regions in both materials responses and are comparable, in terms of size, to those induced by frictionless indenters. However, frictional effects can never be neglected, even though the friction coefficient takes very low values. Figs. 5.5 and 5.6 show the distribution of the accumulated equivalent plastic strains ε_{eqv} for four different contact conditions as a function of the radial distance x from the centreline and for three depths y $(0.05D, 0.10D, 0.40D)$ for Al 6082-T6 alloy and AISI H13 steel, respectively. Two values of penetrations are considered: $h/D = 0.02$

and $h/D = 0.04$. The maps at first probe that friction affects the solution in the entire plastic core under the indenter, as far as a radial distance x approximately equal to $0.3D$ for both considered materials (see Figs. 5.5d and 5.6d). In addition, by analysing the effect of the friction coefficient μ dependence on the curves, an important result seems to emerge. Friction modifies the results when the friction coefficient takes relatively low values, whereas a saturation is observed when it reaches medium-high values (Figs. 5.5 and 5.6).

The above mentioned evidences suggest that the information, which could be deduced by the local plastic strains distribution under the indenter, are strongly affected by the contact conditions, especially when the friction coefficient takes low values. By considering that these low values are typical for metallic materials and it is very difficult to establish *a priori* the friction coefficient between the indenter and the indented surface, the evaluation of stress-strain curves on the basis of the plastic strains field in the sub-indenter region seems particularly critical. Conversely, in consideration of the fact that, the overall response of the indented material at each stage of the loading cycle does not undergo significant modifications with respect to frictionless conditions, even though high friction conditions are considered, it reasonable to expect that the characteristic *L*-*h* curve is not affected by presence of friction, if, of course, the maximum indentation depth does not achieve extremes values. Therefore, the estimation of the constitutive properties via analysing the experimental data collected by the *L*-*h* curve probably represents the best way for obtaining the most accurate and reliable results about the material behaviour.

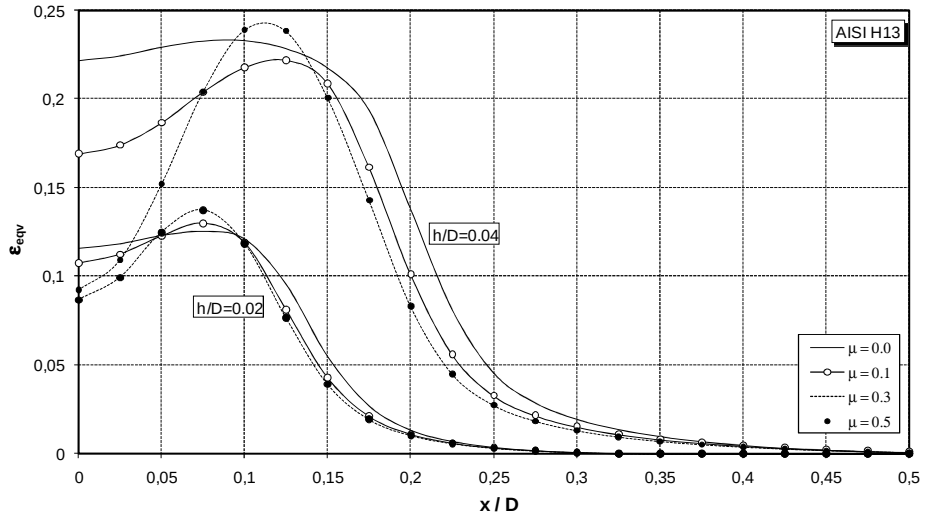

(a)

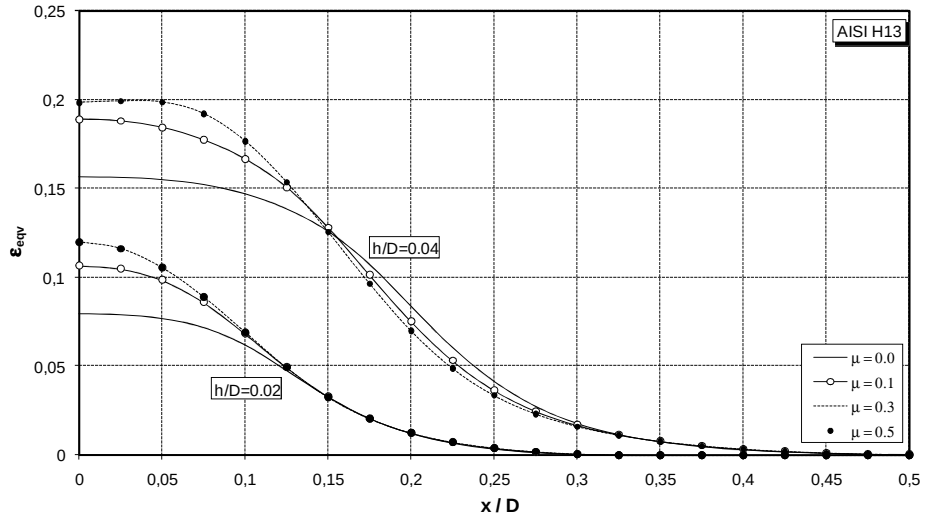

(b)

Figure 5.6. Accumulated equivalent plastic strain ε_{eqv} field at different normalized depths (y/D) in AISI H13 steel for the investigated friction conditions: (a) $y/D = 0.05D$, (b) $y/D = 0.10D$, (c) $y/D = 0.40D$.

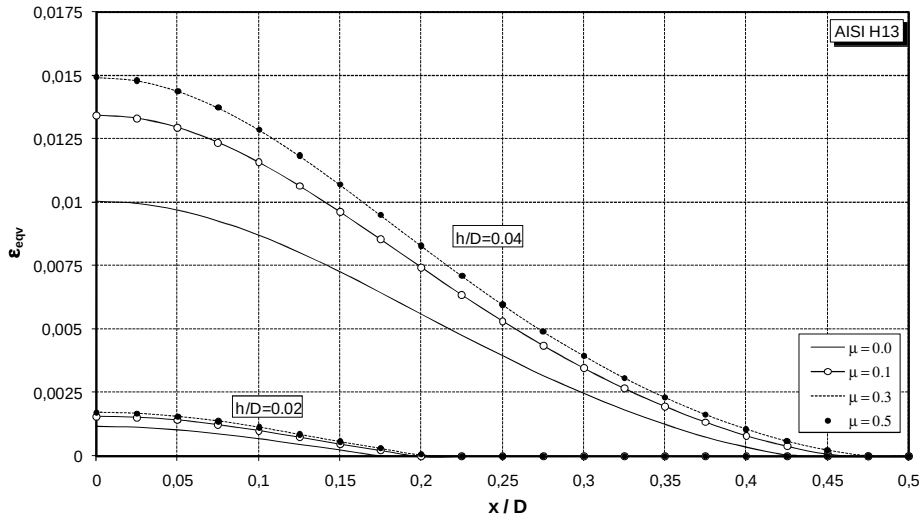

(c)

Figure 5.6. (Continued).

5.2 Crater profile evolution

5.2.1 Crater profile evolution in frictionless spherical indentation

The evolution of the crater profile determined by the plastic strains evolution described in section 5.1.1 is illustrated in Figs. 5.7 and 5.8 for Al 6082-T6 alloy and AISI H13 steel, respectively. As expected, for both investigated materials the well-known sinking-in and piling up phenomena characterize the evolution of the craters morphology (Figs. 5.7a and 5.8a).

For Al 6082-T6 (Fig. 5.7a), the sink-in regime dominates the indentation response at normalized indentation depths h/D lower

than 0.012, whereas the piling-up regime at h/D greater than 0.02. Between these two thresholds the crater profile evolution passes through a transition regime during which the material extrusion process can be easily appreciated (Fig. 5.7b). For AISI H13 steel sinking-in regime is found at very low normalized indentation depth h/D $(h/D < 0.004)$, the transition regime (Fig. 5.8b) at normalized indentation depths h/D ranging from 0.004 to 0.012, approximately, and, finally, the piling-up regime at deeper normalized indentation depths.

The evolution of the crater profile and its geometry, in both materials, confirm what was observed by Zhao et al. [28] and Beghini et al. [57]. Remarkable modifications are detectable in the crater geometry, even though small increments in the penetration depth are considered (see Figs. 5.7b and 5.8b). In addition, the craters geometry is always characterized by high gradients, especially as regards to the region around the crater rim. The inner region of the impressions near to the rim is particularly affected by these evidences. This fact also explain the encountered difficulties in measuring the crater profile via non-contacting profilometers.

Therefore, under these conditions, the determination of the actual contact diameter appears to be a challenge. Accordingly, it should not be surprising if the estimation of the constitutive properties involving the analysis of the crater geometry promoted by the indenter, is characterized by a certain degree of uncertainness.

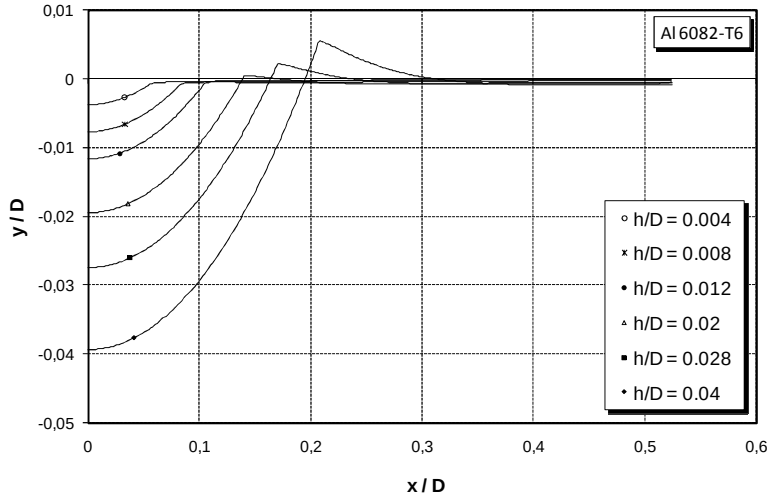

(a)

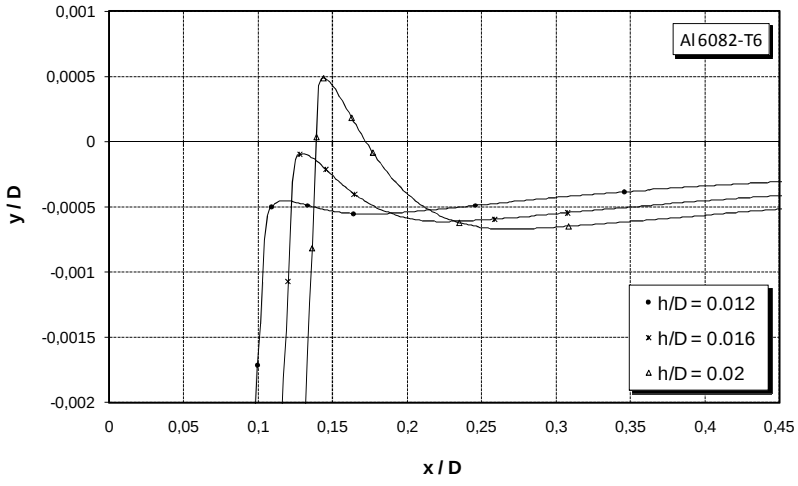

(b)

Figure 5.7. Crater profile evolution during the simulated frictionless indentation test for Al 6082-T6 alloy: (a) sinking-in and piling-up regimes, (b) detail of the crater rim showing the material extrusion process during the transition regime.

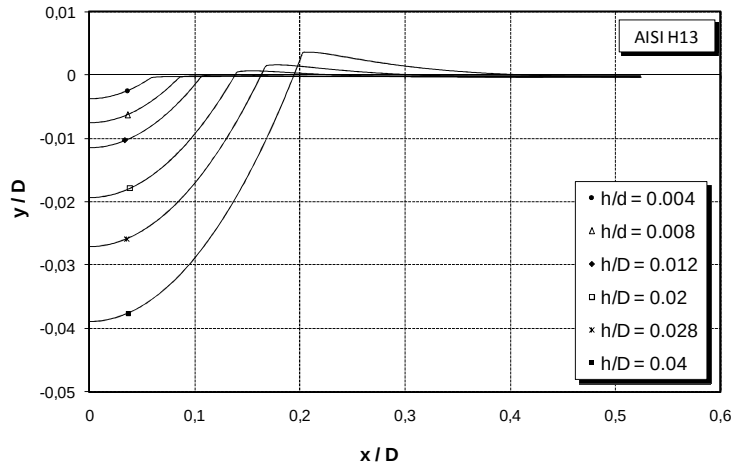

(a)

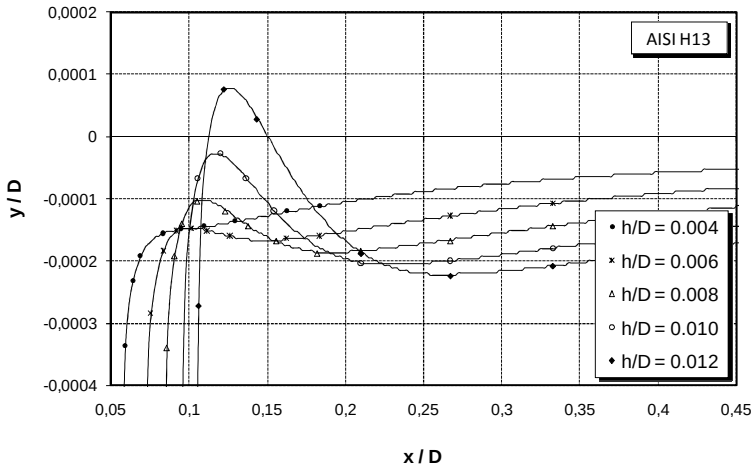

(b)

Figure 5.8. Crater profile evolution during the simulated frictionless indentation test for AISI H13 steel: (a) sinking-in and piling-up regimes, (b) detail of the crater rim showing the material extrusion process during the transition regime.

5.2.1 Frictional effects onto the crater profile evolution

In the previous analysis of the crater profile evolution frictional effects were not taken into account. However, the presence of friction between the indenter and the target cannot be ignored. Taljat et al. [65] showed that friction plays a key role in the sinking-in and piling-up phenomena. The authors found that friction significantly reduce the material piling-up amounts in strain-hardening solids obeying to the Hollomon power constitutive law. It was found that the amount of the material piling-up decrease is a function of the yield strength and are relevant for materials having relatively low large ratio between the elastic modulus E and the yielding stress σ_{yp}. Such effects become more and more important if the strain-hardening coefficient n takes small values. Similar findings were also obtained by Habbab et al. [62].

Frictional effects onto the crater profile evolution are shown in Figs. 5.9 and 5.10 for Al 6082-T6 alloy and AISI H13 steel, respectively. The numerical predictions are referred to a friction coefficient $\mu = 0.5$. The depicted scenarios confirm the above-mentioned evidences in both materials. The effects of friction are twofold in the definition of the impression morphologies. At first, although sinking-in and piling-up phenomena can be still recognized in the both crater profile evolutions (see Figs. 5.9a and 5.10a), the transition between the two regimes is strongly delayed: for Al 6082-T6 alloy the transition occurs at a normalized indentation depth $h/D = 0.028$, whilst for AISI H13 steel at $h/D = 0.02$.

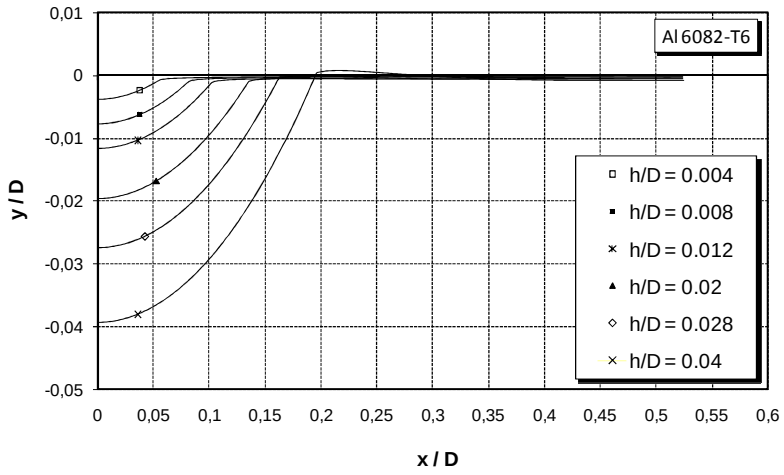

(a)

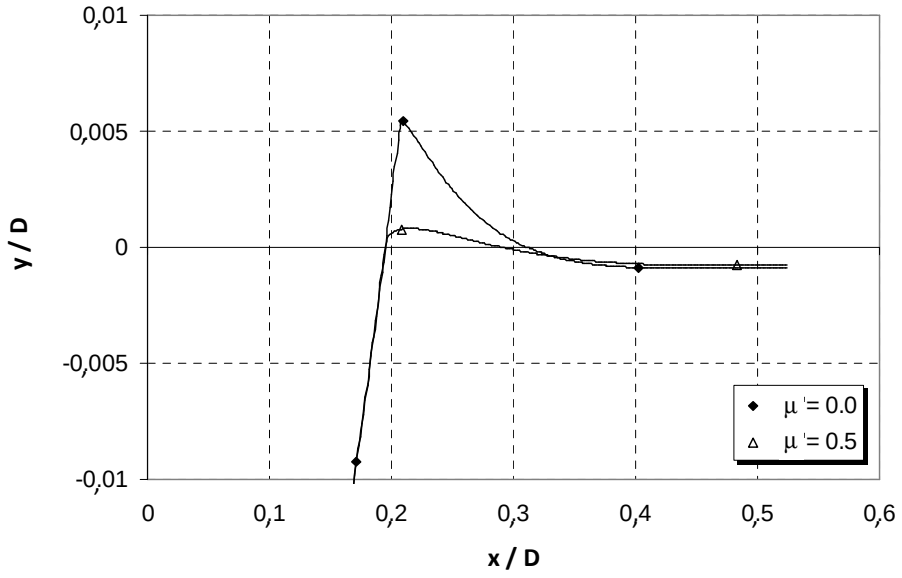

(b)

Figure 5.9. Frictional effects onto crater profile evolution for Al 6082-T6 alloy (friction coefficient $\mu = 0.5$): (a) sinking-in and piling-up regimes, (b) detail of the crater rim evolution showing the material piling up amounts corresponding to the extreme investigated contact conditions.

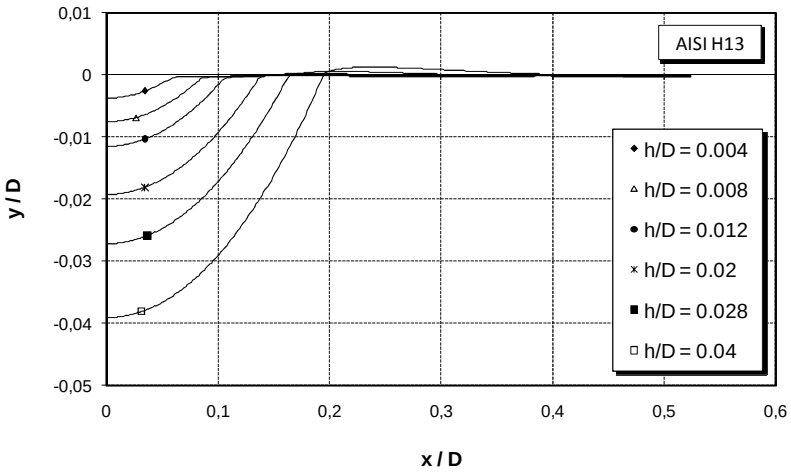

(a)

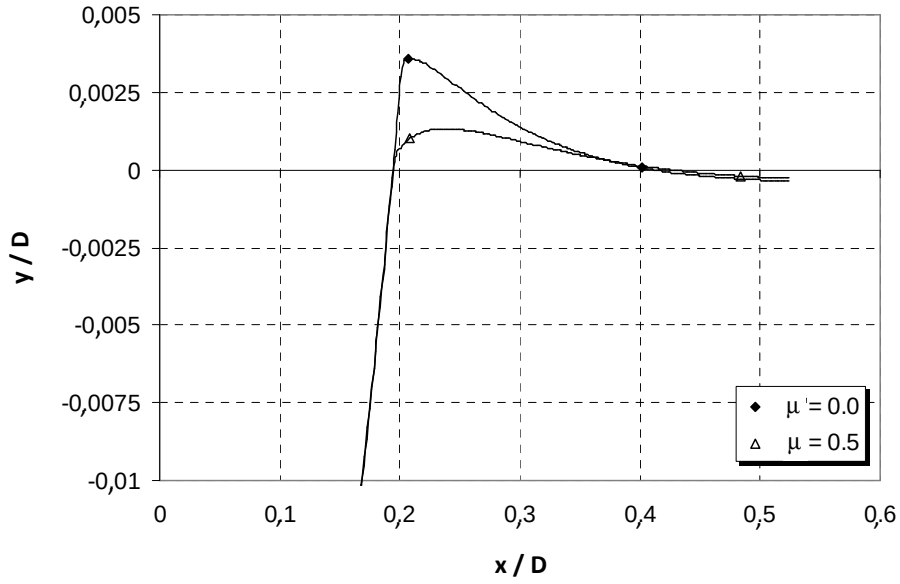

(b)

Figure 5.10. Frictional effects onto crater profile evolution for AISI H13 steel (friction coefficient $\mu = 0.5$): (a) sinking-in and piling-up regimes, (b) detail of the crater rim evolution showing the material piling up amounts corresponding to the extreme investigated contact conditions.

For frictionless indentation the transition was found to occur in Al 6082-T6 at $h/D < 0.012$, whilst for AISI H13 sinking-in regime was found nearly absent.As regards to the amounts of material piling-up at the maximum indentation depth reached during the indentation test $(h/D = 0.04)$, dramatic decrease of 85% and 63% for Al 6082-T6 alloy and AISI H13 steel was found, respectively, with respect to those observed in frictionless indentation. The higher values obtained by the aluminum alloy suggests that the material strain-hardening capabilities are much more important than the material yield strength in the piling-up phenomena. Although the presented results are obtained by considering very high friction conditions, comparable decreases of the material piling-up were observed also for low values of the friction coefficient, typically from 0.05-0.2, thus proofing that the crater geometry is particularly sensitive to this experimental parameter. Unfortunately, these values of the friction coefficient are typical for the metallic materials [55,58].

As also argued by Beghini et al. [60], it is impossible to establish a priori the effective value of the friction coefficient between the indenter and the target during the indentation test. The high values plastic strains occurring in the region immediately in contact with the indenter also suggest that this parameter may vary during the test. Accordingly, such evidences further confirm the poor accuracy which may characterize those methodologies [55, 65] aimed at determining the constitutive properties of the indented material via a proper analysis of the crater geometry.

5.3 Frictional effects onto the load – indentation depth curve

Although the characteristic *L*-*h* curve provides an averaged response of the indented material, it is possible to deduce the constitutive properties via a proper analysis of the trend corresponding to the loading cycle [28,55,57-59,76,77]. As regards to the role of friction in the definition of the *L*-*h* curve trend, Lee et al. [] found that typical values of friction coefficients $(0.0 < \mu < 0.5)$ for metallic materials do not affect the *L*-*h* curve if the maximum indentation depth does not exceed 15% of the indenter diameter. Conversely, Cao et al. [59] observed non negligible modification in the curve curvature C, if penetration depths till to 30% are attained during the loading cycle. These results are consistent with what was obtained in the present investigation. The comparisons between the *L*-*h* curves for four values of the friction coefficients are reported in Fig. 5.11 for both Al 6082-T6 alloy and AISI H13 steel. Here, the friction coefficient μ was assumed to vary between 0.0 to 0.5. The maximum penetration depth was fixed at 4% of the indenter diameter. As emerged from the analysis of the plastic core evolution in the investigated material, such degree of penetration promote and adequate volume of material plastically strained and plastic strains values such ensuring the estimation of the first part of the stress-plastic stain curve of indented materials. By analysing the predicted trends, the effect of friction appear negligible. The maximum relative difference was found to be within 0.3%. However, a trend toward a progressive spread among the curves at highest penetration depth was observed, thus confirming that the increasing frictional effects into the sub-indenter

regions, in terms of plastic strains distributions, are progressively recognized by the characteristic L-h curve as the indentation depth increase.

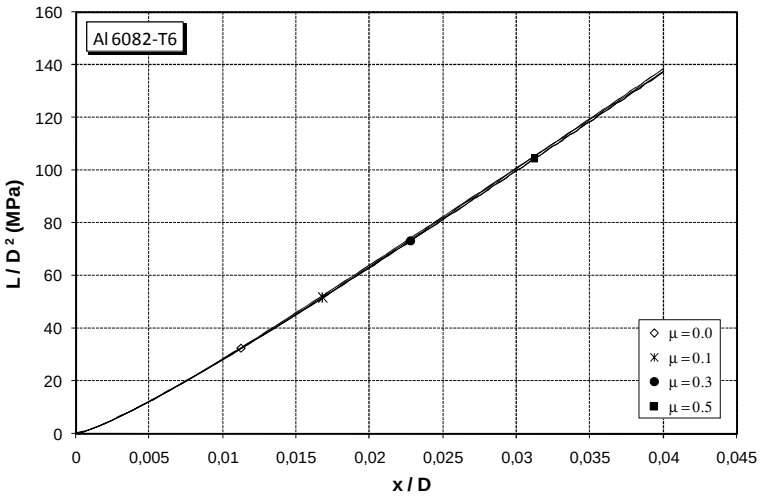

(a)

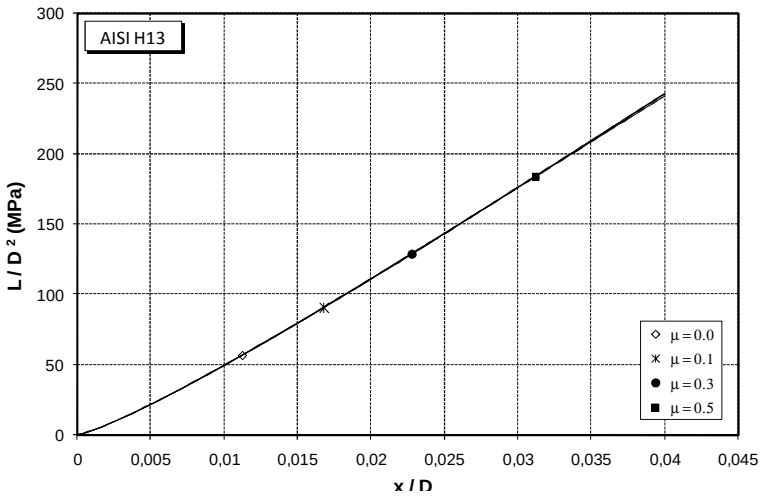

(b)

Figure 5.11. Frictional effects onto *L-h* curves: (a) Al 6082-T6 alloy, (b) AISI H13 steel.

The negligible influence of friction on *L*-*h* curves seems to suggest that this parameter could be neglected in those evaluation procedure [28,57-59,76,77] aimed at predicting the elastic-plastic material properties from the *L*-*h* curve.

5.4 Summary

There are no doubts that for correctly interpreting the experimental indentation response, i.e. the characteristic *L*-*h* curve and the crater profile evolution, the knowledge of the straining phenomena occurring in the sub-indenter region is mandatory, especially if the indentation response is used to deduce the constitutive properties of the indented material. Therefore, the present chapter was devoted to carried out a detailed analysis of the straining process into real materials (Al 6082-T6 alloy and AISI H13 steel), in order to establish if the experimental indentation response is effectively representative of the indented material, from one side, and distinguishing, from the other side, the most reliable experimental source of information from which the constitutive behavior of the indented material can be deduced. The analysis of the indentation response was also performed taking into account the effects of friction which represents the most important experimental parameter in the indentation testing. From the analysis of the crater profile and plastic strain evolutions and the characteristic *L*-*h* curve the following conclusions can be drawn:

1. among the potential source of experimental data, which can be used for deducing the stress-strain curves of metallic materials, the characteristic *L*-*h* curve is surely the most reliable in terms of accuracy;
2. the effects of friction onto the trend of the *L*-*h* curve are negligible if extremes depths are not achieved, whilst they are remarkable in the definition of the plastic strains distribution in the sub-indenter region and in the crater profile evolution;
3. frictional effects onto the plastic strains distribution and crater profile evolution are remarkable even though the corresponding friction coefficient takes low values, as usually occur for metals, thus undermining the accuracy and reliability of those evaluation procedures, based on the analysis of the local strains and impression geometry, for inferring the stress-strain curve of the indented material;
4. large values of the maximum indentation depth are not necessary for inferring the constitutive properties of the indented material. Maximum values of the indentation depth around the 4% of the indenter diameter are sufficient to promote an adequate material volume plastically strained, thus obtaining an effective representative response of the material behaviour.

On the basis of such results, in the next section a new evaluation procedure able to estimate the plastic properties of linear elastic-strain-hardening materials obeying to Hollomon constitutive law through a proper analysis of the characteristic *L*-*h* curve is presented.

CHAPTER 6
Direct and reverse analysis. Setup and assessment of the algorithms

The reliability of the load-indentation depth curve as a source of information for inferring the constitutive properties of metallic materials by was probed in the previous chapter. It was also shown that those methodologies estimating the constitutive properties via the analysis of such curve, should be preferred. However, the validity of any evaluation procedure does not depend only on the quality of the source of information. A key role is also played by the algorithm used for interpreting the experimental data and deducing from them the constitutive law.

In this frame, the present chapter is aimed at analyzing in detail the direct and reverse analyses proposed by Beghini et al. [57], being demonstrated particularly promising for inferring the constitutive properties from the analysis of *L*-*h* curves. To improve the predictive capability of the algorithm, a new database of *L*-*h* curves is generated by using the computational FE model previously developed and consequently new correlations between the parameters characterizing the Hollomon constitutive law and the corresponding *L*-*h* curve are proposed (direct analysis). In this frame,

the comparison criterion adopted by the reverse analysis is also analyzed. The improvements brought by the methodology are assessed by implementing and comparing the predicted and experimental material stress-strain curves for the previously tested Al 6082-T6 alloy.

6.1 Direct analysis

6.1.1 Material model and L-h curves database

For inferring the constitutive properties of any material through the comparison between its experimental *L-h* curve and a reference *L-h* curve, the definition of a reference material model is needed at first. It must be also established the correlations between the *L-h* curve and the parameters characterizing the reference material model.

$$\sigma = \begin{cases} E\varepsilon & \varepsilon \leq \varepsilon_{yp}\ (=\frac{\sigma_{yp}}{E}) \\ \sigma_{yp}\left(\frac{\varepsilon}{\varepsilon_{yp}}\right)^{n} & \varepsilon > \varepsilon_{yp} \end{cases} \qquad 0 < n < 0.5 \qquad (6.1)$$

Hollomon constitutive law (Eqn. (6.1)) surely represents a good approximation for a large number of metallic materials. The few number of constitutive parameters, the elastic modulus E, the proportionality limit σ_{yp} and the strain-hardening coefficient n, allows to develop relatively simple algorithms for deducing these constitutive parameters, thus making it possible to evaluate easily the errors done in the estimation of the unknown variables. Adopting this constitutive framework, the material behaviour is completely defined

once the aforementioned parameters and the Poisson ratio ν are known.

However, it should be noted that the proportionality limit σ_{yp} and the strain-hardening coefficient n surely represents the most important parameters for metallic materials. The Poisson ratio is near to 0.3 for almost all metals and the case in which the elastic modulus E of a metallic material is completely unknown can be considered very rare. Also, within each class of metallic materials the Young modulus E can be considered approximately a constant parameter [Beghini]. From this point of view, the approach proposed by Beghini et al. [] does not appear limited. Moreover, although the authors examined the material behaviour of steels, aluminum alloy and copper alloys, only, the developed procedure may be easily extended to a wide range of metallic materials. In this frame, the determination of the correlations between the *L*-*h* curve and the material plastic properties (σ_{yp}, n) represents the first crucial point. As shown by Beghini et al. [57], such correlations can be easily determined simulating the indentation process via finite element analysis and generating a database of *L*-*h* curves corresponding to a suitable number of the constitutive parameters combinations. An appropriate fitting of the numerical *L*-*h* curves can then provide the aforementioned relationships.

The database architecture developed by Beghini et al. [57] was presented in Section 3.4. The basic structure proposed was maintained but, in order to extend the predictive capabilities of the algorithm, the plastic properties domain was extended. The same ranges, within which the proportionality limit and strain-hardening

coefficient were allowed to vary, were used. *L-h* curves of steels, aluminum alloys and copper alloys were obtained using the computational FE model described in Chapter 5. Each class of materials was identified by a specific values of the elastic modulus and values of the elastic moduli equals to 205 GPa, 70 GPa and 120 GPa were assumed for steels, aluminum alloys and copper alloys classes, respectively. The Poisson ratio was fixed equal to 0.3. For the three classes of materials the proportionality limit σ_{yp} was chosen in the range $50 \leq \sigma_{yp} \leq 2000$ MPa (with a step of 100 MPa between 100 MPa and 2000 MPa), whilst the strain-hardening coefficient n in the range from 0.01 to 0.5 with a step of 0.05. More than 180 *L-h* curves for each class of materials.

As revealed by the analysis of the plastic deformation process in Al 6082-T6 alloy and AISI H13 steel (see Chapter 5), a maximum indentation depth h/D equal to 4% of the indenter diameter does not introduce remarkable frictional effects in the *L-h* curve trend and it is sufficient to obtain a representative response from the indented material. Consequently, all the numerical *L-h* curves were generated by simulating a frictionless indentation process in which the maximum penetration depth was fixed at 4% of the indenter diameter. The number M of the points couples (L, h) used to represent each numerical *L-h* curve was established by analysing the error done in the *L-h* curves interpolation: $M = 100$ points couples was found to provide very good results in terms of fittings.

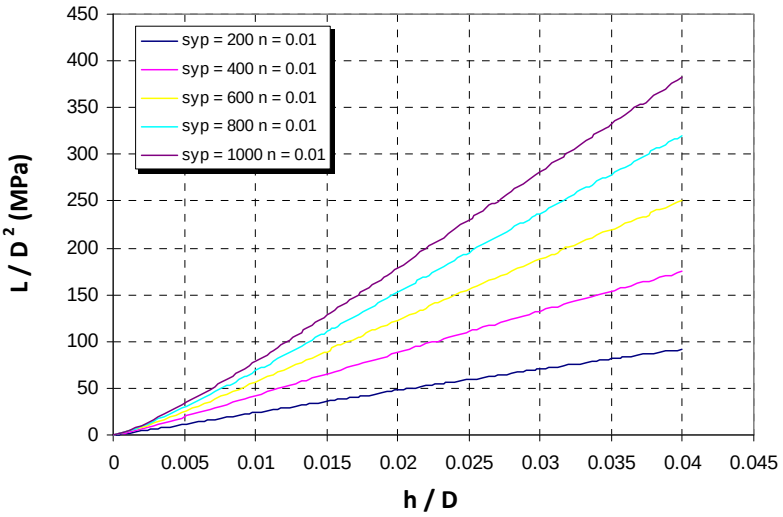

(a)

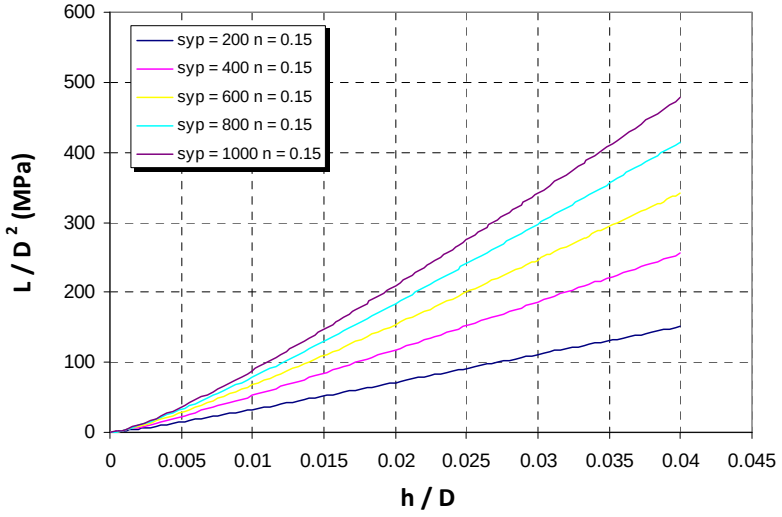

(b)

Figure 6.1. *L*-*h* curves for different values of the proportionality limit σ_{yp} and strain-hardening coefficient n of the steels class: (a) $200 \leq \sigma_{yp} \leq 1000$ MPa, $n \cong 0.0$ and (b) $200 \leq \sigma_{yp} \leq 1000$ MPa, $n \cong 0.15$.

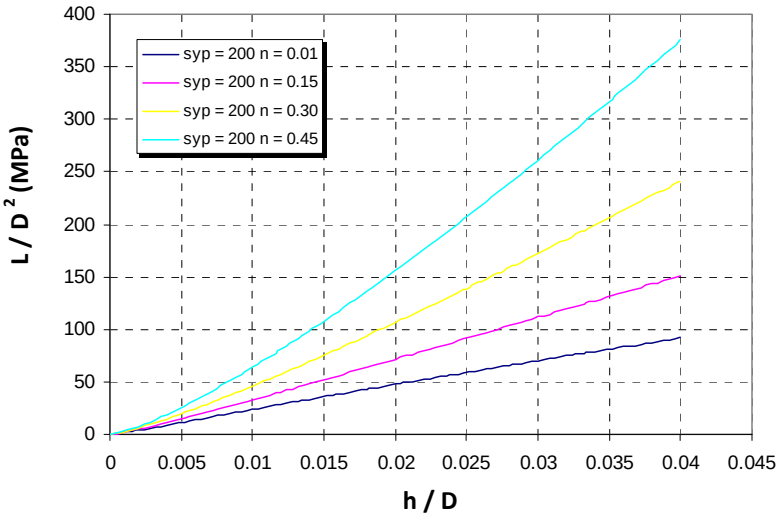

(a)

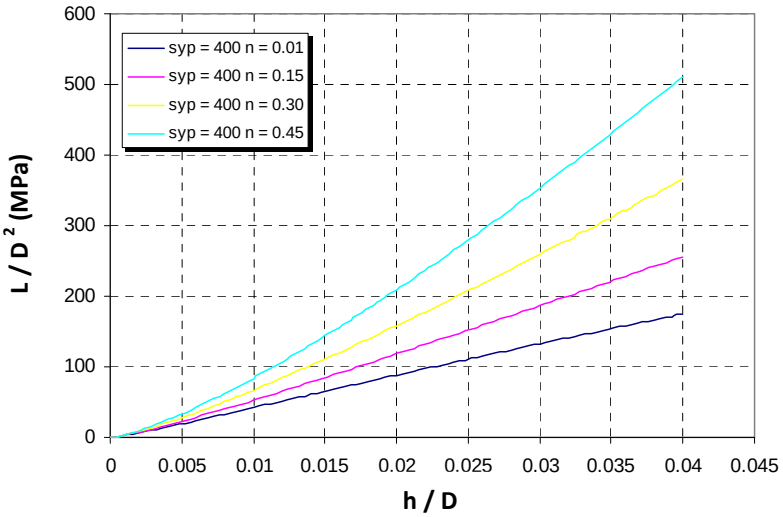

(b)

Figure 6.2. *L-h* curves for different values of the proportionality limit σ_{yp} and strain-hardening coefficient n of the steels class: (a) $\sigma_{yp} = 200$ MPa, $0.0 \leq n \leq 0.45$ and (b) $\sigma_{yp} = 400$ MPa, $0.0 \leq n \leq 0.45$.

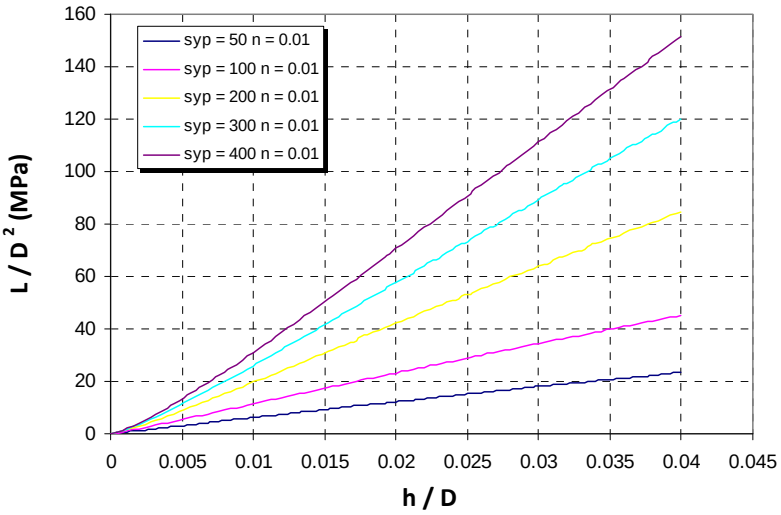

(a)

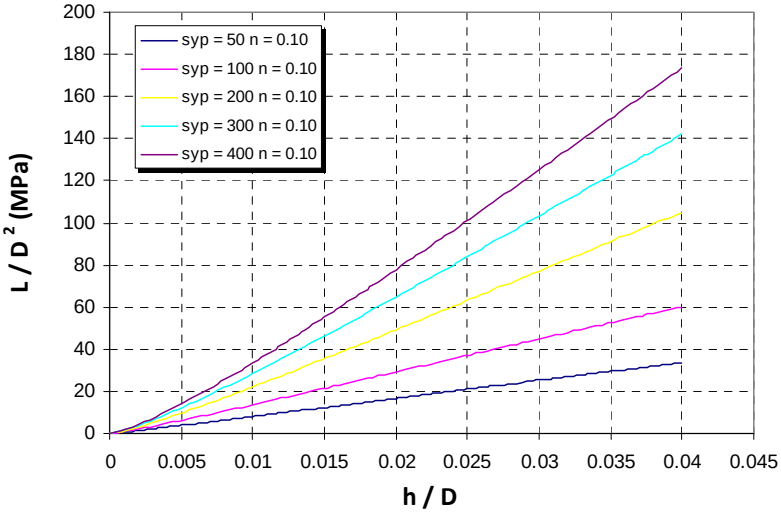

(b)

Figure 6.3. *L*-*h* curves for different values of the proportionality limit σ_{yp} and strain-hardening coefficient n of the aluminum alloys class: (a) $50 \leq \sigma_{yp} \leq 400$ MPa, $n \cong 0.0$ and (b) $50 \leq \sigma_{yp} \leq 400$ MPa, $n \cong 0.10$.

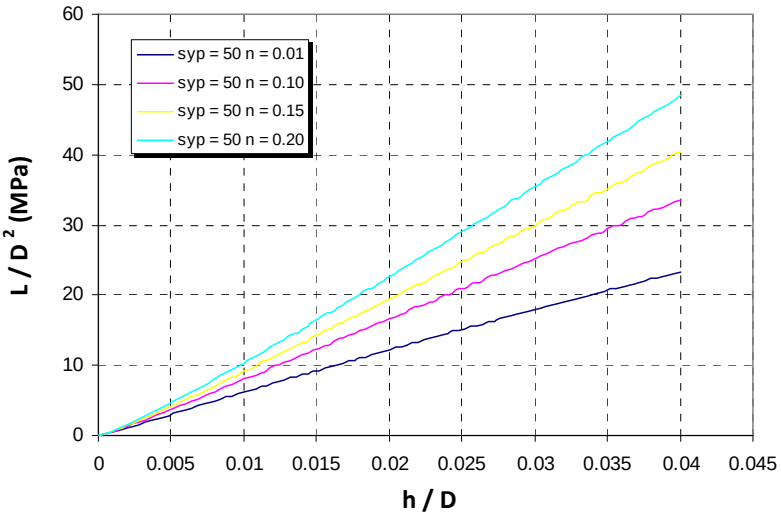

(a)

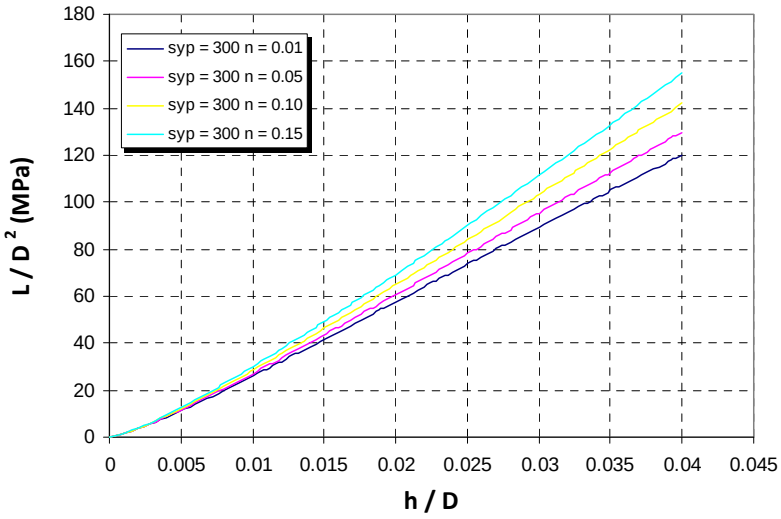

(b)

Figure 6.4. *L-h* curves for different values of the proportionality limit σ_{yp} and strain-hardening coefficient n of the aluminum alloys class: (a) $\sigma_{yp} = 50$ MPa, $0.0 \leq n \leq 0.20$ and (b) $\sigma_{yp} = 300$ MPa, $0.0 \leq n \leq 0.15$.

Figs. 6.1 to 6.4 illustrate some examples of the *L-h* curves for steels and aluminum alloys classes contained in the database. The effects of the proportionality limit (Figs. 6.1and 6.3) and strain-hardening coefficient (Figs. 6.2 and 6.3) onto the trend of the *L-h* curve can be appreciated in both classes of materials. Each *L-h* curve appears clearly distinguishable.

6.1.2 L-h curves interpolation

The correlations between the *L-h* curve, the proportionality limit σ_{yp} and the strain-hardening coefficient n was performed into two steps [83]. Interpolating function which provides the best fitting of each numerical *L-h* curve was firstly assessed. Subsequently, the correlations between the coefficients of the fitting function and the constitutive parameters were established. Accordingly, two levels of interpolations are needed to perform the direct analysis.

From the analysis of the numerical *L-h* curves, it was found that the best fitting of any numerical *L-h* curve of the database can be obtained adopting the following expression:

$$\frac{L}{ED^2} = \sum_{k=1}^{4} A_k \left(\frac{h}{D}\right)^{c_k} \qquad (6.2)$$

where D is the indenter diameter and E the elastic modulus denoting the material class. A base of power law function, defined by the exponents c_k was firstly selected and the fitting parameters A_k were determined subsequently by fitting procedure. The selection of the

fitting functions was based on a statistical approach that will be explained in the next paragraphs. Keeping in mind that each numerical *L*-*h* curve is defined by a set of M points couples (L, h), Eqn. (6.2) can be rewritten in the following matricial form:

$$\begin{pmatrix} \frac{L_1}{ED^2} \\ \vdots \\ \frac{L_M}{ED^2} \end{pmatrix} = \begin{bmatrix} \left(\frac{h_1}{D}\right)^{c_1} & \cdots & \left(\frac{h_1}{D}\right)^{c_4} \\ \vdots & \vdots & \vdots \\ \left(\frac{h_M}{D}\right)^{c_1} & \cdots & \left(\frac{h_M}{D}\right)^{c_4} \end{bmatrix} \begin{bmatrix} A_1 \\ A_2 \\ A_3 \\ A_4 \end{bmatrix} \Leftrightarrow \boldsymbol{L} = \boldsymbol{H} \cdot \boldsymbol{A} \qquad (6.3)$$

where $\boldsymbol{L}$, $\boldsymbol{H}$ and $\boldsymbol{A}$ denotes the array of the loads $\left(\frac{L}{ED^2}\right)$, the matrix of the coefficients $\left(\frac{h}{D}\right)^{c_k}$ and the array of the unknown variables A_k, respectively. Due to the dimensions of the arrays $\boldsymbol{L}$ and $\boldsymbol{H}$, the evaluation of the fitting parameters A_k was carried out using the Normal Equation Method (NEM). The base of coefficients c_k was selected in order to reproduce, as truly as possible, in terms of the *L*-*h* curve trend the straining phenomena induced by the indenter during the indentation response.

The fitting capability can be checked by determining the error in reproducing the set of M points couples for any *L*-*h* curve. To improve the accuracy of fitting, a statistical approach was used for fixing the exponents c_k. For any given base of the coefficients c_k, the fitting parameters A_k were firstly determined through Eqn. (6.3) for each numerical *L*-*h* curve of the database via NEM. The computed values were then used to reconstruct the theoretical L^{th}-h^{th} curve, thus making it possible to establish the relative error done in this first level of interpolation. Relative error estimation was performed by

comparing for each level of the penetration depth h^{FE} predicted by the Finite Element (FE) analysis, the corresponding loads provided by the numerical modelling and the interpolating function (Fig. 6.5a). Eqn. (6.4) was used to reconstruct the theoretical L^{th}-h^{th} curve,

$$\frac{L^{th}}{ED^2} = \sum_{k=1}^{4} A_k \left(\frac{h^{FE}}{D}\right)^{C_k} \quad (6.4)$$

The relative error e_m $(m = 1, \dots, M)$ was estimated as follow for each points couple:

$$e_m = \frac{L^{th}(h_m^{FE}, E, \sigma_{yp}, n) - L_m^{FE}}{L_m^{FE}} \quad (6.5)$$

Eqn. (6.4) was also used to compute the maximum relative error done in the interpolation of each numerical *L*-*h* curve.

$$\Delta L = max_{m=1,\dots,M} |e_m| \quad (6.6)$$

Following the same procedure, the relative error e_m and the corresponding maximum relative error Δh were evaluated also for indentation depth *h* variable (Fig. 6.5b). In this case, the following expression,

$$e_m = \frac{h^{th}(L_m^{FE}, E, \sigma_{yp}, n) - h_m^{FE}}{h_m^{FE}} \quad (6.7)$$

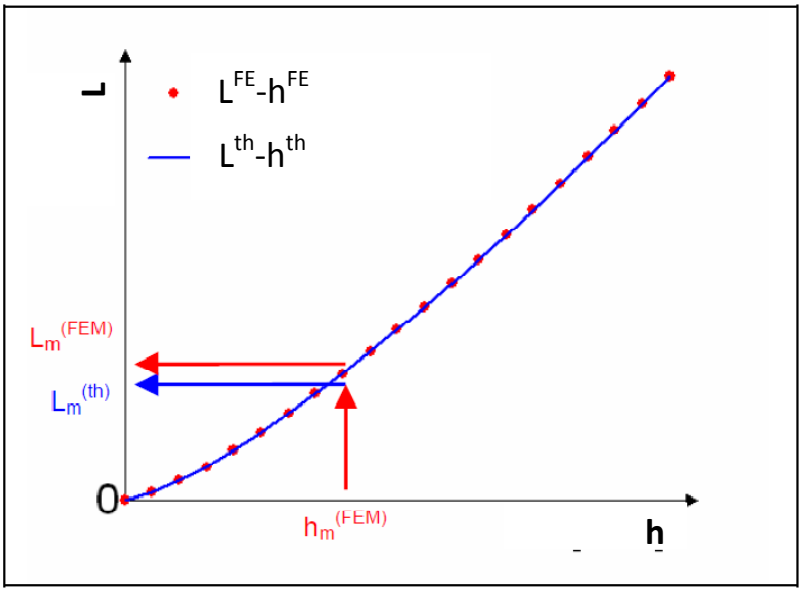

(a)

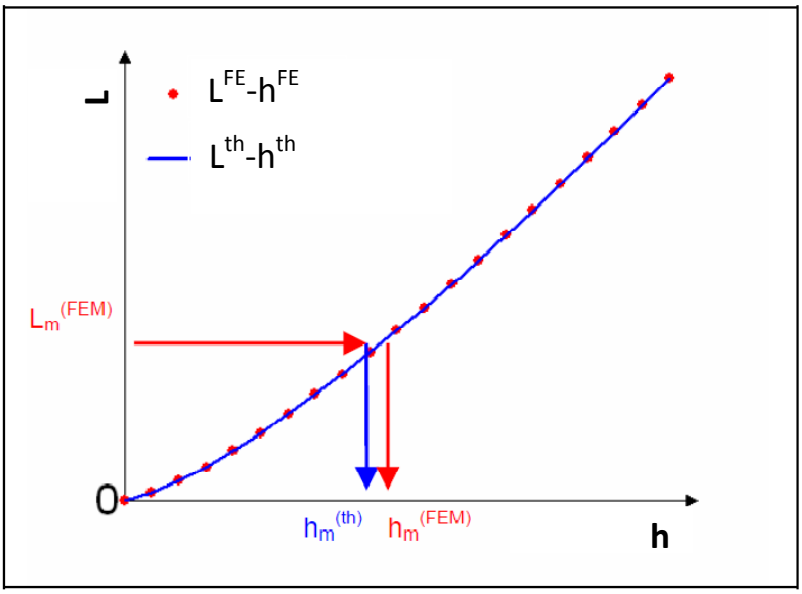

(b)

Figure 6.5. Schematic representation of the evaluation of the relative error e_m for (a) load *L* and (b) the penetration depth *h* variables.

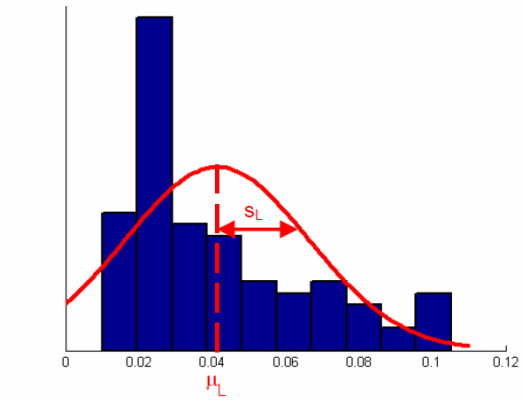

(a)

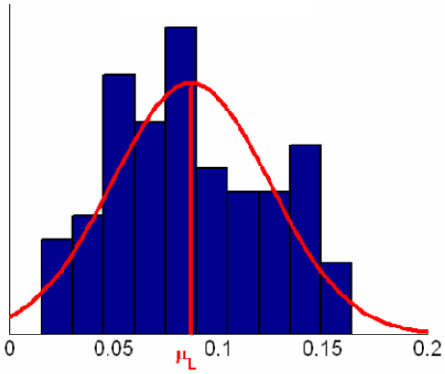

(b)

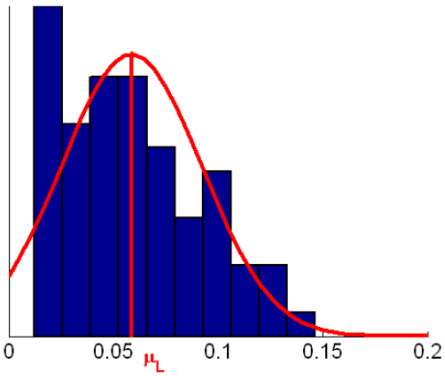

(c)

Figure 6.6. Frequencies histograms of the discrete distributions ΔL for (a) Al-alloys class, (b) steels class and (c) Cu-alloys class. First level of interpolation.

was used to calculate the relative error e_m , whereas the expression for Δh is still given by Eqn. (6.6).

The discrete distributions of the maximum relative errors ΔL and Δh over the entire database were then established and the mean values

$$\mu_L = \frac{\sum_{p=1}^{P}\sum_{q=1}^{Q}\Delta L_{\mathrm{pq}}}{P\cdot Q}\,, \qquad \mu_h = \frac{\sum_{p=1}^{P}\sum_{q=1}^{Q}\Delta h_{\mathrm{pq}}}{P\cdot Q} \tag{6.7}$$

and corresponding standard deviations

$$s_L = \sqrt{\frac{\sum_{p=1}^{P}\sum_{q=1}^{Q}(\Delta L_{\mathrm{pq}}-\mu_L)^2}{P\cdot Q-1}}\,, \qquad s_h = \sqrt{\frac{\sum_{p=1}^{P}\sum_{q=1}^{Q}(\Delta h_{\mathrm{pq}}-\mu_h)^2}{P\cdot Q-1}} \tag{6.8}$$

were evaluated for each distribution. Fig. 6.6 illustrates the frequencies histograms of the discrete distribution ΔL for the analyzed classes of metallic materials.

The statistical approach allowed to establish how the interpolation error, done in the reconstruction of each numerical *L*-*h* curve, varies in the entire database and especially how it is affected by the selection of the parameters c_k. The exponents c_k must be selected in order to reproduce as truly as possible the typical indentation response of metallic materials. Different bases may be used to this purpose. However, to improve the accuracy of the first level of interpolation, it was selected, among the potential bases, the set of parameters c_k which reduces the mean values and the standard deviations given by Eqns. (6.7) and (6.8).

6.1.3 Dependence of A_k coefficients on σ_{yp} and n

The dependence on the plastic properties (σ_{yp}, n) must be determined. The correlation was obtained after analysing the trends of the coefficients A_k over the domain (σ_{yp}, n). It was found that the trends of the fitting parameters A_k were successfully fitted using the following interpolating function:

$$A_k = \sum_{i=1}^{6} \sum_{j=1}^{6} \alpha_{ijk} \left(\frac{\sigma_{yp}}{G_1}\right)^{f_i} (n + G_2)^{f_j} \qquad (6.9)$$

where α_{ijk} are proper fitting parameters, f_i and f_j fixed exponents and G_1 and G_2 are a couple of numerical parameters introduced for improve the stability of the numerical algorithm: the variable σ_{yp}, in fact, varies between 50 and 2000, whereas n between 0.01 and 0.5. For estimating the exponents f_i and f_j and the offsets G_1 and G_2, the statistical approach previously described was used. Eqns. (6.3) and (6.9) were used to reconstruct each numerical *L*-*h* curve of the database for each class of materials, thus determining the discrete distributions (Fig. 6.7) of the maximum relative errors for the load *L* and the penetration depth *h* variables.

The exponents f_i and f_j and the offsets G_1 and G_2 were fixed in order to reduce the mean values and standard deviations of such distributions. The NEM was used to evaluate the fitting parameters α_{ijk}.

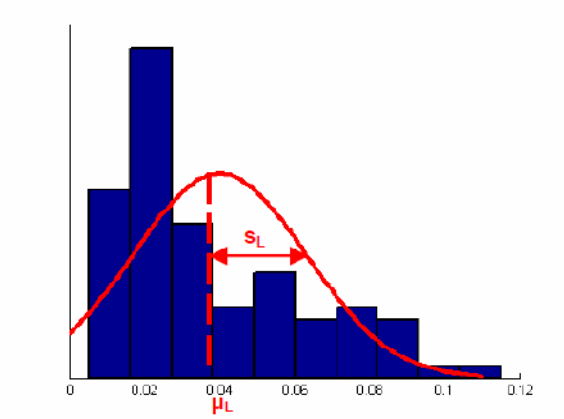

(a)

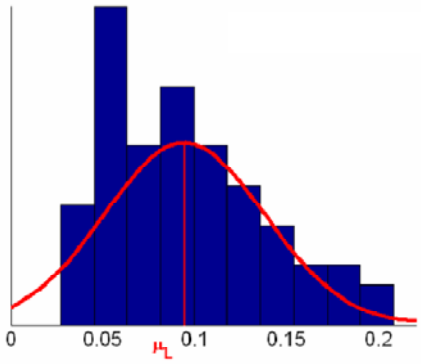

(b)

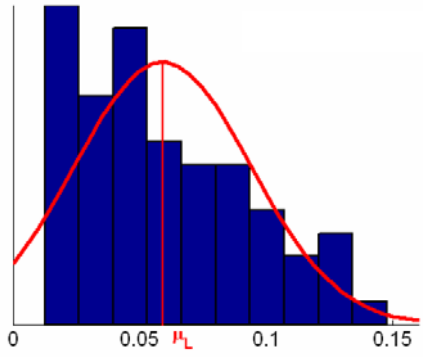

(c)

Figure 6.7. Frequencies histograms of the discrete distributions ΔL for (a) Al-alloys class, (b) steels class and (c) Cu-alloys class. Second level of interpolation.

It should be observed that the numerical *L*-*h* curves fitting is carried out after assuming as independent variable the indentation depth *h*. However, there are no prescriptions about the choice of the independent variable. To establish if the maximum relative error distributions in the first and second level of the interpolation can be affected by the choice of the independent variable, the direct analysis was also carried out by assuming the load *L* as independent variable. The numerical *h*-*L* curve was reconstructed using the following interpolating function,

$$h^{th} = ED^2 \sum_{k=1}^{4} \sum_{i=1}^{6} \sum_{j=1}^{6} \beta_{ijk} \left(\frac{\sigma_{yp}}{U_1}\right)^{t_i} (n + U_2)^{t_j} \left(\frac{L^{th}}{D}\right)^{r_k} \qquad (6.10)$$

Tab. 6.I collects the mean values and the corresponding standard deviations of the maximum relative errors distributions as a function of the independent variable for the considered material classes.

Table 6.I. Maximum relative errors distributions statistical parameters

	INDEPENDENT VARIABLE: INDENTATION DEPTH h					
	FIRST LEVEL OF INTERPOLATION			SECOND LEVEL OF INTERPOLATION		
	Steels	Al-Alloys	Cu-Alloys	Steels	Al-Alloys	Cu-Alloys
μ_h	8.7%	4.1%	5.9%	9.3%	4.0%	5.9%
s_h	3.7%	2.4%	3.3%	5.8%	2.3%	3.5%
μ_L	9.2%	4.3%	6.2%	8.7%	4.1%	4.9%
s_L	5.9%	1.8%	3.4%	4.3%	2.9%	3.8%
	INDEPENDENT VARIABLE: LOAD L					
	FIRST LEVEL OF INTERPOLATION			SECOND LEVEL OF INTERPOLATION		
	Steels	Al-Alloys	Cu-Alloys	Steels	Al-Alloys	Cu-Alloys
μ_h	4.7%	2.1%	3.2%	1.6%	0.8%	3.1%
s_h	4.9%	1.9%	2.2%	1.4%	0.6%	1.8%
μ_L	0.9%	0.5%	8.0%	0.6%	1.2%	0.7%
s_L	0.8%	0.5%	1.6%	0.5%	0.7%	0.7%

Both first and second level of interpolation are considered. The values summarized in Tab. 6.I proofs that a significant reduction in the interpolation error, both in the first and in the second level of the interpolation, can be obtained if the load *L* is treated as independent variable. Consequently, more accurate estimation of the constitutive properties must be expected, if the correlations between the proportionality limit σ_{yp} and strain-hardening coefficient n, from one side, and the numerical *L*-*h* curve, from the other side, are established using the representation given by Eqn. (6.10).

The accuracy of this approach allowed to establish the *L*-*h* curve for any given couple of (σ_{yp}, n). In this way the discrete domain represented by the database is no more covered by a discrete grid of *L*-*h* curves, but by a continuous function. This is of paramount importance for the reverse analysis.

6.2 Reverse Analysis

In order to carry out the reverse analysis, the function correlation the plastic properties to the *L*-*h* curves should be invertible. Unfortunately, this is impossible, thus preventing the direct deduction of the constitutive properties of any indented material from the *L*-*h* curve. Numerical methods based on optimization algorithms must be employed. The choice of the most proper algorithm must be related to the characteristics of the *L*-*h* curves. From this point of view, it should be remembered that the typical experimental output provided by an instrumented indentation test is represented by a sequence of

M couples of measured values $L_m^{exp} - h_m^{exp}$ with $m = 1, \dots, M$. As shown in the review (see Chapter 3), Beghini et al. [57] proposed the following comparison criterion,

$$\chi(E, \sigma_{yp}, n) = \sum_{m=1}^{M} \left[L^{th}(h_m^{exp}, E, \sigma_{yp}, n) - L_m^{exp} \right]^2 \qquad (6.11)$$

for inferring the constitutive parameters of the Hollomon power law from the experimental *L*-*h* curves. In other terms, after fixing the material class, the estimation of the constitutive parameters is carried out by implementing Eqn. (6.11) in an optimization procedure [87] which scans the domain (σ_{yp}, n) and selects the theoretical curve which minimizes the function $\chi(E, \sigma_{yp}, n)$.

Eqn. (6.11) represents a measurement of the global distance between the experimental points $L_m^{exp} - h_m^{exp}$ and the theoretical curve corresponding to the material properties (E, σ_{yp}, n). The evaluation of the $L^{th} - h^{th}$ curve is made possible by applying the direct analysis previously described. NEM can be used to evaluate such distance and small and constant absolute error is achieved adopting this approach [83]. However, if the relative error trend as a function of the indentation depths *h* is analyzed, significant errors were found at low penetration depths [83]. It should be remembered that the early stages of the indentation process are of paramount importance for deducing the proportionality limit of the indented material. Accordingly, non negligible errors in the estimation of the proportionality limit must be expected if the comparison criterion given by Eqn. (6.11) is used. From this point of view, improvements can be attained if the minimization is carried out onto the relative

error. Keeping in mind that the *h-L* curve provides better performances in terms of fitting accuracy, the following definition

$$\chi(E,\sigma_{yp},n)=\sum_{m=1}^{M}\left[\frac{h^{th}(L_m^{exp},E,\sigma_{yp},n)-h_m^{exp}}{h_m^{exp}}\right]^2 \qquad (6.12)$$

was then assumed for evaluating the relative distance between the experimental h^{exp}-L^{exp} and theoretical h^{th}-L^{th} curves. Of course, adopting this comparison criterion, larger errors in the estimation of the strain-hardening coefficient n must be expected with respect to that obtained by applying the criterion proposed by Beghini et al. [57]. Since the proportionality limit is undoubtedly the most important parameter from the engineering point of view, establishing the comparison on the base of the relative distance concept was judged more reasonable.

As regards to the effective estimation of the constitutive properties, the algorithm scans the domain (σ_{yp},n) by defining a coarse grid. At each node of the grid the $h^{th}-L^{th}$ is determined and compared with the experimental one. After determining the $h^{th}-L^{th}$ providing the best approximation of the experimental $h^{exp}-L^{exp}$ curve, a more refined sub-domain is defined around the point corners corresponding to the selected $h^{th}-L^{th}$. The procedure is repeated iteratively until the objective function satisfies a proper tolerance criterion. The procedure appeared to be barely affected by local minimum. A schematic representation of the iterative domain refinement is depicted in Fig. 6.8.

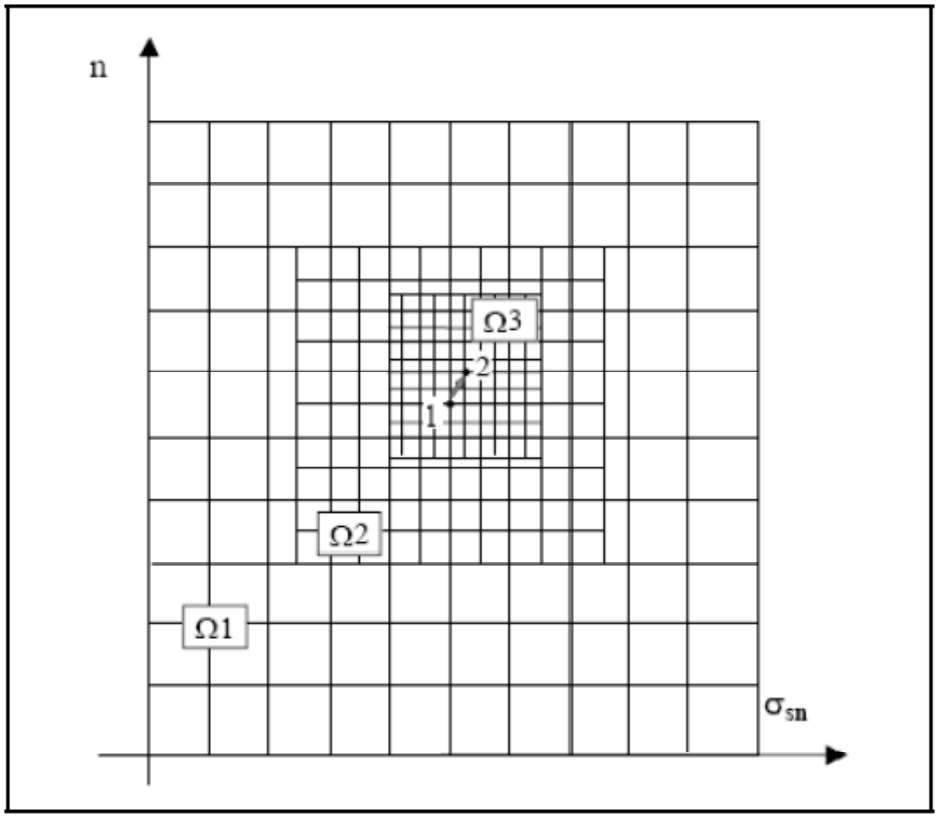

Figure 6.8. Sub-domain definition implemented in the optimization criterion.

6.3 Experimental validation of the reverse analysis

To assess the improvements brought to the methodology proposed by Beghini et al. [57], the experimental *L*-*h* curve of Al 6082-T6 alloy obtained by spherical indentation tests (see Chapter 4) was used as input in the reverse analysis.

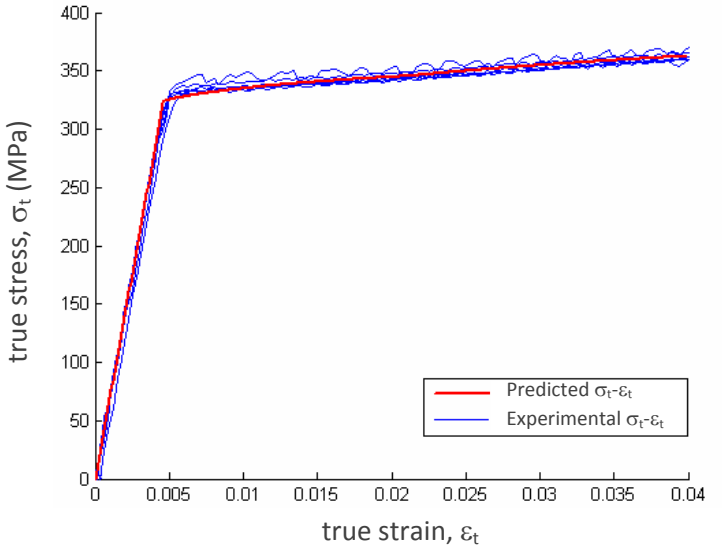

(a)

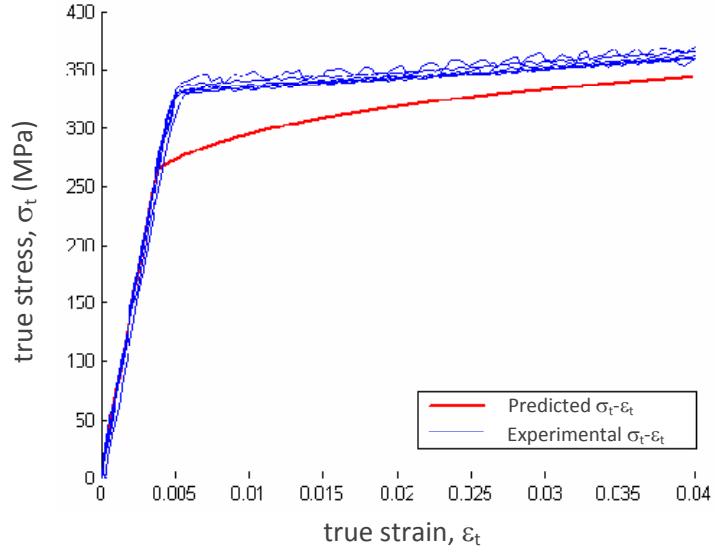

(b)

Figure 6.9. Comparison between the experimental tensile true stress-true strain curves sheaf of Al 6082-T6 alloy and the predicted true stress-true strain curve obtained via (a) the new evaluation procedure and (b) the procedure presented in [57].

Fig. 6.9a shows the comparison between the experimental stress-strain curves sheaf obtained by tensile testing from Al 6082-T6 alloy and the predicted curve adopting the new algorithm. The comparison between the calculated stress-strain curve according to the evaluation procedure developed by Beghini et al. [57] is conversely reported in Fig. 6.9b.

The improvements in the prediction in the near yield region with respect to the previous methodology are significant. A very good agreement can be observed in the near yield region being the relative errors within 3%.

The material strain-hardening capabilities in the first part of the stress-strain curve are also well predicted by the new algorithm. Conversely, an underestimation of the stress-strain curve is observed in the methodology proposed by Beghini et. al [57]. For Al 6082-T6 alloy the relative discrepancies on σ_{yp} are greater than 10%. In addition, if the trend of the experimental stress-strain curve above the proportionality limit is compared to that predicted by the reverse analysis, an overestimation of the strain-hardening coefficient appears evident when the previous algorithm is used. In other terms for this material, the algorithm proposed by Beghini et al. [] seems to underestimate the proportionality limit and overestimate the strain-hardening coefficient. This phenomenon does not occur in the new algorithm.

Although more than one material should be tested for assessing the improvements brought to previous algorithm, there are no doubts on the fact that an appropriate fitting of the *L-h* curves, for determining

the correlation between this characteristic curve and the constitutive properties, and the comparison criterion adopted by the reverse analysis play a key role in the prediction of the stress-strain curve of the indented material. In particular it was shown that the proportionality limit and the first part of the stress-strain curve can be correctly determinate if the error in predicting the first part of the *L*-*h* curve is minimized. The information coming from the first part of the *L*-*h* curve is of paramount importance for determining the σ_{yp} and the first hardening, whereas the entire curve is necessary to predict extensive plastic deformations. Keeping in mind this important results, further improvements of the reverse analysis could be obtained by performing a progressive analysis of the *L*-i curve. This represents an issue left open by this work. The implementation of the progressive analysis can be particularly useful for determining the stress-strain curves of materials that do not obey to the Hollomon power law, such as for example low carbon steels showing the upper and lower yield stress phenomenon followed by strain-hardening.

6.4 Summary

To accurately estimate the stress-strain curve of any material by instrumented spherical indentation testing, appropriate direct and reverse analyses of the indentation response are required. From this point of view, as the evaluation of the constitutive properties is carried out by guessing the material behaviour from the characteristic *L*-*h* curve of the indented material, two crucial features must be taken

into account. The interpolating functions used to correlate the *L*-*h* curve to the constitutive parameters and the criterion adopted for comparing the experimental *L*-*h* curve with a reference curve, for which the constitutive properties are known.

The present chapter showed that how the proper choice of the interpolating functions in the direct analysis of the *L*-*h* curves and the comparison criterion in the reverse analysis can significantly affect the accuracy of the predictions. To improve the accuracy of the prediction, a new methodology, involving the statistical analysis, was proposed at first for correlating the *L*-*h* curve to the proportionality limit and strain-hardening coefficient parameters. Guidelines for selecting the most appropriate comparison criterion were then provided.

The experimental validation carried out by analysing the experimental *L*-*h* curve of a real material confirmed that very good results in terms of stress-strain curve predictability can be attained adopting the evaluation algorithm proposed in the present chapter.

CHAPTER 7
Concluding remarks

The development of evaluation procedures for deducing the constitutive laws of metallic materials by instrumented indentation testing represented the final goal of the present doctoral dissertation. The first part summarized the state of the current researches on the most promising indentation theories of elastic-plastic solids and methodologies nowadays developed for deducing the constitutive parameters from the materials indentation response.

In particular Chapter 2 reviewed the major developments in indentation mechanics for studying the evolution of the plastic strains field in the sub-indenter region. The indentation regimes of linear elastic-strain hardening solids were investigated. The analysis showed that the developed approaches are able to describe only qualitatively the materials indentation response from the straining phenomena point of view and established the driving constitutive parameters. The analysis also highlighted the difficulties in inferring the correlations between the indentation response and the constitutive law except for materials obeying to ideal behaviours like Hollomon power law.

The methodologies developed for deducing the stress-strain curves from the indentation data were reviewed in Chapter 3. Several strategies for deducing the material behaviour arose: crater profile and local plastic strains field analyses as well as the load-indentation depth curve (*L*-*h* curve) can be used to this purpose. However, the review evidenced as the correlations between the indentation and the constitutive parameters can be estimated only for ideal material behaviours. In some cases, the assessment of such correlations appeared particularly difficult. From this point of view, the main limit was especially found in the crater profile measurement. These procedures did not properly take into account those experimental parameters that can potentially affect the indentation response. Accordingly, the application of such evaluation procedures may lead to inaccurate estimation of the constitutive parameters from the experimental data, when real materials are tested.

On the base of this frame, the second part of the present doctoral dissertation was addressed in order to develop a new evaluation procedure able to infer the constitutive laws of real metallic materials.

The Chapter 4 was devoted to present the new tool for exploring the deformation processes occurring in the indented material during the experimental test. A new testing machine and a computational model were setup and subsequently integrated by correlating the experimental response of two common engineering materials (Al 6082-T6 aluminum alloy, AISI H13 steel) to the numerical predictions. Very good agreements were obtained between the two approaches.

The new tool was then used to describe the indentation response of the previously characterized materials (Chapter 5) and the most reliable source of information from which deducing the constitutive parameters, was established. The deep analysis of the deformation mechanisms reported in Chapter 5 occurring in Al 6082-T6 alloy and AISI H13 steel revealed that friction plays a key role in the definition of the crater profile evolution and in the plastic strains development. Due to the impossibility to establish a priori the value of the friction coefficient in an experimental test, the estimations based on proper analysis of the impression promoted by the indenter and the resulting plastic strain field appeared particularly critical. Conversely, it was found that the friction barely affect the trend of the characteristic *L-h* curve. From the material properties evaluation point of view, L-h curve represents the most reliable source of information coming from the indented material. The new tool also allowed to establish the correlations between the indentation depth *h* and the amount of the plastic strain, from one side, and the material volume plastically strained, from the other side. In this way it is possible both to evaluate if the indentation response is effectively representative of the material behaviour and to distinguish the portion of the stress-strain curve for which the estimation can be carry out.

On the base of the aforementioned results, a new algorithm based on the interpretation of the *L-h* curve was built-up for inferring the constitutive properties of three classes of common engineering materials: steels, aluminium alloys and copper alloys (Chapter 6). The estimation of the constitutive properties via comparing the experimental *L-h* with a reference curve corresponding to known

properties was found to be very powerful in terms of accuracy, when the direct analysis between the constitutive parameters and the characteristic *L*-*h* curve and the reverse algorithm are properly are properly setup. To this purpose a specific database of *L*-*h* curves for the three considered classes of metals were generated and used to correlate the indentation response to the constitutive parameters via fitting procedures. To improve the accuracy of fitting procedures a statistical approach was adopted for reducing the errors in the interpolation of *L*-*h* curves. The error analysis approach was also used to select the comparison algorithm ensuring the minimum errors in near yield region of the stress-strain curve. A good agreement was found between the experimental stress-strain curve and numerical prediction for Al 6082-T6 alloy.

The proposed method can be easily extended to a wider range of metallic materials, thus resulting a powerful tool for material characterization. If the correlation between the indentation depth h and the plastic strain amount is known, the present method can be also applied to investigate a specific portion of the stress-strain curve of the indented materials.

In conclusion, the new methodology may be also applied to deduce the constitutive properties of materials having complex stress-strain curves. This is a topic left open by this doctoral dissertation that the author will investigate detail in the future.

References

[1] D. Tabor, *The Hardness of Metals*, Clarendon Press, Oxford, 1951.

[2] B.W. Mott, *Micro-Indentation Hardness Testing*, Butterworth & Co, London, 1956.

[3] H. O'Neil, *Hardness Measurement of Metals and Alloys*, Chapman and Hall, London, 1967.

[4] E.R. Petty, Hardness Testing, in Techniques of Metals Research: Measurement of Mechanical Properties, Vol. 5 (2), pp. 157-221 (1971).

[5] G.E. Dieter, Mechanical Metallurgy, Mc-Graw Hill, New York, 1976.

[6] H.E. Boyer, *Hardness Testing*, ASM, 1987.

[7] P.J. Blau, B.R. Lawn, Microindentation Techniques in Materials Science, ASTM STP 889, 1995.

[8] ASTM E10-93, Standard Test Method for Brinell Hardness of Metallic Materials, 1993.

[9] P.J. Blau, B.R. Lawn, Microindentation Techniques in Materials Science, ASTM STP 889, 1995.

[10] B.R. Lawn, *Fracture of Brittle Solids*, Cambridge University Press, 1993.

[11] I.J. McColm, *Ceramic Hardness*, Plenum Press, New York, 2000.

[12] A.C. Fisher-Cripps, Nanoindentation, Springer-Verlag, New York, 2002.

[13] J.H. Westbrook, H. Conrad, The Science of Hardness Testing and Its Research Applications, ASM, Metals Park, 1973.

[14] S.P. Baker, R.F. Cook, S.G. Corcoran N.R. Moody, Fundamentals of Nanoindentation and Nanotribology II, Materials Research Society Symposium Proceedings, Vol. 649 (2001).

[15] M.M. Chaudhri, Y.Y. Lim (Eds.), Second International Indentation Workshop, Cavendish Laboratory, University of Cambridge, Cambridge, UK, 15-20 July, Philosophical Magazine, Vol. 82 (2002).

[16] Y.T. Cheng, T. Page, G.M. Pharr, M. Swain, K.J. Wahl (Eds.), Fundamental and Applications of Instrumented Indentation in Multidisciplinary Research, Journal of Material Research, Vol. 19 (2004).

[17] M. Towler, A.J. Bushby, R.W. Billington, R.G. Hill, A preliminary comparison of the mechanical properties of chemically cured and ultrasonically cured glass ionomer cements, using nano-indentation techniques, Biomaterial, Vol. 22, pp. 1401-1406 (2001).

[18] S. Hengsberger, J. Enstroem, F. Peyrin, P. Zysset, How is the indentation modulus of bone tissue related to its macroscopic

elastic response? A validation study, Journal of Biomechanics, Vol. 36 (10), pp. 1503-1509 (2003).

[19] J.Y. Rho, T.Y. Tsui, G.M. Pharr, Elastic Properties of Human Cortical and Trabecular Lamellar Bone measured by Nanoindentation, Journal of Biomaterials, Vol. 18 (20), pp.1325-1330 (1997).

[20] J. Mencik, M.V. Swain, Micro Indentation with Pointed Indenters, Materials Forum, Vol. 18, pp. 277-288 (1994).

[21] G.M. Pharr, Measurement of Mechanical Properties by Ultra-low Load Indentation, Materials Science and Engineering A, Vol. 253, pp. 151-159 (1998).

[22] J.L. Hay, G.M. Pharr in: H. Kuhn, D. Medlin (Eds.), ASM Handbook: Mechanical Testing and Evaluation, ASM International Materials Park, Vol. 8 (2000).

[23] M.R. VanLandingham, Review of Instrumented Indentation, Journal of Research at the National Institute of Standards and Technology. Vol. 108, pp. 249-265 (2003).

[24] G.M. Pharr, W.C. Oliver, F.R. Brotzen, On the Generality of the Relationship among Contact Stiffness, Contact Area and Elastic Modulus during Indentation, Journal of Materials Research, Vol. 7, pp. 613-617 (1992).

[25] M.F. Doerner, W.D. Nix, A Method for Interpreting the Data depth-sensing Indentation Instruments, Journal of Material Research, Vol. 1 (4), pp. 601-609 (1986).

[26] W.C. Oliver, G. M. Pharr, A New Improved Technique for determining Hardness and Elastic Modulus using Load and Sensing Indentation Experiments, *Journal of Materials Research*, Vol. 7 (6), pp. 1564-1582 (1992).

[27] X. Chen, J.H. Hutchinson, A.G. Evans, The Mechanics of Indentation Induced Lateral Cracking, Journal of American Ceramic Society, Vol. 88, pp. 1233-1238 (2005).

[28] M. Zhao, N. Ogasawara, N. Chiba, X. Chen, A New Approach to Measure the Elastic-Plastic Properties of Bulk Materials using Spherical Indentation, Acta Materialia, Vol. 54, pp. 23-32 (2006).

[29] X. Chen, N. Ogasawara, M. Zhao, N. Chiba, On the Uniqueness of Measuring Elastoplastic Properties from Indentation: the Indistinguishable Mystical Materials, Journal of the Mechanics and Physics and Solids, Vol. 55, pp. 1618-1660 (2007).

[30] W.C. Oliver, G.M. Pharr, Measurement of Hardness and Elastic Modulus by Instrumented Indentation: Advances in Understanding and Refinements to Technology, Journal of Materials Research, Vol. 19 (1), pp. 3-20 (2004).

[31] A.E.H. Love, Boussinesq's problem for a rigid cone, Quarterly Journal of Mathematics, Vol. 10, pp. 161-175 (1939).

[32] I.N. Sneddon, The relation between load and penetration in the axisymmetric boussinesq problem for a punch of arbitrary profile, International Journal of Engineering Science, Vol 3 (1), pp. 47-57 (1965).

[33] D. Tabor, The hardness of solids, Review of physics in technology, Vol. 1, pp.145-179 (1970).

[34] E. Meyer, Untersuchungen über Harteprufung und Harte, Z. Ver. Deutche Ing., Vol. 52, pp. 645-654 (1908).

[35] Y.T. Cheng, C.M. Cheng, Scaling, Dimensional Analysis, and Indentation Measurements, Material Science and Engineering, 44 R, pp. 91-149 (2004).

[36] H. O'Neil, The Significance of Tensile and other Mechanical Test Properties of Metals, Proceeding of the Institute of Mechanical Engineers, Vol. 151, pp. 116-130 (1944).

[37] J.R. Matthews, Indentation Hardness and Hot Pressing, Acta Metalurgica, Vol. 28, pp. 311-318 (1980).

[38] B. Taljat, G.M. Pharr, Development of pile-up during spherical indentation of elastic-plastic solids, International Journal of Solids and Structures, Vol. 41, pp. 3891-3904 (2004).

[39] R. Hill, B. Storakers, A.B. Zdunek, A theoretical study of the Brinell hardness test, Proceeding of the Royal Society of London A, Vol. 473, pp. 301-330 (1989).

[40] A.L. Norbury, T. Samuel, The recovery and sinking-in or piling-up of material in the Brinell test, and the effect of these factors on the correlation of the Brinell with other hardness test, Journal of Iron and Steel Institute, Vol. 117, pp. 673-687 (1928).

[41] Y. Tirupataiah, G. Sundararajan, On the Constraint Factor Associated with the Indentation of Work-Hardening Materials

with a Spherical Ball, Metallurgical Transaction A, Vol. 22 A, pp. 2375-2384 (1991).

[42] H. Hertz, “Über die Berührung fester elastischer Körper”, J. reine und angewandte Mathematik, Vol. 92, pp. 156-171 (1882).

[43] H. Hertz, “Über die Berührung fester elastischer Körper and über die Harte”, Verhandlungen des Vereins zur Beförderung des Gewerbefleisses, Leipzig (1882).

[44] K.L. Johnson, *Contact Mechanics*, Cambridge University Press, Cambridge, 1985.

[45] S. Timoshenko, J.N. Goodier, *Theory of Elasticity*, McGraw-Hill, London, 1951.

[46] K.L. Johnson, The Correlations of Indentation Experiments, Journal of Mechanics and Physics of Solids, Vol. 18, pp. 115-126 (1970).

[47] L.E. Samuel, T.O. Mulhearn, The Deformed Zone Associated with Indentation Hardness Impressions, Journal of the Mechanics and Physics of Solids, Vol. 5, pp. 125- (1956).

[48] T.O. Mulhearn, Deformation of Metals by Vickers-type Pyramidal Indenters, Journal of the Mechanics and Physics of Solids, Vol. 7, pp. 85- (1959).

[49] R. Hill, *Theory of Plasticity*, University Press, Oxford, 1950.

[50] R. Hill, B. Storakers, A.B. Zdunek, A Theoretical Study of the Brinell Hardness Test, Proceedings of the Royal Society of London A, Vol. 423, pp. 301-330 (1989).

[51] A.F. Bower, N.A.. Fleck, A. Needleman, N. Ogbonna, Indentation of Power-law Creeping Solids, Proceedings of the Royal Society of London A, Vol. 471, pp. 97-124 (1993).

[52] S. Biwa, B. Storakers, An Analysis of fully plastic Brinell indentation, Journal of Mechanics and Physics of Solids, Vol. 13 (4), pp. 1049-1058 (1995).

[53] A.C. Fischer-Cripps, Elastic-plastic Behaviour in Materials Loaded with a Spherical Indenter, Journal of Material Science, Vol. 32, pp. 727-736 (1997).

[54] S.D.J. Mesarovic, N.A. Fleck, Spherical Indentation of Elastic-plastic solids, Proceedings of the Royal Society of London A, Vol. 455, pp. 2707-2728 (1999),

[55] H. Lee, J.H. Lee, G.M. Pharr, A Numerical Approach to Spherical Indentation Techniques for Material Property Evaluation, Journal of the Mechanics and Physics of Solids, Vol. 53, pp. 2037-2069 (2005).

[56] M. Beghini, L. Bertini, V. Fontanari, Evaluation of the Flow Curve of Metallic Materials by means of Spherical Indentation, Proceeding of the 5th International Conference on Computational Methods in Contact Mechanics, in Contact mechanics 2001, Vol. 1, pp 241-252 (2001), Seville (Spain).

[57] M. Beghini, L. Bertini, V. Fontanari, Evaluation of the Stress-Strain Curve of Metallic Materials by Spherical Indentation, International Journal of Solids and Structures, Vol. 43, pp. 2442-2459 (2006).

[58] Y.P. Cao, J. Lu, A New Method to extract the Plastic Properties of Metal Materials from an Instrumented Spherical Indentation Loading Curve, Acta Materialia, Vol. 52, pp. 4023-4032 (2004).

[59] Y.P. Cao, X. Qian, N. Huber, Spherical Indentation into Elasticplastic Materials. Indentation-response based definitions of the Representative Strains, Materials Science and Engineering A, Vol. 454-455, pp. 1-13 (2007).

[60] M. Beghini, L. Bertini, V. Fontanari, B.D. Monelli, Numerical Analysis of Plastic Deformation Evolution into Metallic Materials during Spherical Indentation Process, Journal of Materials Research, Vol. 24, pp. 1270-1278 (2009).

[61] H. Stute, Investigation about the Influence of Grease on the Brinell Hardness of Steel, VDI-Berichte, Vol. 308, pp. 55-80 (1978).

[62] H. Habbab, B.G. Mellor, S. Syngellakis, Post-yield Characterization of Metals with Significant Pile-up through Spherical Indentation, Acta Materialia, Vol. 54, pp. 1965-1973 (2006).

[63] J.S. Field, M.V. Swain, A Simple Predictive Model for Spherical Indentation, Journal of Materials Research, Vol. 8 (2), pp. 297-306.

[64] P. Au, G.E. Lucas, J.W. Sheckerd, G.R. Odette, Flow Property Measurements from Instrumented Hardness Tests in Non-Destructive Evaluation in the Nuclear Industry, in Non-

Destructive Evaluation in the Nuclear Industry, ASM, Vol. 10, pp. 597-610 (1980).

[65] B. Taljat, T. Zacharia, F. Kosel, New Analytical Procedure to determine Stress-Strain Curve from Spherical Indentation Data, International Journal of Solids and Structures, Vol. 35 (33), pp.4411-4426 (1998).

[66] F.M. Haggag, R.K. Nanstad, J.T. Hutton, D.L. Thomas, R.L. Swain, Use of Automated Ball Indentation Testing to Measure Flow Properties and Estimate Fracture Toughness in Metallic Materials, Applications of Automation Technology to Fatigue and Fracture Testing, ASTM STP 1092, pp. 188-208 (1990).

[67] F.M. Haggag, J.A. Wang, M.A. Sokolov, K.L. Murty, Use of Portable/in situ Stress-Strain Microprobe System to Measure Stress-Strain Behaviour and Damage in Metallic Materials and Structures, Nontraditional Methods of Sensign Stress, Strain , and Damage in Materials and Structures, ASTM STP 1318, pp. 85-98 (1997).

[68] G.B. Sinclair, P.S. Follansbee, K.L. Johnson, Quasi-static normal indentation of an elasto-plastic half-space by a Rigid Sphere – II Results, International Journal of Solids and Structures, Vol. 21 (8), pp. 865-888 (1985).

[69] W.C. Oliver, G.M. Pharr, Measurement of Hardness and Elastic Modulus by Instrumented Indentation. Advanced in Understanding and Refinements to Methodology, Journal of Materials Research, Vol. 19, pp. 3-20 (2004).

[70] Y.T. Cheng, C.M. Cheng, Analysis of indentation loading curves obtained using conical indenters, Philosophical Magazine Letters, Vol. 77 (1), pp. 39-47 (1998).

[71] Y.T. Cheng, C.M. Cheng, Scaling approach to conical indentation in elastic-plastic solids with work hardening, Journal of Applied Physis, Vol. 84 (3), pp. 1284-1291 (1998).

[72] Y.T. Cheng, C.M. Cheng, Scaling relationships in conical indentation of elastic-perfectly plastic solids, International Journal of Solids and Structures, Vol. 36, pp. 1231-1243 (1999).

[73] M. Dao, N. Chollacoop, K.J. Van Vliet, T.A. Venkatesh, S. Suresh, Computationa Modelling of the Forward and Reverse Problems in Instrumented Sharp Indentation, Acta Materialia, Vol. 49, pp 3899-3918 (2001).

[74] G.I. Barenblatt, *Scaling, Self-similarity, and Intermediate Asymptotics*, Cambridge University Press, Cambridge, 1996.

[75] N. Ogasawara, N. Chiba, X. Chen, Representative Strain of Indentation Analysis, Journal of Materials Research, Vol. 20 (8), pp. 2225-2234 (2005).

[76] A. Nayebi, O. Bartier, G. Mauvoisin, R. El Abdi, New Method to determine the Mechanical Properties of Heat Treated Steels, International Journal of Mechanical Sciences, Vol. 43, pp. 2679-2697 (2001)

[77] A. Nayebi, R. El Abdi, O. Bartier, G. Mauvoisin, New Procedure to determine Steel Mechanical Parameters from the Spherical Indentation Technique, Mechanics of Materials, Vol. 34, pp. 243-254 (2002).

[78] M. Beghini, L. Bertini, F. Carsughi, W. Rosellini, Mechanical Characterization of Metallic Materials by Shear Punch Tests, Proceedings of the XXX Convegno Nazionale dell'Associazione Italiana per l'Analisi delle Sollecitazioni, Alghero, Italy, 12-15 September 2001, pp. 657-666 (in Italian).

[79] A. Di Gioia, Progetto Costruttivo di un Indentatore Sferico Strumentato", Bachelor's Degree Dissertation, University of Pisa, Faculty of Engineering, , A.Y. 2005/2006.

[80] M. Beghini, L. Bertini, V. Fontanari, On the possibility to obtain the Stress-Strain Curve for a Strain-Hardening Material by Spherical Indentation, International Journal of Computer Application in Technology, Vol. 15 (4/5), pp. 168-175 (2002).

[81] M. Beghini, L. Bertini, V. Fontanari, Dispositivo per la rilevazione di caratteristiche meccaniche di materiali, in particolare materiali metallici, National Patent n° TO/2004/A/000535 (2004).

[82] M.F. Ashby, *Materials Selection in Mechanical Design*, Pergamon Press, Oxford, 3rd Ed. 2005.

[83] D. Villano, Tecniche per l'acquisizione ed l'elaborazione di misure di indentazione sferica, Bachelor's Degree Dissertation, University of Pisa, Faculty of Engineering, , A.Y. 2006/2007.

[84] ANSYS, Version 11.0, Ansys INC (2009).

[85] K.J. Bathe, Finite Element Procedures, Prentice Hall, Upper Saddle River, 1996.

[86] ASTM E8-04, Standard Test Method for Tension Testing of Metallic Materials, 2004.

[87] M. Beghini, L. Bertini, L. Bosio, V. Fontanari, R. Valleggi, Progetto e Realizzazione del Diaptometro, strumento per la Caratterizzazione Meccanica di Materiali Metallici mediante Indentazione Sferica Strumentata, Proceedings of the XXXV Convegno Nazionale dell'Associazione Italiana per l'Analisi delle Sollecitazioni, Ancona, Italy, 13-16 September 2006 (in Italian).